Thermoelectric Properties of Bismuth Antimony Telluride Alloys

Thesis by

Hyun-Sik Kim

In Partial Fulfillment of the Requirements for

the degree of

Doctor of Philosophy

CALIFORNIA INSTITUTE OF TECHNOLOGY

Pasadena, California

2016

(Defended May 23, 2016)

ACKNOWLEDGEMENTS

This dissertation would not have been possible without the guidance, help, and the patience of several individuals who in one way or another contributed and extended their valuable assistance in the preparation and completion of this study.

First and foremost, my utmost gratitude to my advisor, Prof. Jeff Snyder, whose insight, understanding, and patience I will never forget. Prof. Snyder has been my lighthouse (bigger and brighter than the one in Evanston, IL) when I often drifted around in the deep, dark sea of data that I could not comprehend.

This thesis was enriched significantly through helpful discussions with my Thermoelectrics Group members Nick Heinz (who taught me how to grow textured crystals using the zone-melting furnace now at Northwestern University), Prof. Teruyuki Ikeda (who built the zone-melting furnace) Zach Gibbs (who taught me how to calculate multi-band transport behaviors via Python), Kasper Borup (who built Hall measurement instrument), Yinglu Tang, Stephen Kang, Heng Wang, Prof. Yanzhong Pei, Tristan day, Dr. Fivos Drymiotis, Saneyuki Ohno, Dr. Umut Aydemir, and many others.

My sincere thanks also goes to Prof. Sang Il Kim, Prof. Kyu Hyoung Lee, and Prof. Sung Wng Kim, who provided me a wonderful opportunity to collaborate with them on liquid compacted Bi-Sb-Te materials with a substantially low lattice thermal conductivity. Without their help and collaboration, it would not have been possible to finish this thesis.

I would also like to thank all of my former team members in Samsung Advanced Institute of Technology. I am particularly indebted to Prof. Kyu Hyoung Lee, Prof. Jong-Soo Rhyee, Prof. Sang Il Kim, and Prof. Kyung-Han Ahn, who taught me about thermoelectric materials. Most importantly, I would have not been able to study in the US at all without the generous financial support from Samsung Advanced Institute of Technology.

Last but not the least, I would like to thank my better half, Ok-Young Choi, and my 17 months old son, Rieu, who endured and persevered with me throughout my entire study. I will never forget the support from my families in Korea in every aspect I could ever imagine for me to finish the program in time.

ABSTRACT

Commonly used ozone-depleting refrigerants in refrigerators will be completely phased out in less than 15 years according to the Montreal Protocol. This imminent challenge can be tackled effectively by replacing the current vapor-compression cooling with environmentally sustainable thermoelectric cooling. *P*-type $(Bi_{0.25}Sb_{0.75})_2Te_3$ alloys have been intensively studied over the past 50 years for cooling applications because of their high thermoelectric performance near room temperature. However, the electronic origin of the high thermoelectric efficiency of $(Bi_{0.25}Sb_{0.75})_2Te_3$ alloys is often understated or ignored completely. In this thesis, the underlying physics of high electronic performance observed in the particular alloy composition, $(Bi_2Te_3)_{0.25}$–$(Sb_2Te_3)_{0.75}$, is investigated. It was demonstrated with two-band transport calculation that the convergence of bands occurred at $(Bi_2Te_3)_{0.25}$–$(Sb_2Te_3)_{0.75}$. A zT improvement of 17 % was also achieved in zone-levelled $(Bi_{0.25}Sb_{0.75})_2Te_3$ crystals by controlling their carrier concentration while using the two-band model as a guide. With the optimum electronic efficiency theoretically calculated and achieved experimentally, the thesis moves on to minimize lattice thermal conductivity of $(Bi_{0.25}Sb_{0.75})_2Te_3$ for the maximum zT. A new liquid compaction method was devised to produce dense arrays of dislocations in grain boundaries of nanostructured $(Bi_{0.25}Sb_{0.75})_2Te_3$. The grain boundary dislocations were found to be highly effective in scattering phonons and a substantial improvement in zT was possible (zT = 1.86 at 320 K). The understanding of phonon scattering by dislocations was in turn applied to phonon scattering at grain boundaries of polycrystalline materials. By demonstrating that the frequency-dependent dislocation scattering can replace the commonly used frequency-independent boundary scattering by Casimir, this thesis suggests that the grain boundary dislocation scattering may be responsible for the mechanism of phonon scattering at grain boundaries.

PUBLISHED CONTENT AND CONTRIBUTIONS

1. †Gibbs, Z. M., †Kim, H.-S., Wang, H. & Snyder, G. S. Band gap estimation from temperature dependent Seebeck measurement – Deviations from the $2e|S|_{max}T_{max}$ relation. *Appl. Phys. Lett.* **106**, 022112 (2015). DOI: 10.1063/1.4905922 (†Z. M. Gibbs and H.-S. Kim contributed equally to this work).

   H.-S. K. participated in theoretically comparing different band gap calculations with different assumptions, producing an engineers' chart for facile and accurate determination of band gap, and participated in the writing of the manuscript.

2. Kim, H.-S., Gibbs, Z. M., Tang, Y., W. Heng & Snyder, G. S. Characterization of Lorenz number with Seebeck coefficient measurement *APL Mater.* **3**, 041506 (2015). DOI: 10.1063/1.4908244.

   H.-S. K. participated in devising a simple equation as a function of Seebeck coefficient which can calculate Lorenz number without having to solve Boltzmann transport numerically, and participated in the writing of the manuscript.

3. †Kim, S. I., †Lee, K. H., †Mun, H. A., Kim, H.-S., Hwang, S. W., Roh, J. W., Yang, D. J., Shin, W. H., Li, X. S., Lee, Y. H., Snyder, G. J. & Kim, S. W. Dense dislocation arrays embedded in grain boundaries for high-performance bulk thermoelectrics. *Science* **348**, 109-114 (2015). DOI: 10.1126/science.aaa4166 (†S. I. Kim, K. H. Lee and H. A. Mun contributed equally to this work).

   H.-S. K. participated in analysis of data by achieving experimentally obtained low lattice thermal conductivity with lattice thermal conductivity modelling. H.-S. K. also estimated bipolar contribution to the total thermal conductivity by employing two-band transport calculation. H.-S. K. theoretically calculated the maximum coefficient of performance of modules and compared with experimental data. H.-S. K. participated in the writing of the manuscript.

4. Tang, Y., Gibbs, Z. M., Agapito, L. A., Li, G., Kim, H.-S., Nardelli, M. B., Curtarolo, S. & Snyder, G. J. Convergence of multi-valley bands as the electronic origin of high thermoelectric performance in $CoSb_3$ skutterudites. *Nat. Mater.* **14**, 1223-1228 (2015). DOI: 10.1038/NMAT4430.

   H.-S. K. participated in multi-band transport model calculation.

5. Kim, H.-S., Kang, S. D., Tang, Y., Hanus, R. & Snyder, G. J. Dislocation strain as the mechanism of phonon scattering at grain boundaries. *Mater. Horiz.* (2016). DOI: 10.1039/c5mh00299k.

   H.-S. K. participated in lattice thermal conductivity calculation and writing of the manuscript.

6. Kim, H.-S., Kim, S. I., Lee, K. H., Kim, S. W. & Snyder, G. J. Phonon scattering by dislocations at grain boundaries in polycrystalline $Bi_{0.5}Sb_{1.5}Te_3$. *Submitted.*

   H.-S. K. participated in lattice thermal conductivity calculation and writing of the manuscript.

7. Lavrentev, M. G., Osvenskii, V. B., Parkhomenko, Yu. N., Pivovarov, G. I., Sorokin, A. I., Bulat, L. P., Kim, H.-S., Snyder, G. J., Bublik V. T. & Tabachkova, N. Yu. Improved mechanical properties of thermoelectric $(Bi, Sb)_2Te_3$ by nanostructuring. *Accepted in APL Mater*. (2016).

   H.-S. K. participated in analysis of temperature-dependent strength data and writing of the manuscript.

8. Kim, H.-S., Heinz, N. A., Gibbs, Z. M., Tang, Y., Kang, S. D. & Snyder, G. J. High thermoelectric performance in $(Bi_{0.25}Sb_{0.75})_2Te_3$ system due to band convergence and independent carrier concentration control. *Submitted.*

   H.-S. K. participated in sample synthesis, compositional characterization, thermoelectric transport property measurements, two-band transport modelling, and participated in the writing of the manuscript.

TABLE OF CONTENTS

LIST OF FIGURES

LIST OF TABLES

Chapter 1

Introduction

1.1 History of refrigeration

Early history of refrigeration is closely related to our efforts to preserve food by keeping it cool. Centuries ago, when natural ice was the only available refrigerant people harvested ice in winter and stored it underground year-round to keep their food cold[2]. With the advent of an icebox (Fig. 1.1) in early 19th century, harvested ice could be stored domestically. When a block of ice was placed in a compartment at the top of the icebox, chilled air around the ice would travel down the box keeping food in lower compartments fresh. Insulating materials such as cork and sawdust were inserted in wooden walls of the icebox to prevent the ice from melting. When the ice eventually melted, it was drained through a spigot[3]. However, with increasing pollution in rivers (source of natural ice) ice harvesting and the use of iceboxes faded away by early 1910[4,5].

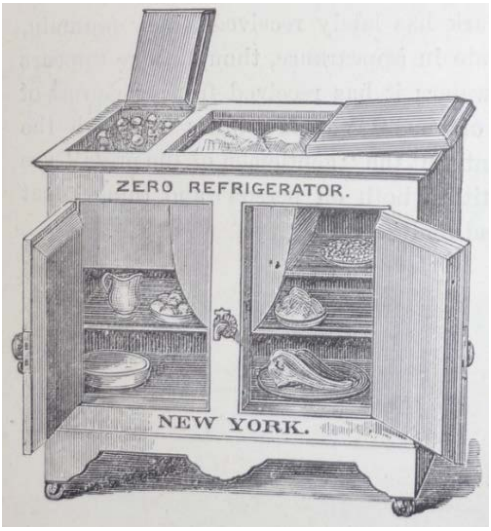

Fig. 1.1. Schematic diagram of an icebox from an advertisement in 1874. Image from Google

In 1930, electricity-powered refrigerators using synthetic refrigerant based on chlorofluorocarbon (CFC) were commercially available (the very first refrigerator powered by electricity was developed in 1927, but it utilized flammable and toxic methyl formate as its refrigerant)[6]. Unlike icebox where harvested ice was used as a refrigerant, mechanically circulating refrigerant (CFC) which changed its state between liquid and gas was used in the refrigerator (vapor-compression cooling).

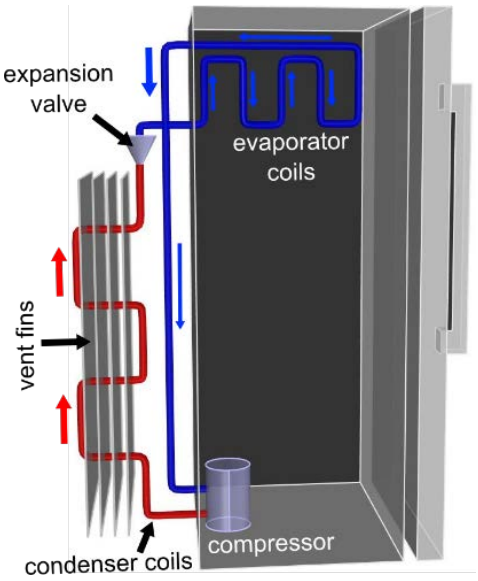

Fig. 1.2. Schematic diagram of a mechanical refrigerator. Image redrawn from a website run by The Institute of Refrigeration in the UK (www.fantasticfridge.com).

The refrigerant in gas (low pressure and low temperature, blue line entering the compressor in Fig. 1.2) is compressed to high pressured gas at high temperature. This work is done by a compressor powered by electricity. As the gas (high pressure and high temperature) enters the condenser and passes through vent fins (red line coming out of the compressor), it condenses to a liquid at a reduced temperature. Some of the liquid then quickly expands to a vapor at an expansion valve. This change of state suddenly drops the temperature of the liquid. The cold liquid lowers the temperature of the air inside the refrigerator and changes back to gas (low pressure, low temperature) in an evaporator in the refrigerator.

Despite the fact that it was less harmful to use CFC (or other newly developed hydrochlorofluorocarbon (HCFC) based refrigerant) than methyl formate (used in the first electric refrigerator in 1927) as refrigerants, both CFC and HCFC were identified as ozone-depleting gases. Currently, the CFCs are prohibited in the Montreal Protocol and even the HCFCs are scheduled for a complete phase-out by 2030[7]. Many efforts have been focused on developing a better refrigerant which is not ozone-depleting, but in order to tackle this ambitious task a completely different approach to refrigeration is necessary.

1.2 Thermoelectric solid-state cooling

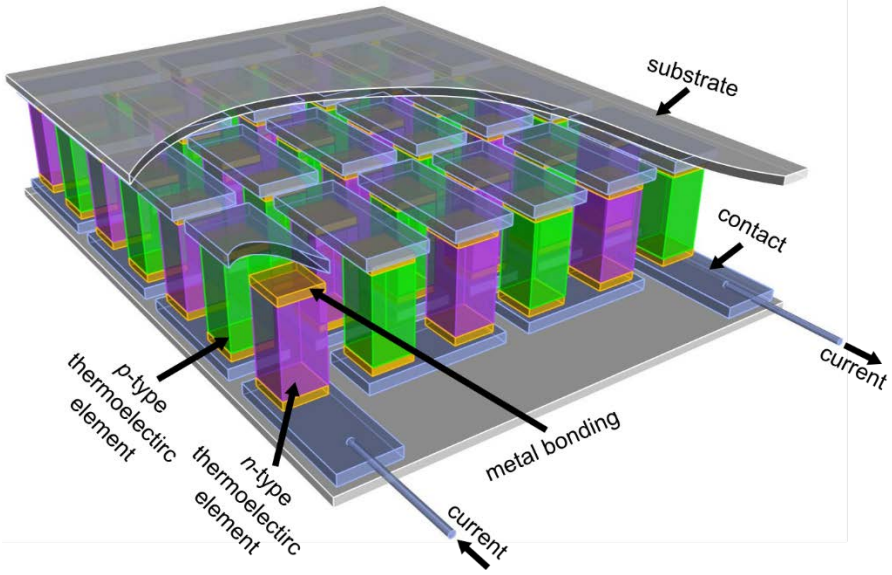

Fig. 1.3. Schematic diagram of a thermoelectric module

Thermoelectric solid-state cooling does not require any refrigerants for it to operate. All it needs are thermoelectric modules in Fig. 1.3 and an external electric current source. When an external electric potential is applied to the module, as the current runs through thermoelectric elements (*p*-type in green and *n*-type in purple) in series, heat is absorbed from one side of the module and released to the other (with the current flowing as in Fig. 1.3, the top surface of the module cools).

The thermoelectric module can absorb heat from one side (and dissipate the heat at another side) due to a thermoelectric phenomenon called Peltier effect. When current flows through *n*-type and *p*-type thermoelectric elements connected in series (Fig. 1.4), charge carriers from each thermoelectric element are forced to move. Both electrons (from *n*-type element) and holes (from *p*-type element) travel downwards (white dotted arrows in Fig. 1.4) while carrying heat along with them. This movement of charge carriers induced by electric potential makes one side of the thermoelectric module cold and the other side hot. A thermoelectric material's ability to convert the applied electric potential to a temperature difference is expressed in Seebeck coefficient, $S = V/\Delta T$ (V and ΔT are the applied voltage and induced temperature difference, respectively). Even though a material with a high Seebeck coefficient is not necessarily a good thermoelectric material, the good thermoelectric material has a high Seebeck coefficient (reason to be discussed in Chapter 1.3)

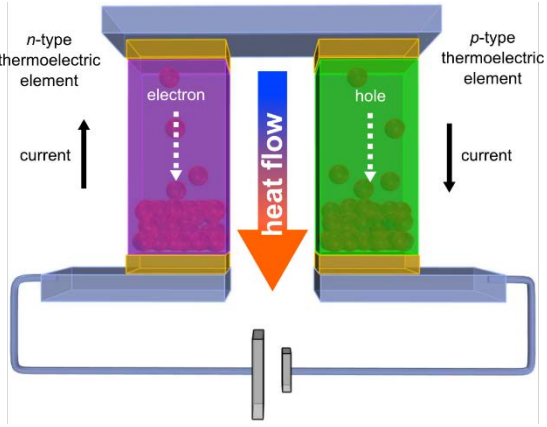

Fig. 1.4. Schematic diagram of a Peltier effect

Thermoelectric cooling is superior to its mechanical counterpart in many aspects. For instance, it is environmentally sustainable (refrigerant-free), free of vibration/noise (no compressor required), and even capable of zonal cooling. Commercially available thermoelectric wine refrigerator is a good example, which demonstrates thermoelectric cooling's advantages. A wine refrigerator cannot be made with a vapor-compression cooling, as the vibration it accompanies will agitate sediments in wines and eventually cause

the wines to age prematurely. Only vibration-free thermoelectric refrigerator can serve its purpose as a suitable wine cellar. Unfortunately, efficiency of the thermoelectric module is lower than that of the vapor-compression cooling which hinders thermoelectric refrigerator from replacing household mechanical refrigerator. For thermoelectric refrigerator to be more competitive than current vapor-compression refrigerator, development of highly efficient thermoelectric materials is needed.

1.3 Thermoelectric materials for cooling application

Efficiency of a thermoelectric material is characterized by a dimensionless figure-of-merit, $zT = S^2\sigma T/\kappa$ where S, σ, T, and κ are the Seebeck coefficient, electrical conductivity, temperature (absolute temperature), and thermal conductivity. Both charge carriers transporting heat (κ_e) and phonons propagating through lattice of a material (κ_l) contribute to the thermal conductivity ($\kappa = \kappa_e + \kappa_l$). In theory, an efficient thermoelectric material can be achieved by increasing both S and σ while keeping κ minimum. Nonetheless, optimizing zT is nontrivial because the variables in zT, which are expressed separately, are in fact coupled to each other. For example, the S is known to be inversely proportional to carrier concentration and directly proportional to entropy[8]. Qualitatively, it can be reasoned that a material with a high carrier concentration has a low entropy as there is not much more room to accommodate additional carriers. In contrast, another material with low carrier concentration will have a high entropy for the exactly opposite reason. Thus, by decreasing carrier concentration of a material, its S will increase but its σ will decrease along with κ_e. A more detailed interrelationship among thermoelectric parameters is depicted in Fig. 1.5. Approximately, an optimized thermoelectric material (with high zT) has a carrier concentration in a range between $10^{18} \sim 10^{20}$ (cm^{-3}), where a typical heavily-doped semiconductor lies.

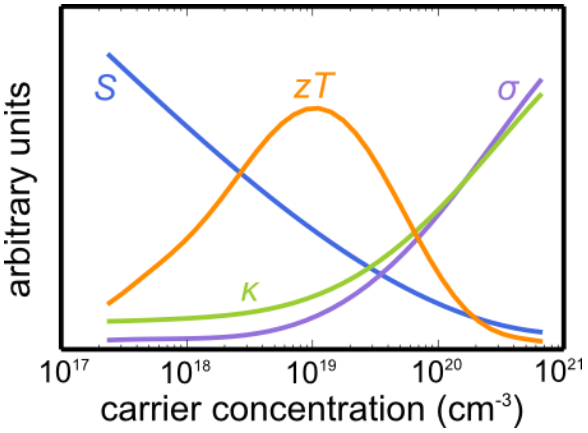

Fig. 1.5. Schematic dependence of thermoelectric parameters with respect to charge carrier concentration. Curves are redrawn from Heng Wang[9].

Among other thermoelectric materials, Bi_2Te_3-based alloys have been found to have the highest zT near room temperature (~300 K) as shown in Fig. 1.6. Because of their high *zT* near 300 K, they have been studied extensively for their application in cooling devices.

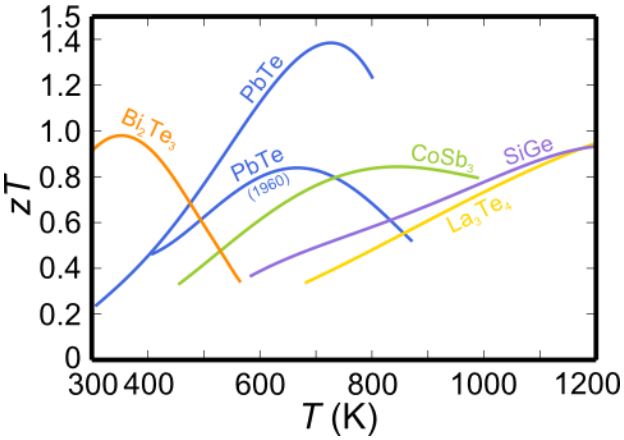

Fig. 1.6. *zT* for different *n*-type thermoelectric materials with respect to temperature. Data are from Snyder and Toberer[10].

Bi_2Te_3 crystal has a layered hexagonal crystal system (also a rhombohedral structure) as drawn in Fig. 1.7. Tellurium (Te) in Bi_2Te_3 can be situated in two different positions (distinguished by Te (1) and Te (2)). While layers of bismuth (Bi) and Te are strongly held together by covalent-ionic bonds, the connection

between Te (1) layers (between orange layers in Fig. 1.7) is much weaker (van der Waals bonding)[11]. Therefore, Bi_2Te_3 single crystal easily cleaves along *a*-*b* basal plane.

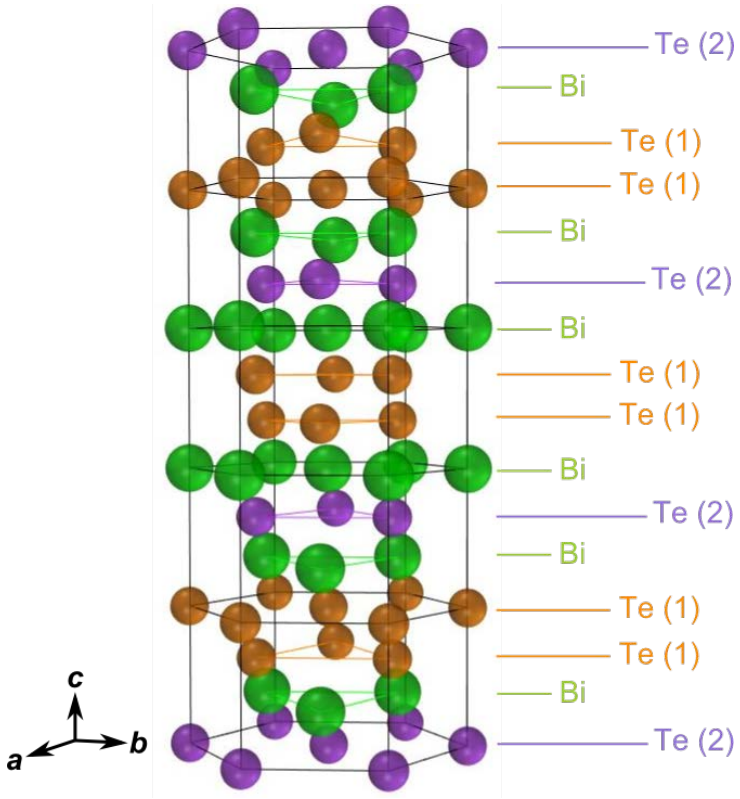

Fig. 1.7. Crystal structure of Bi_2Te_3. Te atoms in two different positions are distinguished by Te (1) and Te (2).

In addition to the anisotropy in mechanical property, some thermoelectric properties of Bi_2Te_3 single crystal are observed to be anisotropic as well (i.e. electrical conductivity and Hall coefficient, which is related to carrier concentration)[11,12]. Drabble[13] explained the observed anisotropy in transport with a multiple Fermi surfaces in its band structure. For *p*-type Bi_2Te_3, it was found that the highest valence band had a valley degeneracy (N_v) of 6[(13)]. The complex band structure with anisotropic Fermi pockets (Fig. 1.8) in *p*-type Bi_2Te_3 makes its high thermoelectric performance possible[14].

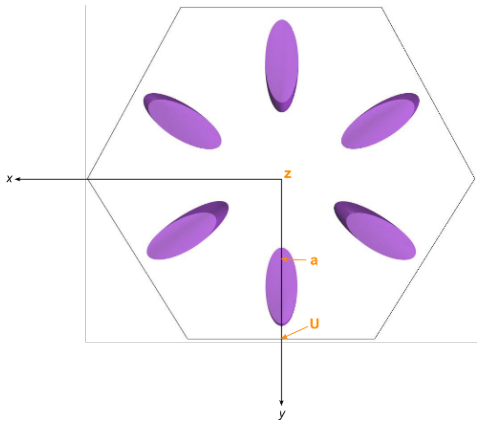

Fig. 1.8. Valence band structure of *p*-type Bi_2Te_3. Only the Fermi surfaces which correspond to the highest valence band are present (in purple). High symmetry points are noted as z, a, and U in orange.

1.4 Summary of research

This thesis focuses on improving current best thermoelectric material for cooling (Bi_2Te_3-based alloys) in order to help advance a new era of solid-state cooling refrigerators. Because the substitution of isoelectronic Sb^{3+} for Bi^{3+} in Bi_2Te_3 has the potential to improve zT by reducing the thermal conductivity, $(Bi_{1-x}Sb_x)_2Te_3$, especially $(Bi_{0.25}Sb_{0.75})_2Te_3$ (x = 0.75) alloys have been studied extensively in literature (composition x = 0.75 has the best zT among $0 \leq x \leq 1$).

The first part of the thesis explores possibilities to further enhance thermoelectric performance of $(Bi_{0.25}Sb_{0.75})_2Te_3$ alloys. To begin with, the reason that the $(Bi_{1-x}Sb_x)_2Te_3$ alloys have the highest zT at x = 0.75 is examined. Historically, it has been assumed that only the highest valence bands in Bi_2Te_3 and Sb_2Te_3 contribute in transport. Consequently, the transport properties of $(Bi_{1-x}Sb_x)_2Te_3$ alloys interpreted with a single valence band model results in a conclusion that the density-of-states effective mass of the band suddenly peaks at x = 0.75 (hence the highest Seebeck coefficient and zT). However, it is proposed that the maximum Seebeck coefficient is not because of the abrupt increase in the effective mass but because of the convergence of bands (between the first valence band and the second valence band). Based on this two band model, an improved zT is achieved from careful carrier concentration tuning by changing the amount of excess Te in oriented $(Bi_{0.25}Sb_{0.75})_2Te_{3+\delta}$ crystals.

Strategies to reduce thermal conductivity of $(Bi_{0.25}Sb_{0.75})_2Te_3$ polycrystalline material are also investigated. A liquid-phase compaction method, which involves Spark Plasma Sintering (SPS) of $(Bi_{0.25}Sb_{0.75})_2Te_3$ powders with excess Te is found to produce dense arrays of dislocations in grain boundaries of polycrystalline $(Bi_{0.25}Sb_{0.75})_2Te_3$ when melted excess Te is expelled during the SPS process. Phonon scattering by the dislocations reduces thermal conductivity significantly with a very high zT of 1.86 at 320 K. Further phonon scattering due to modulation of solute concentration near dislocation strain fields is also presented.

Secondly, important physics behind thermoelectric parameters are analyzed. Developing a theoretical tool that accurately describes properties of a material is important as it broadens our understanding of the physics behind. Furthermore, it will guide us to new strategies for improving performance of the material as well. First of all, an alternative approach to boundary scattering is proposed. A frequency-independent phonon mean free path has been commonly used to describe phonon boundary scattering in polycrystalline materials. However, recently it was discovered that at low temperature, the frequency-independent boundary scattering could no longer describe thermal conductivity of nanostructured materials. Therefore a better analytical model which works in all temperature range is suggested. Tools for an accurate determination of energy band gap and Lorenz number (both important in calculating zT accurately) as a function of measured thermopower (absolute value of S) are discussed as well.

Lastly, mechanical strength of Bi_2Te_3-Sb_2Te_3 alloys fabricated by hot extrusion, vertical zone melting, and SPS are compared. This study is relevant to the practical application of the material in a thermoelectric module as thermoelectric elements in the module are subjected to stress when they are assembled in the module and when the module is in use.

Chapter 2

Experimental methods

2.1 Summary of experimental methods

Experimentally, this thesis studies $(Bi_{0.25}Sb_{0.75})_2Te_3$ synthesized by two very different methods: zone-melting and Spark Plasma Sintering (SPS). Because the samples synthesized by SPS were made by our collaborators in Samsung Advanced Institute of Technology (SAIT) and Sungkyunkwan University in the Republic of Korea, tools used to characterize the samples are also different from those used to analyze samples fabricated by zone-melting at Caltech. Therefore, this chapter is first divided by material synthesis technique. Under each different synthesis method, synthesis procedure and sample characterization are detailed.

2.2 Starting charge zone-melting for $(Bi_{0.25}Sb_{0.75})_2Te_{3+\delta}$

This section contains contents that have been submitted to a journal. Once it is accepted, permission will be asked.

2.2.1 Synthesis procedures

Samples of Te-rich $(Bi_{0.25}Sb_{0.75})_2Te_3$ were synthesized from solidus compositions (*SC*) of $(Bi_{0.25}Sb_{0.75})_2Te_{3+\delta}$ with δ in the range of 0 - 0.0585 and liquidus compositions (*LC*) of $(Bi_\alpha Sb_\beta)_2Te_{3+\delta}$ with $\beta/\alpha < 3$ and δ from 0 - 0.0585 as listed in Table 2.1. Elements of Bi, Sb, and Te (99.999 % purity metals basis) from Alfa Aesar were used to synthesize the *SC* and *LC* compounds separately. For both *SC* and *LC*, stoichiometric amounts of each element were weighed in air. They were then loaded into carbon coated quartz ampoules, and evacuated to a pressure of $\sim 10^{-5}$ Torr. The *SC* and *LC* (in sealed ampoules) were melted at 1073 K for 12 hours using a vertical tube furnace, and rapidly quenched in water. The obtained ingots were ground for 20 minutes using a mortar and pestle in an Argon glove box to prevent oxidation of the ground powders.

Table 2.1 Starting solidus and liquidus compositions for Te-excess $(Bi_{0.25}Sb_{0.75})_2Te_3$

Sample†	*LC*/*SC*‡	Bi (at. %)	Sb (at. %)	Te (at. %)
6.73E19	*LC*	18.00	22.00	60.00
	SC	10.00	30.00	60.00
4.57E19	*LC*	10.30	28.10	61.60
	SC	9.97	29.90	60.13
3.61E19	*LC*	10.30	28.10	61.60
	SC	9.92	29.78	60.30
3.57E19	*LC*	10.45	28.38	61.17
	SC	9.862	29.58	60.55
3.29E19	*LC*	10.45	28.38	61.17
	SC	9.862	29.58	60.55
2.64E19	*LC*	10.46	27.92	61.61
	SC	9.71	29.12	61.17

† Sample name = n_H of the resulting oriented crystal at 300 K. ‡ *LC* = liquidus composition, *SC* = solidus composition

To create the starting ingot for crystal growth, the resulting *LC* powder was melted (in a quartz tube under ~10^{-5} Torr) at 1073 K for 5 minutes, and quenched in water (Fig. 2.1a to 2.1c). The newly formed *LC* ingot (inside of the tube) was about 10 ~ 15 mm in length (green ingot in Fig. 2.1c). The top of the sealed quartz tube (with *LC* ingot still inside) was cut and *SC* powder (purple spheres) was placed on top of the *LC* ingot as shown in Fig. 2.1d. The quartz tube was vacuum sealed to ~10^{-5} Torr yet again. While keeping the *LC* ingot at room temperature, the *SC* powder (which slid to the bottom of the tube as the tube was held upside-down) was melted at 1073 K for 5 minutes (Fig. 2.1e). The upside-down quartz tube with melt *SC* was flipped and gently shaken once or twice to ensure that the melt *SC* flowed down to be in contact with the *LC* ingot. The instant that all the melt *SC* is on top of the *LC* ingot, the whole tube was quenched in water as in Fig. 2.1f. This “flip and quench” step, which took less than 5 seconds, formed an interface free of voids between the *LC* ingot (~10 mm in length) and *SC* ingot (~70 mm in length).

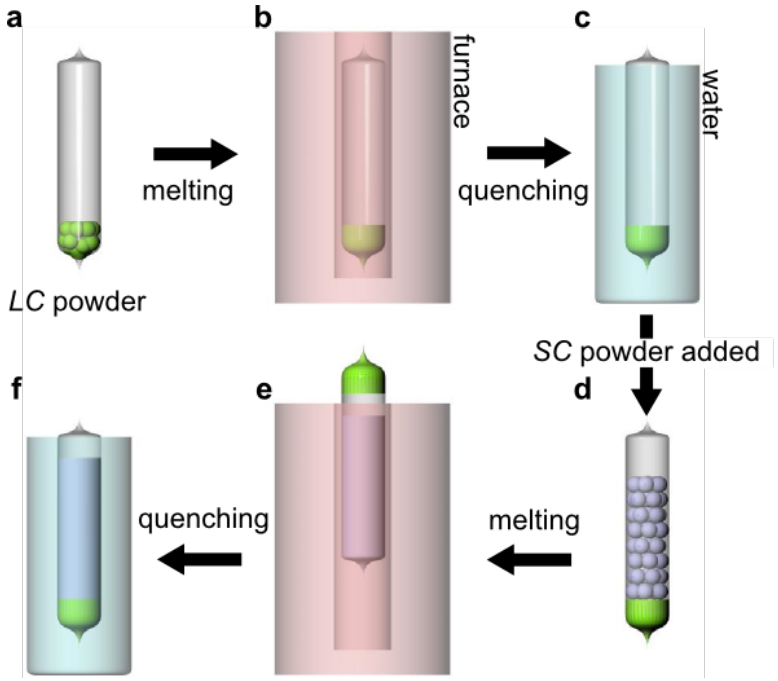

Fig. 2.1. Schematic description of preparing a sealed ampoule with two ingots with different compositions in contact for zone-melting.

The ampoule with *LC* ingot at the bottom and *SC* ingot on top (as in Fig. 2.1f and Fig. 2.2) was zone-levelled with a home-built vertical zone-levelling furnace[15] at 890 K with a solidification rate of 2.7 mm/hr. Temperature of the molten zone was measured by a pyrometer (Modline 5, Ircon). A temperature controller (UP550, Yokogawaka) controlled the power input to the induction coil to keep the molten zone temperature at 890 K. The length of the *LC* ingot (orange part in Fig. 2.2) was controlled to be approximately the length of the molten zone in the zone-levelling furnace by adjusting the amount of *LC* powder in Fig. 2.1a. As the molten zone passed through the *LC* ingot, the melt *LC* froze to a solid with a composition of *SC* ($k < 1$). Because the composition of frozen solid from the molten zone is the same as that fed into the molten zone (*SC* ingot), this zone-levelling resulted in oriented polycrystalline material with a homogeneous composition of *SC*.

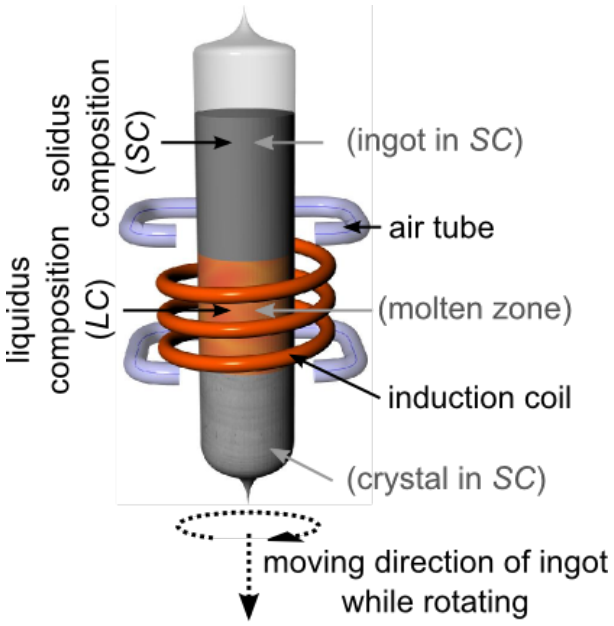

Fig. 2.2. Schematic diagram of zone-levelling apparatus.

2.2.2 Characterization

2.2.2.1 Composition characterization

An iterative process was employed to determine the compositions of *LC* and their corresponding *SC*. Each $(Bi_{\alpha}Sb_{\beta})_2Te_{3+\delta}$ powder (prepared as above) with different composition was melted (in a quartz tube under ~10^{-5} Torr) at 1073 K for 5 minutes, and quenched in water (as in Fig. 2.1a to 2.1c). Final ingots (40 mm in length) were zone-levelled at 890 K with a growth rate of 2.9 mm/hr. Composition of each crystal's region where the first solidification happened was examined by electron probe microanalysis (EPMA). Only those samples which melt and froze into Bi : Sb = 10 : 30 (at. %) with Te higher than 60 at. % (*SC*) were used as *LC* to synthesize $(Bi_{0.25}Sb_{0.75})_2Te_{3+\delta}$ oriented crystals (Table 2.1).

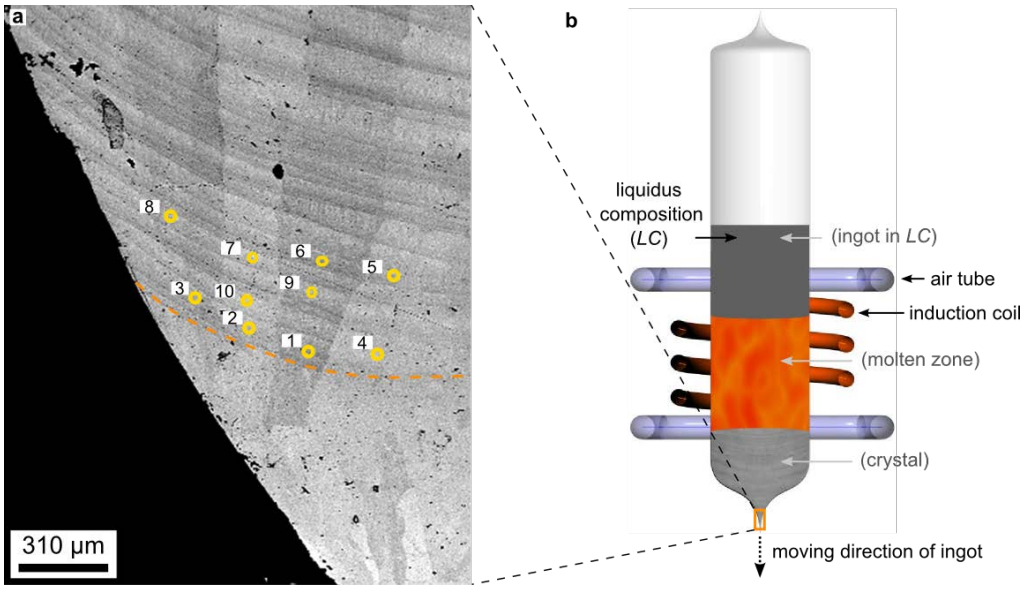

Fig. 2.3. Determination of liquidus compositions (*LC*) and their corresponding solidus compositions (*SC*). (a) Electron probe microanalysis (EPMA) on the *LC* of Bi : Sb : Te = 10.45 : 28.38 : 61.17 in at. % (see Table 2.1, sample "3.57E19" and "3.29E19"). Yellow circles and numbers indicate locations of composition measurements and the order of the measurements, respectively. Orange dotted line shows where texturing of the zone-melted crystal begins. This part of the crystal is from the tip of the zone-melted crystal as schematically represented in a cross-sectional view of the ingot being zone-melted (b).

For example, as a candidate for *LC*, an ingot with a composition of Bi : Sb : Te = 10.45 : 28.38 : 61.17 (in at. %) was zone-melted as in Fig. 2.3b. Unlike in Fig. 2.2, there was only one ingot (with *LC*) present in Fig. 2.3b which would result in changing composition of the zone-melted crystal along the height of the crystal. Therefore in order to accurately measure the freezing composition of the melted *LC*, electron probe microanalysis (EPMA) was done on the region where the molten zone was first started (orange square in Fig. S1b). The orange dotted line in Fig. 2.3a clearly defines the boundary between textured crystal (curved layers) and ingot (below the line). Since the start of the textured crystal corresponds to that of the molten zone, EPMA measurements from ten different spots (yellow circles in Fig. 2.3a) were taken from above the orange dotted line (but still close to the line). Those spots were deliberately chosen to be closer to the surface of the crystal as the cooling air (via air tube in Fig. 2.3b) first froze the melted ingot near the surface. According to the EPMA, the averaged (from ten data points) ratio of Sb to Bi was ~2.95 and the averaged Te was 60.55 at. %. As the freezing composition satisfied the two conditions of *SC*, $(Bi_{0.25}Sb_{0.75})_2Te_{3+\delta}$, the composition of Bi : Sb : Te = 10.45 : 28.38 : 61.17 (in at. %) and its freezing composition were adopted as

LC and *SC*, respectively. This combination of *LC* and *SC* was used in the samples "3.57E19" and "3.29E19" as listed in Table 2.1. After the sample "3.29E19" was synthesized, the same synthesis procedure was repeated to make "3.57E19" from the very beginning for a brief reproducibility test. All the *LC* used in Table 2.1, their freezing compositions estimated by EPMA are given in Table 2.2. For *SC* of the sample "4.57E19", the lower limit of the estimated Te (at. %) from the freezing composition was used.

Table 2.2. Freezing composition of each *LC* measured by EPMA.

Sample†	*LC*			freezing composition‡		*SC*		
	Bi (at. %)	Sb (at. %)	Te (at. %)	Bi : Sb	Te (at. %)	Bi (at. %)	Sb (at. %)	Te (at. %)
4.57E19	10.30	28.10	61.60	0.25 : 0.74 (±0.05)	60.30 (±0.17)	9.97	29.90	60.13
3.61E19	10.30	28.10	61.60	0.25 : 0.74 (±0.05)	60.30 (±0.17)	9.92	29.78	60.30
3.57E19 3.29E19	10.45	28.38	61.17	0.25 : 0.76 (±0.03)	60.55 (±0.14)	9.862	29.58	60.55
2.64E19	10.46	27.92	61.61	0.25 : 0.79 (±0.03)	61.16 (±0.54)	9.71	29.12	61.17

† Sample name = n_H of the resulting zone-levelled crystal at 300 K
‡ freezing composition = composition that melted *LC* ingots freeze into

2.2.2.2 Thermoelectric transport characterization

Parallelepiped shape samples (4.0×1.5×12.0 mm^3) were prepared for resistivity and Hall effect measurements under dynamic vacuum. A total of 5 contacts were made on the samples to measure the resistivity (via 4-point method) and Hall effect (with the 5^{th} contact at opposite side of resistance voltage contacts) at the same time without having to change contact geometry (Fig. 2.3). A modified MMR technologies variable temperature Hall measurement system with a 1.0 T field up to 520 K was utilized.

Disk shape samples (6.0 mm diameter and 1.5 mm thick) cut from one end of the zone-levelled ingot piece for the parallelepiped samples were used in the Seebeck coefficient (house built)[16] and thermal diffusivity (via Netsch LFA 457) measurements.

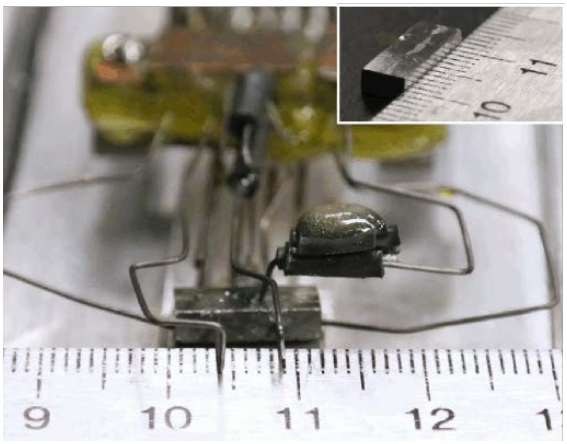

Fig. 2.4. Picture of a parallelepiped shape sample set up for electrical resistivity and Hall coefficient measurement. Inset shows the sample alone.

2.2.3 Two-band transport model

A two-band (TB) model was employed to compute transport properties of the zone-levelled $(Bi_{0.25}Sb_{0.75})_2Te_{3+\delta}$ samples at 300 K. For each nonparabolic band, Boltzmann transport equations (as functions of chemical potential) were numerically solved (in Python) to obtain chemical potential dependent thermoelectric parameters (i.e. Seebeck coefficient, mobility, etc.) while assuming acoustic phonon scattering[17] and alloy scattering[18] (except Bi_2Te_3 and Sb_2Te_3). The resulting transport properties from the two valence bands (VB_1 and VB_2 in Fig. 3.1d) were calculated by taking conductivity-weighted averages of the thermoelectric parameters of each band[19].

The energy gaps between the lowest conduction band (*CB*) and the highest valence band for $0 \leq x \leq 0.75$ (VB_1) used in the TB model were taken from Sehr *et al.*[20] (Fig. 3.1d and $\Delta E_{CB\text{-}VB1}$ in Table 2.3). For $x > 0.75$, the $\Delta E_{CB\text{-}VB1}$ was linearly extrapolated to minimize complexity. The density-of-states effective mass (m^*) and deformation potential (E_{def}) for each valence band at $x = 0$ and $x = 1$ were fitted to experimental data from literatures while adjusting their energy differences between *CB* and VB_2 ($\Delta E_{CB\text{-}VB2}$). Because it was assumed that the bands were crossing at $x = 0.75$, we knew $\Delta E_{CB\text{-}VB2}$ at $x = 0.75$ ($\Delta E_{CB\text{-}VB2} = \Delta E_{CB\text{-}VB1}$). The $\Delta E_{CB\text{-}VB2}$ at $x = 0.75$ and those determined from $x = 0$ and 1 could approximately be joined in a straight line. Therefore, the $\Delta E_{CB\text{-}VB2}$ for other x were obtained from the straight line (Table 2.3). For $0.75 < x \leq 1$, the

highest valence band is the VB_2 and the $\Delta E_{CB\text{-}VB2}$ serves as the energy gap (between the lowest CB and the highest valence band). The fitted energy gap at $x = 1$ used in the model (0.2007 eV of $\Delta E_{CB\text{-}VB2}$ in Table 2.3) is about 16 % smaller than degeneracy-corrected optical energy gap from Sehr *et al.*[20] (reasonable given the tendency to overestimate the optical energy gap as degeneracy increases)[21].

Based on the band structure information ($\Delta E_{CB\text{-}VB1}$ and $\Delta E_{CB\text{-}VB2}$) obtained from the literature and the fitting to the experimental literature data of $x = 0$ and 1, the m^* and E_{def} of each band for $0 < x < 1$ were determined while controlling the alloy scattering potential U (Table 2.3). The U describes the magnitude of the alloy scattering in an alloy. The relaxation time equation for the alloy scattering from Heng *et al.*[18] was used in the TB model. The total relaxation time was calculated by Matthiessen's rule: $\tau_{total}^{-1} = \tau_{ac}^{-1} + \tau_{alloy}^{-1}$, where τ_{ac} and τ_{alloy} are the relaxation times for acoustic phonon scattering and alloy scattering, respectively. A constant U of 0.35 eV was used for all x except $x = 0$ and 1 (where the alloy scattering was absent).

Table 2.3. Band parameters used in the two-band transport model.

x[†]	VB_1 (the first valence band)					VB_2 (the second valence band)					$\Delta E_{VB1\text{-}VB2}$ (meV)	U[ǂ] (eV)	C_l[§] (GPa)
	m^* (m_e)	E_{def} (eV)	$\Delta E_{CB\text{-}VB1}$[‖] (eV)	N_V	$m_\parallel^*/m_\perp^*$[‡]	m^* (m_e)	E_{def} (eV)	$\Delta E_{CB\text{-}VB2}$ (eV)	N_V	$m_\parallel^*/m_\perp^*$			
0.00	0.760	14.36	0.1442	6	2.56	0.800	28.09	0.1742	6	1.00	30.0	0.00	64.04
0.20	0.750	15.61	0.1575	6	2.26	0.775	28.09	0.1795	6	1.00	22.0	0.35	62.19
0.33	0.730	13.42	0.1661	6	2.79	0.768	25.03	0.1829	6	1.00	16.8	0.35	60.97
0.50	0.728	15.29	0.1775	6	2.46	0.750	25.16	0.1875	6	1.00	10.0	0.35	59.38
0.60	0.725	15.79	0.1841	6	2.42	0.740	23.72	0.1901	6	1.00	6.0	0.35	58.44
0.67	0.720	16.85	0.1888	6	2.48	0.728	22.78	0.1920	6	1.00	3.2	0.35	57.78
0.75	0.733	17.54	0.1941	6	1.00	0.710	18.10	0.1941	6	2.29	0.0	0.35	57.03
0.80	0.730	21.85	0.1974	6	1.00	0.700	18.10	0.1954	6	2.35	-2.0	0.35	56.56
0.85	0.725	23.41	0.2007	6	1.00	0.689	17.79	0.1967	6	2.55	-4.0	0.35	56.09
0.90	0.730	25.16	0.2041	6	1.00	0.681	17.48	0.1981	6	2.55	-6.0	0.35	55.61
1.00	0.722	25.28	0.2107	6	1.00	0.670	14.98	0.2007	6	2.59	-10.0	0.00	54.67

[†] Composition x in $(Bi_{1-x}Sb_x)_2Te_3$.

[‖] $\Delta E_{CB\text{-}VB1}$ = Energy difference between conduction band (CB) and the first valence band (VB_1).
Similarly, $\Delta E_{VB1\text{-}VB2}$ denotes the energy difference between the first and second valence bands.

[‡] $m_\parallel^*/m_\perp^*$ = Parameter describing the anisotropy of a single band.
$m_\parallel^*$ and $m_\perp^*$ are effective masses along longitudinal and transverse ellipsoid directions, respectively.
The ratios of $m_\parallel^*$ to $m_\perp^*$ for different compositions (x) are calculated from ref. 22.

[ǂ] U = Alloy scattering potential. [§] C_l = elastic constant.

Anisotropy of the bands was also taken into account in the TB model. Stordeur *et al.*[22] have optically measured effective masses along longitudinal ($m_{\parallel}$*) and transverse ($m_{\perp}$*) ellipsoid directions. However, since Stordeur *et al.* assumed that only a single band was participating in transport only composition-dependent $m_{\parallel}$* and $m_{\perp}$* for a single valence band was available. Thus, only the highest valence band (VB_1 for $0 \leq x \leq 0.75$ and VB_2 for $0.75 < x \leq 1$) was treated as anisotropic (Table 2.3). The second highest band was assumed to be isotropic for simplicity ($m_{\parallel}*/m_{\perp}* = 1$ for an isotropic band).

The elastic constants ($C_l = d \times v_l^2$ where d and v_l are the density and the longitudinal sound velocity, respectively) of Bi_2Te_3 ($x = 0$) and Sb_2Te_3 ($x = 1$) were calculated from the d and v_l of $x = 0$ ($d = 7700$ kg/m^3 and $v_l = 2143$ m/s from ref. 23,24) and $x = 1$ ($d = 6500$ kg/m^3 and $v_l = 2333$ m/s from ref. 23,24). The C_l for the rest x were linearly interpolated between those of $x = 0$ and 1 (Table 2.3).

As shown in Figs. S4, S5, and S6, band parameters used in the TB model (Table 2.3) yielded satisfactory fits to the experimental literature data at 300 K. However, equally adequate fits may be obtained for different sets of parameters. Nonetheless, the underlying physics of the measured transport properties in $(Bi_{1-x}Sb_x)_2Te_3$ single/oriented crystals is satisfactorily captured in the fits provided by the TB model.

2.3 Spark Plasma Sintering (SPS) for $(Bi_{0.25}Sb_{0.75})_2Te$

2.3.1 Synthesis procedures

The $Bi_{0.5}Sb_{1.5}Te_3$ ingots were prepared with a melt process; high-purity (> 99.999 %) Bi, Sb, and Te granules were weighed according to the composition $Bi_{0.5}Sb_{1.5}Te_3$ and loaded into a vacuum-sealed quartz tube of 10 mm diameter, and the contents were melted and homogeneously mixed in a rocking furnace for 10 h at 1073 K.

$Bi_{0.5}Sb_{1.5}Te_3$ bulk ingots were pulverized and mixed with excess Tellurium (25 wt. %), then the homogeneously mixed materials were put into a quartz cylinder with 0.3 mm diameter nozzle in melt spinning system. The materials were induction-molten, and were injected under a pressure of 40 kPa Ar onto a Cu wheel rotating with linear speed of 45 ms^{-1} under the Ar atmosphere of 300 mTorr. Thin ribbons (5–10 μm thick, 1.5–2 mm wide, and 5–10 mm long) were obtained by rapid solidification (cooling rate ~106 Ks^{-1}) using this melt spinning process.

The melt spun ribbons were pulverized, then compacted using spark plasma sintering (SPS) at 480 °C for 3 min under 70 MPa. During the compacting, the liquidified excess Te was expelled from the graphite die.

Fig. 2.5. Picture of excess Te expelled from the graphite die after the SPS process.

2.3.2 Characterization

X-ray diffraction (XRD) (D/MAX-2500/PC, Rigaku, Japan) analysis with Cu K_α radiation (λ = 1.5418 Å) was performed on powder and bulk samples. The microstructure was investigated using scanning electron microscopy (SEM) (JSM-7600F, JEOL) and transmission electron microscope (TEM) (JEM-2100F, JEOL). Transport measurements were performed in directions both parallel and perpendicular to the pressing direction. Only the measurements perpendicular to the pressing directions are shown in the main text and used for calculation of *zT*. The electrical conductivities (σ) and Seebeck coefficients (*S*) were measured from 300 to 480 K by a four point probe method using a ZEM-3 (ULVAC-RIKO, Japan). Hall effect

measurements were performed using Physical Property Measurement System (Quantum Design). The thermal conductivity values ($\kappa = \rho_s \times C_p \times \lambda$) were calculated from measurements taken separately. Sample density (ρ_s) was measured by Archimedes method. The thermal diffusivity (λ) was measured by laser-flash method using TC-9000 (ULVAC-RIKO, Japan). The Dulong-Petit heat capacity (C_p = 124.6 J mol^{-1} K^{-1}) was used and confirmed by measurements at 300 K by the thermal relaxation method using a Physical Property Measurement System (Quantum Design).

Chapter 3

Convergence of valence bands in $(Bi_{0.25}Sb_{0.75})_2Te_3$

This section contains contents that have been submitted to a journal. Once it is accepted, permission will be asked.

3.1 Introduction

Since commonly used refrigerants (hydrochlorofluorocarbons) were identified as ozone-depleting, there has been a worldwide agreement to eliminate their production by 2030[7]. Progress towards this task can be aided if current vapor-compression cooling is replaced by environmentally sustainable thermoelectric cooling. The development of high-efficiency thermoelectric material, whose performance is evaluated by its figure of merit, $zT = S^2\sigma T/\kappa$, where S, σ, T, and κ are the Seebeck coefficient, electrical conductivity, temperature, and the thermal conductivity, respectively, is essential to make thermoelectric refrigerators more competitive than their ozone-depleting counterparts.

For decades, *p*-type Bi_2Te_3-Sb_2Te_3 alloys have been the best candidates for cooling applications because of their high zT near room temperature[10]. Among single-crystal $(Bi_{1-x}Sb_x)_2Te_3$, the composition near $x = 0.75$ has been found to have the maximum zT (0.87 – 0.9 at 300 K)[12,25]. Since then, many efforts have focused on nanostructured polycrystalline $(Bi_{0.25}Sb_{0.75})_2Te_3$ to improve the zT by κ reduction[1,26-28].

In order to further enhance zT in $(Bi_{0.25}Sb_{0.75})_2Te_3$, optimizing both the thermal and electronic properties will be required. Recently, a high zT (1.86 at 320 K) was reported in $(Bi_{0.25}Sb_{0.75})_2Te_3$ from phonon engineering through dislocations[1]. This material is made with excess Te and lower hole concentration than typical materials of the same nominal composition[1], suggesting charge carrier optimization may also have been involved. The maximum attainable electronic performance of a thermoelectric material is proportional

to the quality factor[29], which in turn depends on the number of Fermi pockets (N_v)[13,30]. Because N_v is not coupled to any other property related to zT, converging separate carrier pockets provides a straightforward strategy for improving zT (ref. 30). To date, band convergence in $(Bi_{1-x}Sb_x)_2Te_3$ has not been sufficiently investigated, probably because many experiments assumed only one band participating in transport[12,31-33] despite the fact that it has a high crystal symmetry like PbTe.

Using a single band model, the density-of-states effective mass (m^*) for the valence band can be calculated from the Seebeck Pisarenko plot (S versus Hall carrier concentration) for each composition. A peak was found in m^* at $x = 0.75$ (ref. 34,35) as shown in Fig. 3.1a. Optical investigations[22] of single-crystal $(Bi_{1-x}Sb_x)_2Te_3$ confirmed the m^* peak at $x = 0.75$ and concluded this was due to an increase in mass along one direction only near $x = 0.75$. Unfortunately, the single band theory could not explain the abrupt change in the effective mass[33].

Here we propose, providing additional evidence, that the high zT at $x = 0.75$ is not due to sudden flattening of the valence band to increase m^*, but instead is due to the convergence of the two different valence bands that cross as x changes (Fig. 3.1d). We develop a two-band transport model for $(Bi_{1-x}Sb_x)_2Te_3$ alloys that predicts an improvement in zT when the carrier concentration of $(Bi_{0.25}Sb_{0.75})_2Te_3$ is carefully tuned. Preparing homogeneous, crystalline material by zone-melting, we observe a zT of ~1.05 at 300 K. This value is significant when compared to the state-of-the-art single-crystal $(Bi_{0.25}Sb_{0.75})_2Te_3$ ($zT \leq 0.9$), as it is achieved without nanostructuring or external doping.

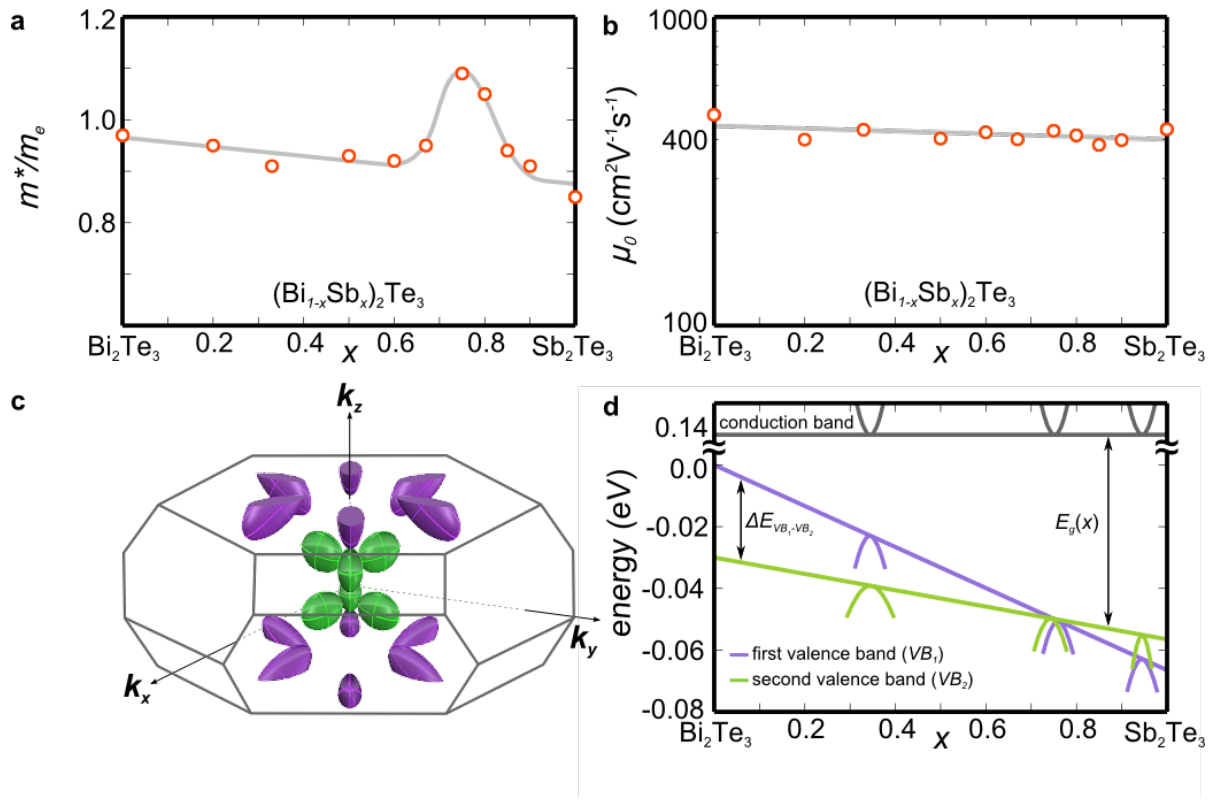

Fig. 3.1. Band related properties as a function of composition (x) for $(Bi_{0.25}Sb_{0.75})_2Te_3$ at 300 K. (a) Density-of-states effective mass (red circle) showing an abrupt peak (grey line as guide to the eye) while the mobility prefactor (b) shows no such change at x = 0.75. (c) Brillouin zone of Bi_2Te_3 (x = 0) showing hole pockets for the first valence band (in purple) and for the second valence band (in green). (d) Semi-empirical band structure (300 K) with the first valence band (purple line), second valence band (green line), and the lowest conduction band (dark grey line). For simplicity, the energy of the first valence band (purple) of Bi_2T_3 (x = 0) is set to 0.0 eV. $\Delta E_{VB1\text{-}VB2}$ denotes energy difference between the first and second valence bands. The energy gap between the lowest conduction band (dark grey) and the highest valence band (purple for $0 \le x \le 0.75$ and green for $0.75 \le x \le 1$) is the band gap $E_g(x)$.

3.2 Experimental

In order to understand band structure of $(Bi_{1-x}Sb_x)_2Te_3$ with pronounced anisotropy[36], the transport properties carefully measured from its textured or single crystal along the same direction are required. Among various methods to grow textured and/or single crystals, simple solidification from the melt (Bridgman method) works well for congruently melting systems, but for alloys this will generally produce materials with a composition gradient as the material solidifies and the composition of the liquid phase changes[37]. This is due to the composition difference between the solid and liquid phase at the growth

temperature characterized by the segregation coefficient k (concentration of a particular component in solid phase divided by that in the liquid phase)

Zone-levelling (shown schematically in Fig. 3.2) is ideal for producing homogeneous crystals in systems with segregation coefficients not equal to unity ($k \neq 1$)[38]. Unlike the Bridgman method where the entire molten ingot solidifies from end to end, in zone-levelling only a portion (or zone) of the ingot is in the molten state at any given time. The compressed air flowing below and above the molten zone ensures sufficient temperature gradients for solidification and a smooth liquid-solid interface (Fig. 3.2a). The two regions of different compositions (solute concentration) in the ingot before the zone-levelling is depicted with a blue dashed line in Fig. 3.2b. The initial composition is the liquidus composition (*LC*) C_0/k at the bottom of the ingot (with a length the size of the molten zone) and solidus composition (*SC*) C_0 for the remainder of the ingot. These compositions correspond to liquidus and solidus composition in the ternary phase diagram of Bi-Sb-Te system at the growth temperature of 890 K (since $k < 1$ for $(Bi_{0.25}Sb_{0.75})_2Te_3$, $C_0 < C_0/k$). When the zone-levelling is performed on this ingot, the crystal has a solute concentration of C_0 (*SC*) throughout the crystal as liquid *LC* freezes to *SC* except at the top of the crystal where the molten zone is stopped (blue solid line in Fig. 3.2b). Therefore, it is particularly important to control the initial liquid-solid interface to coincide with the *LC-SC* junction (between orange and grey regions of the ingot in Fig. 3.2a). For $k \neq 1$, the normal freezing method (i.e. Bridgman method) would result in a gradually changing solute concentration (green solid line in Fig. 3.2b) and not a homogeneous ingot with the desired composition C_0.

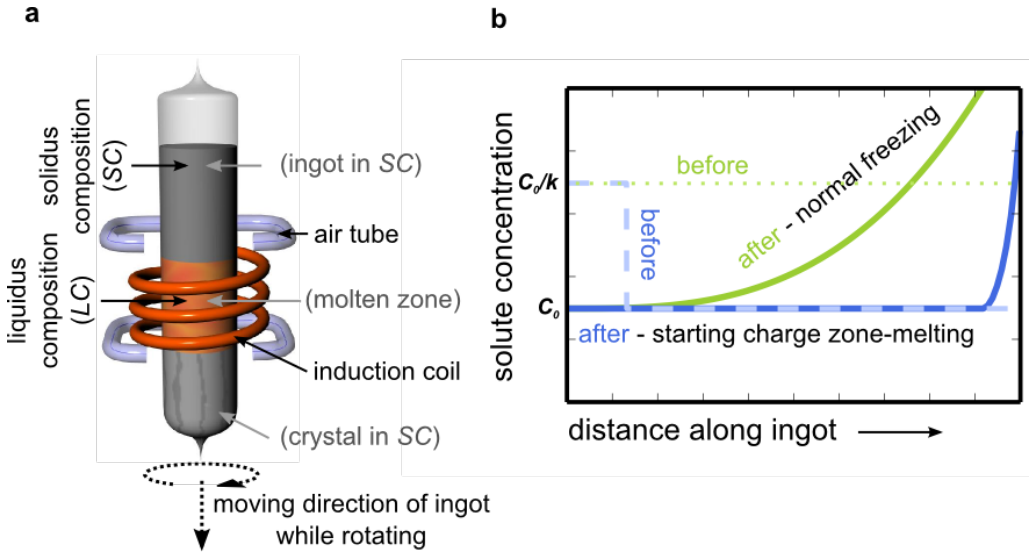

Fig. 3.2. Apparatus and method of zone-levelling. (a) Schematic diagram of zone-levelling apparatus. A sealed ampoule with an ingot of liquidus composition (*LC* in orange) and another ingot of solidus composition (*SC* in grey) in contact is positioned at the center of induction coil. The *LC* and *SC* correspond to solute concentration of C_0/k and C_0 in Fig. 2b, respectively. All the *LC* ingot is currently in molten state (part of ingot in orange is within the induction coil). For uniform mixing of solute, the sealed ampoule rotates while moving downwards in a constant rate. (b) Concentration profile for the zone-levelling method compared to normal freezing (Bridgman method). Solute concentration of an ingot before zone-levelling is shown in blue dashed line. That of another ingot before normal freezing is in green dotted line. Resulting solute concentrations of crystals after zone-levelling and normal freezing are expressed in blue and green solid lines, respectively.

Although pseudo-binary phase diagram for Bi_2Te_3–Sb_2Te_3 can be found in literature[12], in order to tune hole carrier concentration with excess Te in $(Bi_{0.25}Sb_{0.75})_2Te_{3+\delta}$ a ternary phase diagram of Bi-Sb-Te is required. However, because a sufficient Bi-Sb-Te ternary phase diagram is not available (only the liquidus projection has been studied) numerous melted ingots with a single composition have been solidified to characterize their solid (frozen) compositions. Only those ingots (*LC*) which freeze (after being melted) to $(Bi_{0.25}Sb_{0.75})_2Te_{3+\delta}$ (*SC*) are presented in this paper. Preparing a sealed ampule with both ingots of *LC* and *SC* is illustrated in Fig. 3.3.

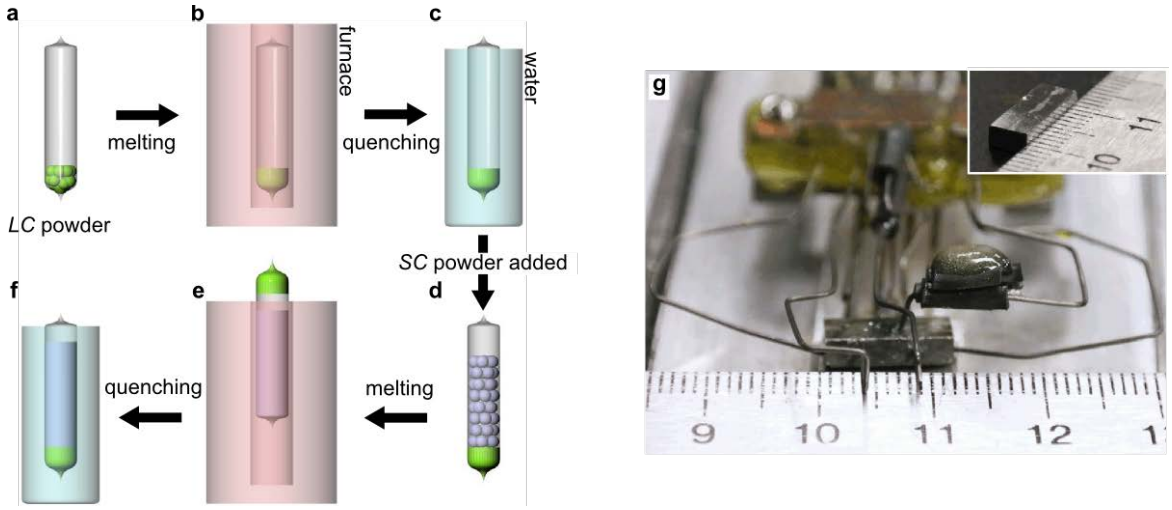

Fig. 3.3. Schematic description of preparing a sealed ampoule with two ingots with different compositions in contact for zone-levelling and picture of cut crystal after zone-levelling. All the sealed ampoules from Fig. 3.3a to 3.3f are under vacuum. Powder is depicted in spheres. Once the powder is melted in furnace (3.3b) and quenched in water an ingot is formed as in 3.3c. Top of the ampoule in 3.3c is cut and *SC* powder is poured on top of the *LC* ingot (3.3d). Only *SC* powder is melted while keeping the *LC* ingot in room temperature (3.3e). The ampoule in 3.3e is inverted upside down for the melted *SC* to flow down to *LC* ingot. As soon as the melted *SC* is in contact with the *LC* ingot the entire ampoule is quenched in water to prepare a sealed ampoule with *LC* and *SC* in contact (3.3f). Picture of a parallelepiped shape sample set up for electrical resistivity and Hall coefficient measurement (3.3g). Inset shows the sample alone.

Parallelepiped ($4\times1.5\times12$ mm^3) and disk shape samples (6 mm diameter and 1.5 mm thick) were cut from the zone-levelled crystals for electrical resistivity, Hall effect, Seebeck coefficient, and thermal conductivity measurements along the growth direction. The parallelepiped shape sample mounted on an apparatus for measuring electrical resistivity and Hall coefficient is shown in Fig. 3.3g.

3.3 Two valence band behavior in *p*-type $(Bi_{1-x}Sb_x)_2Te_3$

The band structure of Bi_2Te_3 and Sb_2Te_3 has been extensively studied[36,39-42] showing the bands and Fermi surfaces are clearly complex with several distinct band extrema off the high symmetry points (all on the plane containing the G, Z, U, A, F, L points). The combination of complex band structure and anisotropic Fermi pockets (Fig. 3.1c) found in Bi_2Te_3 contributes to the high S and σ at the same time[14]. Different density functional theory (DFT) methods predict different energies for the different band extrema. Based on locations of valence band edges[40,42] and calculated hole mass tensor parameters associated with the valence band edges[42], Fermi pockets of Bi_2Te_3 are illustrated as in Fig. 3.1c. The second valence band (VB_2, green ellipsoids in Fig. 3.1c) close to the first valence band (VB_1, purple ellipsoids) in energy is also shown

(calculated $\Delta E_{VB1\text{-}VB2}$ is 27 meV from ref. 42 and 3.8 meV from ref. 40 – our fitted $\Delta E_{VB1\text{-}VB2}$ is 30 meV as in Fig. 3.1d). Because both hole pockets for VB_1 and VB_2 lie in a mirror plane of Bi_2Te_3 Brillouin zone (k_y-k_z plane in Fig. 3.1c), they both have three-fold rotation and inversion symmetry; by being off the Γ–Z line their degeneracies are $N_v = 6$.

Here we propose a schematic band structure of $(Bi_{1-x}Sb_x)_2Te_3$ alloys with two valence bands contributing to transport, contrary to previous reports in which only a single valence band was considered[22,34,35]. After Drabble showed that a model assuming one valence band with $N_v = 6$ could be made to fit galvanomagnetic measurements on single crystal of *p*-type Bi_2Te_3 ($x = 0$)[13], the band structure of even other compositions was assumed to have a single valence band. Gaidukova *et al*.[35] determined the density-of-states effective mass (m^*) from measured Seebeck data of the alloys ($0.5 \leq x \leq 1$) using the Single Parabolic Band (SPB) model[8]. When the m^* was plotted against the composition (x), a peak was observed at $x = 0.75$. A similar result was reported by Stordeur *et al*.[22] where the m^* and its components along different directions in k-space (as a function of x) were calculated from thermoelectric transport data and reflection spectra concluding that the single valence band suddenly becomes heavy in one direction.

To understand the cause of the maximum m^* at $x = 0.75$, we have first conducted semi-empirical SPB modelling[8] on experimental Seebeck coefficient (S) and the Hall mobility (μ_H) from the literature ($0 \leq x \leq 1$) and the samples prepared here ($x = 0.75$) to extract single band m^* and intrinsic mobility (μ_0, which scales with μ_H) for different x (Fig. 3.1a and 3.1b). Because of the marked anisotropy of the layered structure of $(Bi_{1-x}Sb_x)_2Te_3$ (i.e., hexagonal crystal system)[36], only the S and the μ_H measured perpendicular to the trigonal axis of single-crystal samples (c-axis in the hexagonal system) were used in the modelling (the zT perpendicular to the c-axis is higher than that along the c-axis[11]).

The fact that the μ_0 does not change dramatically with x like m^* suggests that this is not due to a change in mass of a single band (Fig. 3.1b). This is because the mobility is not only inversely proportional to the inertial effective mass in the direction of transport (*a*-*b* plane) but also inversely proportional to the density

of states mass $m_b^{*3/2}$ of electron states it can scatter into (deformation potential e.g. acoustic phonon scattering dominates)[29].

For a Fermi surface consisting of N_V equivalent conducting carrier pockets (or valleys in the band structure) each with density-of-states mass, m_b^*, the overall equivalent density of states mass is given by $m^* = N_V^{2/3} m_b^*$. Thus μ_0 directly reflects the shape of the band around a charge carrier regardless of the total number of conducting bands while m^* is a measure of the total density of states including the number of bands contributing.

According to Fig. 3.1a, where the m^* peaks at $x = 0.75$ (equivalent to previous results[22,35]), it can be said that N_V or m_b^* (or even both) peaks around $x = 0.75$. The absence of a dip in μ_0 at $x = 0.75$ (Fig. 3.1b) eliminates the possibility of m_b^* increasing at $x = 0.75$ but instead suggests that the increase in m^* is a result of the N_V peaking around $x = 0.75$.

We postulate that convergence of two valence bands is responsible for the high N_V at $x = 0.75$. The existence of the second valence band has been reported for both Bi_2Te_3 ($x = 0$)[43-45] and Sb_2Te_3 ($x = 1$)[46-50] from Shubnikov–De Haas measurements. Although ΔE between the first and second valence bands at $x = 0$ (15 meV)[44] and $x = 1$ (150 meV)[47] were also deduced, because these values were estimated at a low temperature (4.2 K) they could be significantly different at 300 K. Band movements with temperature of this magnitude are observed in PbTe[51]. Therefore we only assume that the VB_1 (purple line in Fig. 3.1d) and the VB_2 (green line in Fig. 3.1d) cross each other at $x = 0.75$ (for simplicity, energies of both bands are assumed to vary linearly with composition x). The energy difference between VB_1 and VB_2 at $x = 0$ and $x = 1$ are fitted ($\Delta E_{VB1\text{-}VB2}$ in Fig. 3.1d).

Besides $\Delta E_{VB1\text{-}VB2}$, the composition-dependent energy band gap $E_g(x)$ between the lowest conduction band and the highest valence band was required to construct the band diagram for $(Bi_{1-x}Sb_x)_2Te_3$ (Fig. 3.1d). The true optical energy band gap (at 300 K) utilized here is from Sehr and Testardi[20]. They estimated it by subtracting the Burstein–Moss shift from the observed energy band gap. As the intrinsic hole carrier density

increases rapidly as x gets close to 1, this correction increases and with it the uncertainty in the optical gap[21]. Sehr and Testardi's data only for $0 \leq x \leq 0.75$ were used. Based on the $E_g(x)$ ($0 \leq x \leq 0.75$), two fitted $\Delta E_{VB1\text{-}VB2}$ (at $x = 0$ and 1), and proposed band convergence at $x = 0.75$ ($\Delta E_{VB1\text{-}VB2} = 0$) the energies of the two bands for other compositions were extrapolated as in Fig. 3.1d.

3.4 Transport properties calculated by the two-band model

We incorporated the band structure information given in Fig. 3.1d into multi-band and nonparabolic-band[52] (due to its narrow energy band gap[22,45]) modelling of the thermoelectric properties of $(Bi_{1-x}Sb_x)_2Te_3$. Approximately linearly varying density-of-states effective mass (m^*) and deformation potential ($\Xi \propto \mu_0^{-1/2}$) throughout the composition (x) for each valence band were determined by fitting them to S and μ_H (both as functions of n_H for $0 \leq x \leq 1$) under the acoustic phonon scattering and alloy scattering assumptions (Fig. 3.4a). A constant valley degeneracy (N_V) of 6 was used in all x for both valence bands[40,53,54] (see Fig. 3.1c). Anisotropy in the Fermi pockets ($m_\parallel^*/m_\perp^* \neq 1$, where $m_\parallel^*$ and $m_\perp^*$ are effective masses along the longitudinal and transverse ellipsoid direction, respectively) of $(Bi_{1-x}Sb_x)_2Te_3$ (Fig. 3.1c), which was obtained by Stordeur *et al.*[22] was included in the two-band (TB) modelling. Stordeur *et al.*[22] assumed that a single valence band ($N_V = 6$) contributed to transport to calculate the anisotropy. Thus the anisotropy was only adopted in the highest valence band in Fig. 3.1d (VB_1 for $0 \leq x < 0.75$ and VB_2 for the rest x). Lastly, the μ_H reduction due to alloy scattering was also taken into account for alloy compositions (except $x = 0$ and 1)[18]. The TB model results (orange line in Fig. 3.4b and 3.4c), those of the SPB model (green line), and experimental data are given in Fig. 3.4b and 3.4c for $x = 0.75$. Even though both TB model and SPB model closely followed the measured S in all n_H, the TB model was slightly better at describing measured μ_H at $n_H > 10^{20}$ cm^{-3}.

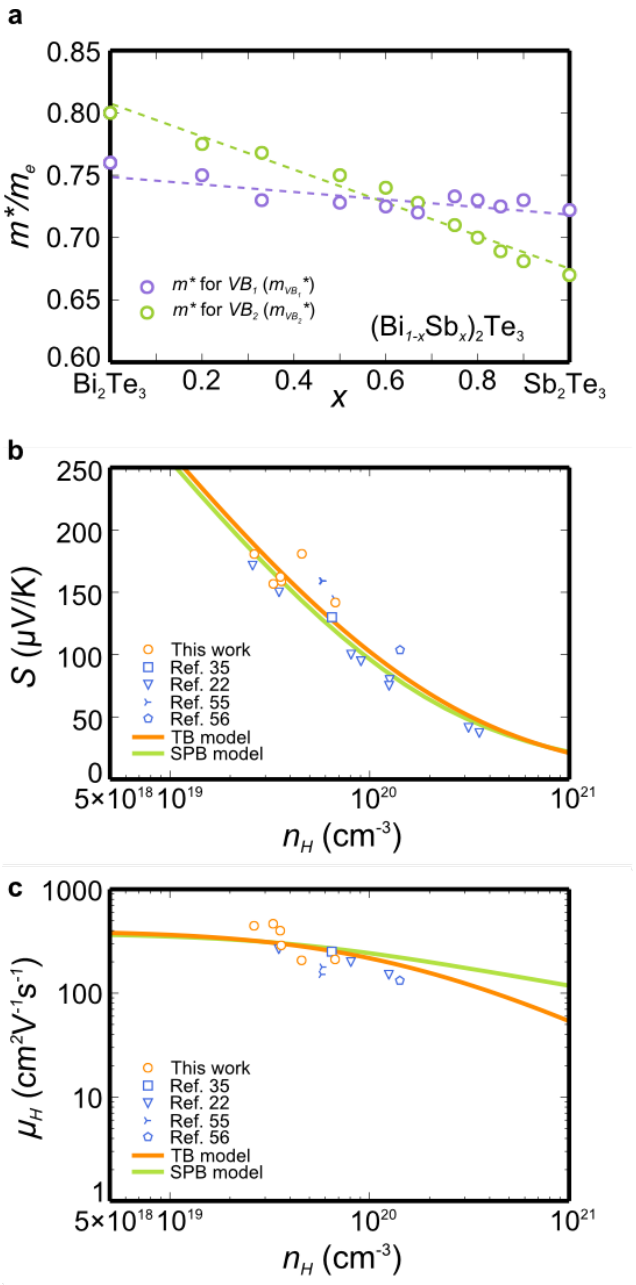

Fig. 3.4. Two-band related property as a function of composition (x) and transport properties as a function of Hall carrier concentration (n_H) for $(Bi_{0.25}Sb_{0.75})_2Te_3$ at 300 K. (a) Density-of-states effective masses (m^*) used in the two-band (TB) model to calculate Seebeck coefficient (S) (b) and Hall mobility (μ_H) (c). The TB model (orange line) was fitted to the experimental results (empty circles in orange) and the literature data from Ref. 35, 22, 55, and Ref. 56 (empty shapes in blue). The result of SPB model (green line) was also plotted for comparison.

Calculated density-of-states effective masses (m^*) for both bands in the TB model (Fig. 3.4a) decrease linearly with x (Fig. 3.4a). It should be noted that, for example at $x = 0$, m_{VB2}^* is heavier than m_{VB1}^* (Fig. 3.4a) but VB_2 is lower than VB_1 in energy (Fig. 3.1d). The m_{VB1}^* and m_{VB2}^* decrease only by ~5 % and

~15%, respectively, as x increases from 0 to 1. The greater change in m_{VB2}* allows the lower energy valence band (m_{VB2}* for $0 \leq x < 0.75$ and m_{VB1}* for the rest x) to stay heavier than the highest band for all x (Fig. 3.4a and 3.1d) despite the bands crossing at $x = 0.75$. Literature on the band parameters of the first and second valence bands in $(Bi_{1-x}Sb_x)_2Te_3$ was scarce to support the reliability of the TB model for all compositions (x). For example, Sologub *et al.*[53] could not determine relative energies of the two bands in Bi_2Te_3 despite the band parameters acquired for both bands from galvanomagnetic measurements. However, Köhler *et al.*[48] tentatively extrapolated the m* of the highest valence band for $0 \leq x \leq 0.6$ (0.3 m_e) up to x = 1 with a brief mention of the m* in the second valence band being comparable to that estimated for Bi_2Te_3 ($x = 0$) by von Middendorff and Landwehr[44] for all x (1.25 m_e). In spite of the fact that the extrapolation of both the m* to $x = 1$ was based on a tentative assumption, we could at least find that the second band being heavier than the first band at $x = 0$ was in agreement with our results. For $x = 0$, Kulbachinskii *et al.*[57] and Biswas *et al.*[43] confirmed that the second valence band was heavier than the first band. While the m* of the highest valence band in Sb_2Te_3 ($x = 1$) was deduced by von Middendorff *et al.*[47], the lack of information on the m* of the second band made direct comparison of the literature and our study difficult. Nonetheless, the m* of the second band (m_{VB1}* at $x = 1$ in Fig. 4a) being heavier than that of first band (m_{VB2}*) at $x = 1$ was also reported by Kulbachinskii *et al.*[58].

3.5 Optimizing the zT at 300 K via carrier concentration control

The carrier concentration of $(Bi_{0.25}Sb_{0.75})_2Te_3$ was controlled via the amount of excess Te. Based on the TB model and the lattice thermal conductivity taken from Goldsmid[59], the zT (for $x = 0.75$) was predicted as in Fig. 3.5 (orange solid line) with its maximum of 1.03 at $n_H = 1.3\times10^{19}$ cm^{-3} (300 K). However, when stoichiometric $(Bi_{0.25}Sb_{0.75})_2Te_3$ was synthesized with the liquidus composition (*LC*) of Bi : Sb : Te = 18 : 22 : 60 in at. %, and solidus composition (*SC*) of Bi : Sb : Te = 10 : 30 : 60 (at. %) in reference to the pseudo-binary phase diagram[12] of Bi_2Te_3–Sb_2Te_3 the resulting n_H was close to 6.7×10^{19} cm^{-3} (with $zT \approx$

0.6). As an excess Te should suppress Sb_{Te} antisite defects that produce holes[12] and hence increase *S*, attempts to produce homogenous $(Bi_{0.25}Sb_{0.75})_2Te_3$ oriented crystals with excess Te were made. As the complete ternary phase diagram including solidus and liquidus tie-lines is not known, the compositions used resulted from an iterative process.

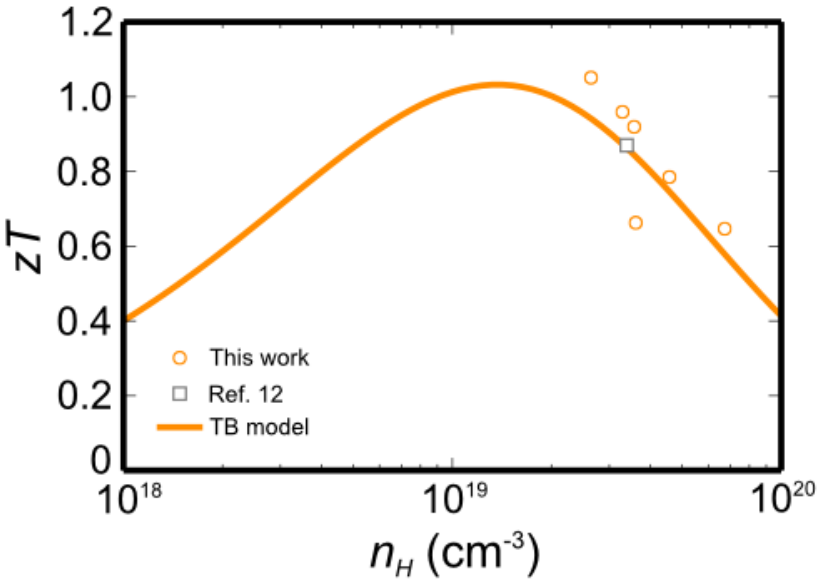

Fig. 3.5. *zT* as a function of Hall carrier concentration (n_H) for $(Bi_{0.25}Sb_{0.75})_2Te_3$ at 300 K. The experimental results (empty shapes in orange) and the literature data of Ref. 12 (empty diamond in grey), and prediction from the TB model were plotted.

Experimentally, the 17–20 % improvement in *zT* (1.05 at $n_H = 2.6\times10^{19}$ cm^{-3}) was achieved via carrier concentration tuning when compared to *zT* = 0.87 from Scherrer and Scherrer[12] (empty grey diamond in Fig. 3.5), and the *zT* of 0.9 (at 300 K) of Yim and Rosi[25] (not be shown in Fig. 3.5 as its n_H was not provided).

In summary, the best *zT* performance from $x = 0.75$ in $(Bi_{1-x}Sb_x)_2Te_3$ alloys is explained with two valence bands converging at $x = 0.75$. A two band transport model satisfactorily explains the experimental thermoelectric transport data for $(Bi_{1-x}Sb_x)_2Te_3$ alloys within a framework consistent with low temperature measurements and theory indicating a complex band structure. Based on the two-band model predicting higher *zT* for lower carrier concentrations, a $(Bi_{0.25}Sb_{0.75})_2Te_{3+\delta}$ oriented crystal was fabricated via zone levelling with excess Te. The successful suppression of holes from Sb_{Te} anti-site defects results in a *zT* of

1.05 at 300 K. This value is about 17 % higher than the commonly known best zT for $(Bi_{0.25}Sb_{0.75})_2Te$ crystals. Further improvements in zT are expected in fine-grained and nanostructured materials due to reduced lattice thermal conductivity.

Chapter 4

Phonon engineering through grain boundary dislocations in polycrystalline $(Bi_{0.25}Sb_{0.75})_2Te_3$

This section contains contents reproduced with permission from *Science* **348**, 109-114 (2015). DOI: 10.1126/science.aaa4166.

4.1 Introduction

Bismuth antimony telluride alloys are the most widely used thermoelectric bulk material developed in the 1960's for Peltier cooling with *p*-type composition close to $Bi_{0.5}Sb_{1.5}Te_3$ and peak zT of 1.1 near 300 K (ref. 12). The Bi-Sb atomic disorder in $Bi_{0.5}Sb_{1.5}Te_3$ scatters the heat carrying phonons, reducing κ_l that permits such high zT values. Matched with Bi_2Te_3 based *n*-type alloys, devices are commercially produced that provide a maximum temperature drop (ΔT_{max}) of 64 – 72 K with 300 K hot side (T_h) (ref. 11). Recent measured improvements in zT of $Bi_{0.5}Sb_{1.5}Te_3$ bulk alloys have been reported using strategies primarily based on nanometer-scale microstructures to add boundary scattering of phonons at the composite interface or grain boundaries[27,60-62]. However, improvements in the performance (ΔT_{max}) of Peltier cooling devices have not been realized since the development of bismuth antimony telluride[11].

Heat carrying phonons cover a broad spectrum of frequencies (ω) and the lattice thermal conductivity (κ_l) can be expressed as a sum of contributions from different frequencies[11,63]: $\kappa_l = \int \kappa_s(\omega) d\omega$. The spectral lattice thermal conductivity $\kappa_s(\omega)$ can be expressed as arising from the spectral heat capacity of phonons $C_p(\omega)$, their velocity $v(\omega)$, and their scattering time $\tau(\omega)$ such that $\kappa_s(\omega) = C_p(\omega) \times v^2(\omega) \times \tau(\omega)$. Phonons in all crystalline materials are scattered by other phonons by Umklapp scattering, which generally has a $\tau_U^{-1} \sim \omega^2$ dependence. Combining this with the Debye approximation for heat carrying phonons ($C_p(\omega) \sim \omega^2$)

gives $\kappa_s(\omega)$ = constant. This leaves a wide range of phonon frequencies where all frequencies contribute to the thermal conductivity (Fig. 4.1a).

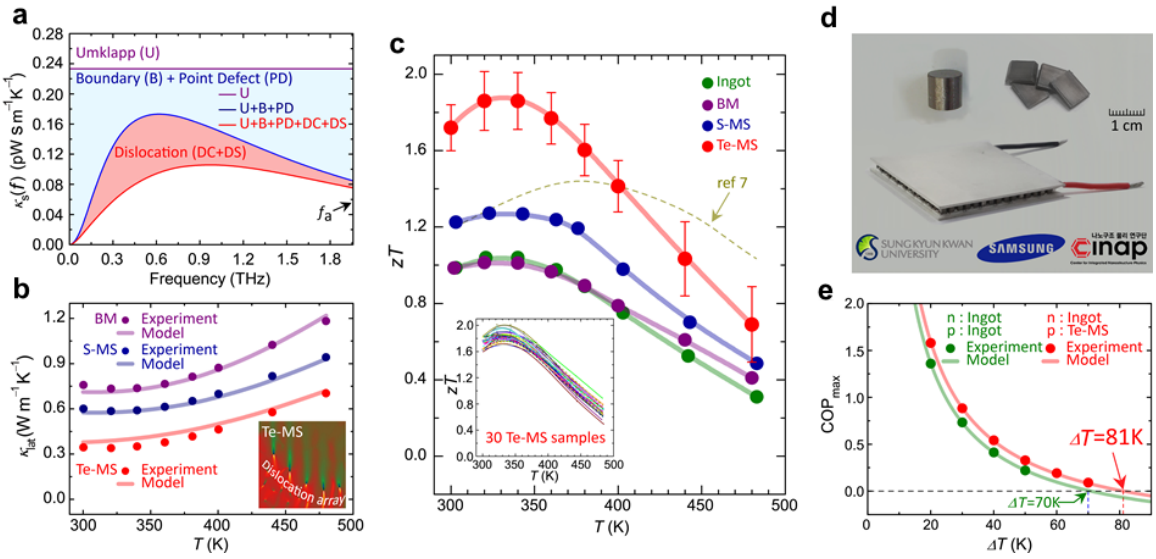

Fig. 4.1. Full-spectrum phonon scattering in high-performance bulk thermoelectrics. (a) The inclusion of dislocation scattering (DC + DS) is effective across the full frequency spectrum. Boundary (B) and point defect (PD) are effective only at low and high frequencies. The acoustic mode Debye frequency is f_a. (b) Lattice thermal conductivity (κ_l) for $Bi_{0.5}Sb_{1.5}Te_3$ alloys produced by melt-solidification (Ingot), solid-phase compaction (BM, S-MS) and liquid-phase compaction (Te-MS). The lowest κ_l of Te-MS can be explained by the mid-frequency phonon scattering due to dislocation arrays embedded in grain boundaries (inset). (c) The figure of merit (zT) as a function of temperature for $Bi_{0.5}Sb_{1.5}Te_3$ alloys. The data points (red) give the average (±standard deviations) of all 30 Te-MS samples (inset), which shows excellent reproducibility. (d) A Peltier cooling module (right) with 127 couples made from *p*-type $Bi_{0.5}Sb_{1.5}Te_3$ Te-MS pellet (left) and *n*-type 1 wt. % SbI_3 doped $Bi_2Te_{2.7}Se_{0.3}$ ingot. (e) The maximum coefficient of performance (COP_{max}) measured on modules of (d) where the high-performance is confirmed with notably high ΔT_{max} of 81 K with 300 K hot side.

The κ_l can be further reduced with additional scattering mechanisms. Traditional mechanisms are only effective at the high or low frequency ends[11]. Point defect scattering of phonons from the Bi-Sb disorder in $Bi_{0.5}Sb_{1.5}Te_3$ targets high frequency phonons with a scattering time depending on frequency as $\tau_{PD}^{-1} \sim \omega^4$ (ref. 11), similar to Rayleigh scattering. However, boundary scattering of phonons targets low frequency phonon as it is frequency independent[64] ($\tau_B^{-1} \sim$ constant). Even the scattering of nanometer-sized particles can be well described with these two models as the small size Rayleigh regime rapidly crosses over to the boundary regime as the particle size increases[65]. A full-spectrum strategy targeting the wide spectrum of phonons including mid-frequency phonon scattering is necessary for further reduction in κ_l. However, at the same time the high carrier mobility (μ) must be maintained because the maximum zT of a material is

determined by the ratio μ/κ_l (quality factor)[11]. Thus, any reduction in κ_l by phonon scattering must not be compensated by a similar reduction in μ due to electron scattering for there to be a net benefit[18].

4.2 Liquid-phase compacting process

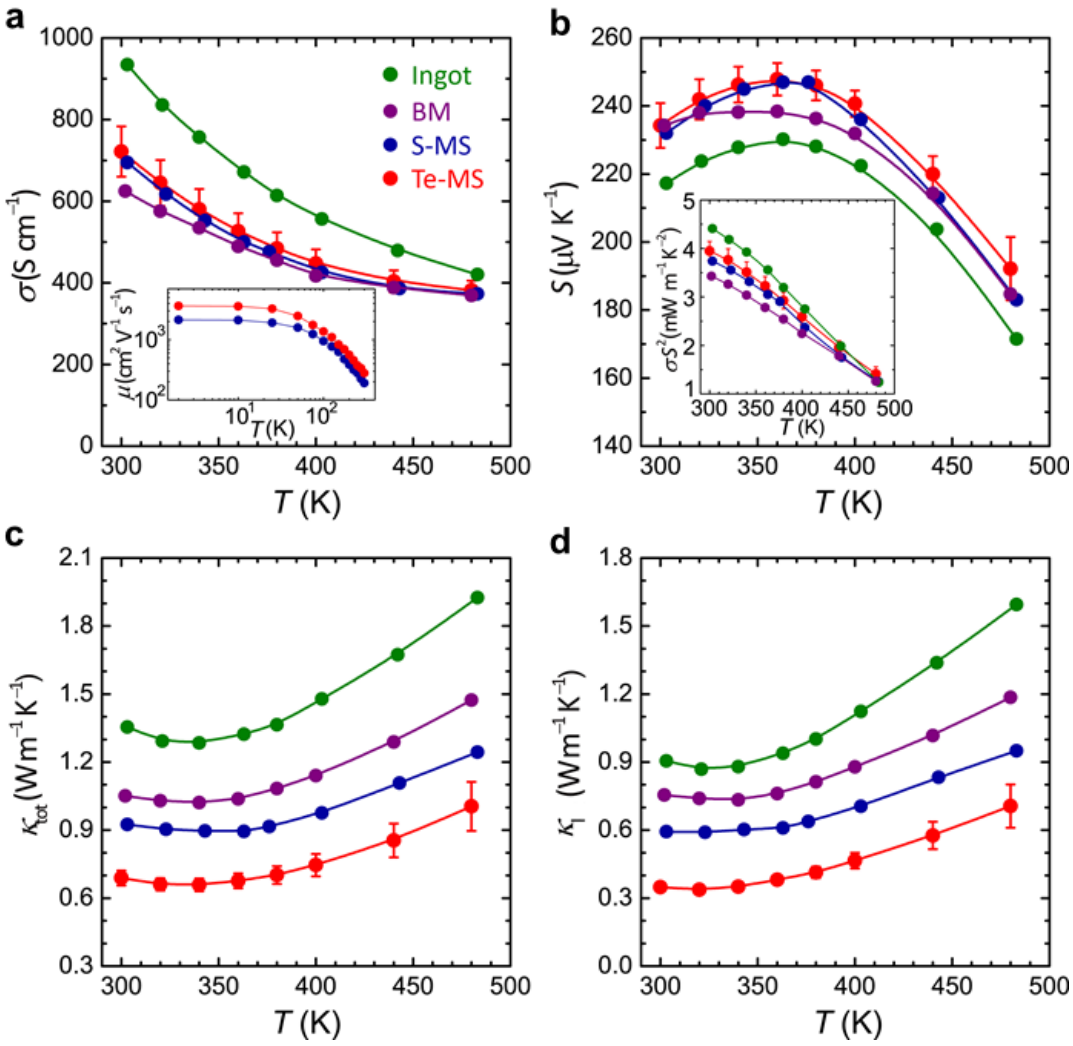

Fig. 4.2. Comparison of thermoelectric properties of $Bi_{0.5}Sb_{1.5}Te_3$ between different fabrication methods. Introduction of dislocation arrays has a large effect on thermal conductivity but a small effect on electronic conductivity. (a) Temperature dependence of electrical conductivity (σ). Charge carrier mobilities of S-MS (190 $cm^2\ V^{-1}\ s^{-1}$) are lower than for Te-MS (280 $cm^2\ V^{-1}\ s^{-1}$) materials (Inset). (b) Temperature dependence of Seebeck coefficient (S) and power factor (σS^2) (Inset). Temperature dependences of total (c) and lattice (d) thermal conductivity (κ_{total}, κ_l) for all samples. The error bars of Te-MS in all panels are the standard deviations from the measurements of 30 samples.

Liquid-phase sintering produces low energy, semi-coherent grain boundaries that one can expect to have a minimal impact on electron scattering. The techniques to engineer and characterize grain boundaries have

been well established in materials science due to their importance in engineering the mechanical strength[66], magnetism[67], and other material properties[68]. Most importantly, the periodic dislocations that can arise from such low energy grain boundaries add a new mechanism that targets the mid-frequency phonons with both $\tau^{-1} \sim \omega$ and $\tau^{-1} \sim \omega^3$ dependence that is between those for point defect and boundary scattering[11,63]. In order to produce the periodic dislocations at low energy grain boundaries in $Bi_{0.5}Sb_{1.5}Te_3$ alloys, we applied a simple liquid-phase compacting process. The process differed from typical liquid-phase sintering as it included applied pressure and transient flow of the liquid phase during compaction. The process greatly reduced κ_l to 0.33 W m^{-1} K^{-1} at 320 K (Fig. 4.1b, Fig. 4.2d) and resulted in an exceptionally high zT of 1.86 ± 0.15 at 320 K for dozens of independently measured $Bi_{0.5}Sb_{1.5}Te_3$ samples (Fig. 4.1c) used to make a Peltier cooling module with 127 couples (Fig. 4.1d). The module outperforms all known single stage Peltier cooling modules[11,69], demonstrating a ΔT_{max} of 81 K with T_h of 300 K (Fig. 4.1e). We compare ingot, ball milled (BM), and stoichiometric melt spun (S-MS) $Bi_{0.5}Sb_{1.5}Te_3$ materials (Figs. 4.1 and 4.2). The latter two types of samples were fabricated by using spark plasma sintering (SPS). Two different melt-spun materials were synthesized, stoichiometric (S-MS), and with excess Te (Te-MS, Fig. 4.3a, red arrow).

Melt-spun samples have plate-like microstructure of S-MS and Te-MS ribbons with platelets several micrometers wide and several hundred nanometers thick (Fig. 4.3b). The Te excess composition has an eutectic microstructure over the entire ribbons that forms between the $Bi_{0.5}Sb_{1.5}Te_3$ platelets (Fig. 4.3b). The eutectic phase consists mostly of elemental Te and a small amount of $Bi_{0.5}Sb_{1.5}Te_3$ nano-particles. During the high temperature (480 ^{o}C) and pressure (70 MPa) process of SPS, above the melting point of Te (450 ^{o}C), the excess Te in the eutectic phase was liquidified and expelled to the outer surface of the graphite die (Fig. 4.3c and Fig. 2.5).

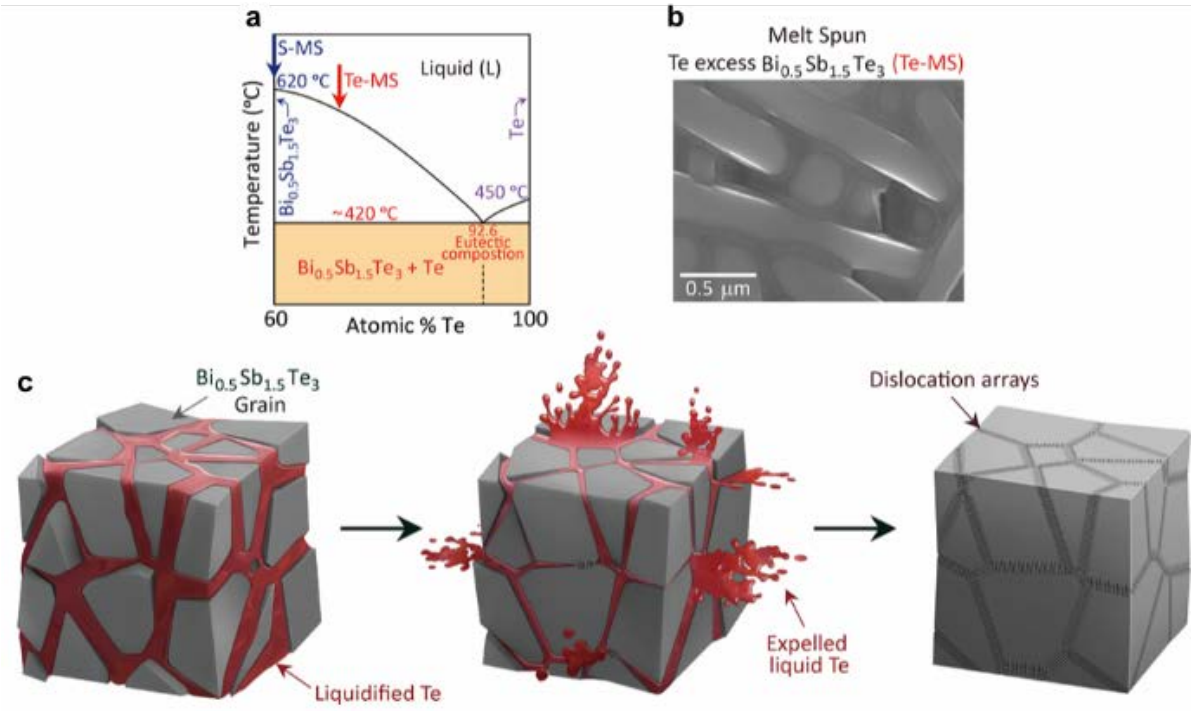

Fig. 4.3. Generation of dislocation arrays at grain boundaries in $Bi_{0.5}Sb_{1.5}Te_3$. (a), Phase diagram of $Bi_{0.5}Sb_{1.5}Te_3$–Te system showing an eutectic composition at 92.6 at. % Te. Blue and red arrows indicate the nominal composition of melt spun stoichiometric $Bi_{0.5}Sb_{1.5}Te_3$ (S-MS) and 25 wt. % Te excess $Bi_{0.5}Sb_{1.5}Te_3$ (Te-MS) material. (b) The scanning electron microscope (SEM) image of melt spun ribbon of Te-MS material showing the $Bi_{0.5}Sb_{1.5}Te_3$ platelets surrounded by the eutectic phase of $Bi_{0.5}Sb_{1.5}Te_3$–Te mixture, in which the $Bi_{0.5}Sb_{1.5}Te_3$ particles (white spots) have the size of 10–20 nm. (c) Schematic illustration showing the generation of dislocation arrays during the liquid-phase compaction process. The Te liquid (red) between the $Bi_{0.5}Sb_{1.5}Te_3$ grains flows out during the compacting process and facilitates the formation of dislocation arrays embedded in low energy grain boundaries.

4.3 Periodic arrays of dislocations at grain boundaries

The morphology of the grain boundary structure in the Te-MS material is remarkably different than the typical grain boundaries as found in the S-MS material. TEM images (Figs. 4.4b to 4.4j) reveals a Moiré pattern (up to 50 nm wide) at the grain boundaries between the $Bi_{0.5}Sb_{1.5}Te_3$ grains in the Te-MS material (Fig. 4.4b), compared to the few nanometer width as observed in the S-MS material (Fig. 4.4a). Moiré patterns can be observed when the grain boundary plane is oblique to the TEM zone axis so the two crystals overlap along the viewing direction. The Moiré patterns indicate the grains are highly crystalline with clean grain boundaries in which the obscured dislocations exist. From the elemental mapping (TEM-EDS) in the Te-MS material, we confirmed no presence of excess Te at the grain boundaries, suggesting that the abnormal contrast is not due to a secondary phase.

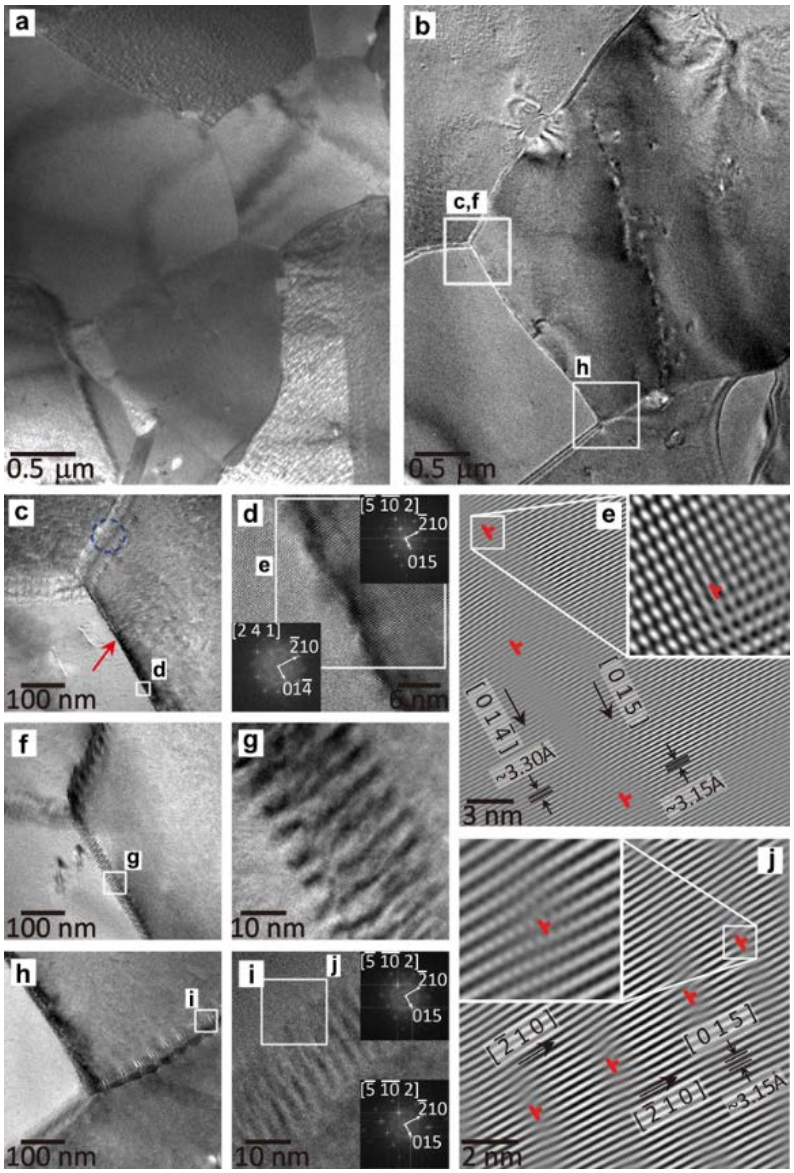

Fig. 4.4. Dislocation arrays embedded in grain boundaries. (a) Low magnification TEM image of S-MS material. (b) Low magnification TEM image of a Te-MS material. (c) Enlarged view of boxed region in (b). The grain boundary indicated by red arrow is aligned along the zone axis showing only strain effects while the two grain boundaries at upper part show Moiré patterns. The high magnification TEM image of circled area is shown in fig. S15. (d) Enlarged view of boxed region in (c). The insets are FFT images of adjacent grains crossing a twist-type grain boundary (GB). (e) IFFT image of (0 1 5) and (0 1 $\bar{4}$) atomic planes of left and right grains in the inset (d). Along the boundary, edge dislocations, indicated as red symbols, are clearly shown. Burgers vectors of each dislocation is $\mathbf{B_D}$ = <0 1 5>, parallel to the boundary. The misfit between the two planes are ~ 0.15 Å (~ 4.5 %), which compensates the misfit spacing of ~ 6 nm and is identical to the periodic patterns (~ 6 nm spacing) in (f) and (g). (f) Enlarged view of boxed region in (b). A view of tilted zone axis from (c), showing periodic Moiré patterns along GBs. (g) Enlarged views of boxed region in (f). (h) Enlarged view of boxed region in (b). (i) Enlarged view of boxed region in (h). The insets are FFT images of adjacent grains crossing a tilt-type GB. (j) FFT image of (0 1 5) atomic planes in the inset of (I). Burgers vectors of the each dislocation is $\mathbf{B_D}$ = <$\bar{2}$ 1 0>, perpendicular to the boundary. The misfit spacing of ~ 2.5 nm was obtained. Insets of (e) and (j) are the IFFT images of boxed areas, respectively, clearly identifying the dislocations.

The clean grain boundary structure observed in Te-MS material requires the presence of periodic arrays of dislocations that form at low energy grain boundaries. Figure 4.4c shows a grain boundary (indicated by red arrow) aligned along the zone axis showing only strain effects. The indexing of fast Fourier-transformed (FFT) images confirmed the coincidence of (0 1 $\bar{4}$) and (0 1 5) atomic planes along the two adjacent grains at the twist-type grain boundary with lattice spacing of 3.30 and 3.15 Å, respectively. Edge dislocation arrays are found in inverse FFT (IFFT) images of Fig. 4.4d (Fig. 4.4e, red symbols). The dislocations compensate for the *d*-spacing mismatch between the crystallographic planes of adjacent grains, which is ~ 0.15 Å (4.5 %) between (0 1 5) and (0 1 $\bar{4}$) atomic planes, introducing misfit spacing of ~ 6 nm. This mismatch is identical, as expected[70], to the periodicity in the translational Moiré patterns of the grain boundary observed in Figs. 4.4f and 4.4g, which were taken by slightly tilting the zone axis from that of Figs. 4.4c and 4.4d. Dislocation arrays with the periodic spacing of ~ 2 nm were observed together with Moiré fringes at the circled area (in blue) of upper grain boundary in Fig. 4.4c. Another array of dislocations was observed in tilt-type boundary in Fig. 4.4h. The FFT images in the inset of Fig. 4.4i revealed the 5° misorientation between two adjacent grains and inverse IFFT image of (0 1 5) atomic planes in Fig. 4.4j and dislocation arrays with the misfit spacing of ~ 2.5 nm. Such dislocation arrays are expected to be present in low angle grain boundaries or between grains with small *d*-spacing mismatch to lower the interfacial energy[71]. The dislocation arrays observed here have a close spacing between cores of ~2.5 – 6 nm, which considering the size of the grains corresponds to an areal dislocation density of ~2×10^{11} cm^{-2} that is 100 times higher than that observed in grains of Bi_2Te_3 (ref. 72).

In a typical solid-phase sintering, the grain boundaries have random alignment due to a limited diffusion length of atoms/dislocations, and so the chance of low angle boundary (< 11°) is very low[71]. In contrast, in liquid-phase sintering, the wetting liquid penetrates into the grain boundaries[73]. Atoms in a liquid have much higher diffusivities and also dislocations at the grain boundaries have much higher diffusion lengths[74]. The high solubility of Bi and Sb in the Te liquid and insignificant solubility of Te in the solid phase contributes to the very rapid mass transport (over 100 times faster than in solids) and rapid rearrangement

of the grains[73]. In addition, the capillary force of the liquid at the grain boundary exerts a force facilitating grain rearrangement[73,75].

However, the liquid-phase becomes absorbed in the matrix of the grain in a typical transient liquid phase sintering, leading to compositional variation of the matrix. This prohibits the application of traditional liquid-phase sintering for thermoelectric Bi-Sb-Te because compositional variation will degrade the TE properties. In contrast, the liquidified excess Te in the eutectic phase is expelled during the high pressure-assisted liquid-phase compacting processing. Any slight amount of Te remaining is nearly insoluble in $Bi_{0.5}Sb_{1.5}Te_3$ and does not as dramatically affect the carrier concentration. Furthermore, the applied pressure induces additional stresses which helps create dislocations[75] and accelerate grain rearrangement[73]. As a result, the grain interfaces rearrange to allow low energy grain boundaries, which results in dislocation arrays within much of the grain boundary.

From the thermal and electrical transport properties it appears that the semi-coherent grain boundaries of Te-MS material do maintain high charge carrier mobility but provide sufficient atomic strain to scatter heat carrying phonons. The small increase in Seebeck coefficient is due to a slight decrease in carrier concentration for S-MS and Te-MS materials compared to the Ingot material (Fig. 4.2b). The reduced grain size of the S-MS and Te-MS materials leads to lower carrier mobility. This decrease is less dramatic for Te-MS indicating the semi-coherent grain boundaries in Te-MS are less disruptive to charge carriers than those in the S-MS material (Fig. 4.2a). Low energy grain boundaries in Bi-Sb-Te are likely formed when atomic displacements are primarily in the Te-Te van der Waals layer, which have been observed experimentally[76]. Displacements in this layer are also likely to be least disruptive to the charge carriers and maintain high mobility.

While the dense dislocation arrays embedded in grain boundaries do little to scatter charge carriers, they are remarkably efficient at scattering phonons and greatly reducing thermal conductivity in the Te-MS material (Fig. 4.2d). The κ_l values were extracted from κ_{total} by subtracting the electronic thermal

conductivity (κ_e), which was estimated using the Wiedemann-Franz relation. We calculated the Lorenz number (L_0) using the reduced Fermi energy obtained from measured S values at different temperatures. The calculations indicate that dislocation arrays embedded in grain boundaries cause the reduction of κ_l. The κ_l value at 320 K (0.33 W m^{-1} K^{-1}) of the Te-MS sample is comparable to the reported value (0.29 W m^{-1} K^{-1}) in highly deformed $Bi_{0.2}Sb_{1.8}Te_3$ with high-density lattice defects[77], indicating that dense dislocation arrays at grain boundaries are effective to reduce the κ_l.

4.4 Reinforced phonon scattering from dislocation strain field

We have modeled the temperature dependent κ_l of BM, S-MS and Te-MS materials based on Debye-Callaway model[78] using parameters derived from independently measured physical properties (Fig. 4.1b). The total phonon relaxation time (τ_{total}) was estimated by including scattering from Umklapp processes (τ_U) and point defects (τ_{PD}) using parameters based on bulk alloys[63,79,80]. We used microscopy to determine the parameter of average grain size (d) for the grain boundary scattering[70] (τ_B). The calculated κ_l (0.66 W m^{-1} K^{-1} at 300 K) for BM matches the measured data well, verifying the values used for Umklapp processes (τ_U) and point defects (τ_{PD}) of $Bi_{0.5}Sb_{1.5}Te_3$ alloys. The 18 % reduction in κ_l observed in S-MS material relative to BM material at 300 K is explained by a grain size reduction from 50 μm to 300 nm. The additional 29 % reduction in κ_l for Te-MS material is explained by introducing phonon relaxation times associated with additional scattering from dislocation cores (τ_{DC}) and strain[81-83] (τ_{DS}), using the experimentally determined dislocation density (~2×10^{11} cm^{-2}) and the effective Burgers vector (B_D of ~12.7 Å).

This analysis shows that the periodic spacing of dislocation arrays plays a vital role for reducing κ_l. When the spacing between dislocation cores is small as observed in Te-MS material, the scattering from dislocation strain is reinforced[84]. This effect was experimentally observed in Ag-Cd alloys with the large scattering effect as due to the dislocation pile-up[64]. When dislocations are closely spaced the effective Burgers vector (B_D) is the sum of the individual Burgers vectors involved[85]. As the scattering rate is

proportional to B_D^2, this pile-up of dislocation strain leads to a non-linear increase in scattering. The exact amount of reinforcement is not precisely specified in the theory and leads to the only adjustable parameter in the model. Nevertheless, the Burgers vector that precisely fits the data is well within the range observed experimentally[76] (more details regarding the κ_l modelling can be found in Chapter 5).

The dislocation scattering mechanism is particularly effective because it targets phonons not scattered sufficiently by the other mechanisms providing a full-spectrum solution to scatter phonons. Compared to Umklapp scattering (Fig. 4.1a), boundary scattering from grain boundaries ($\tau_B^{-1} \sim \omega^0$) is efficient at scattering low frequency phonons but quickly become ineffective at higher frequencies. Conversely, point defects scatter mostly high frequency phonons ($\tau_{PD}^{-1} \sim \omega^4$). However, most of the remaining heat carrying phonons have intermediate frequency around 0.63 THz (Fig. 4.1a) and avoid scattering from boundaries and point defects. The 0.63 THz phonons still carry 74% of the heat they would have carried without any scattering from boundaries or point defects in the S-MS material. Including the dislocation scattering as found in the Te-MS material, the κ_s of 0.63 THz phonons drops to less than 45% of the heat they would have carried with only Umklapp scattering (Fig. 4.1a).

The low thermal conductivity while maintaining high mobility results in a dimensionless figure of merit (zT) for Te-MS that reaches a maximum value of 2.01 at 320 K within the range of 1.86 ± 0.15 at 320 K for 30 samples (Fig. 4.1c), a much higher value than for S-MS or Ingot materials. Most importantly, for cooling applications, the zT at 300 K is high (1.72 ± 0.12), suggesting it should provide superior refrigeration than other materials. For example, the zT is the higher than that of nanograined $Bi_{0.5}Sb_{1.5}Te_3$ alloy (dotted line in Fig. 4.1c) near room temperature. These results from the ability of dislocation arrays to enable a full-spectrum scattering of phonons due to a compounding effect not found in randomly dispersed dislocations inside grains. The present liquid-phase compaction method assisted with a transient liquid flow is highly scalable for commercial use and generally applicable to other thermoelectric systems such as PbTe, $CoSb_3$, Si-Ge alloys, and even engineer thermal properties of other thermal materials such as

thermal barrier coatings[86]. This may accelerate practical applications of thermoelectric systems in refrigeration and beyond to waste heat recovery and power generation.

4.5 ΔT_{max} calculation of the Peltier cooler with the *p*-type Te-MS

The ultimate verification of the exceptional *zT* comes from testing the performance of a Peltier cooler (Fig. 4.1d) made using Te-MS materials. A state-of-the-art Peltier device using the Te-MS as the *p*-type material and an *n*-type ingot material was made with cutting edge commercial methods. The device not only greatly outperforms a similar device made with the *p*- and *n*-type ingot materials (Fig. 4.1e), but also outperforms all commercial Peltier devices[69]. We determined the coefficient of performance (COP = cooling power/input power) to assess the cooling performance of both Peltier devices. Maximum values for coefficient of performance (COP_{max}) were taken at different ΔT in COP versus input current. The values of COP_{max} for two modules were plotted as filled circles in Fig. 4.1e. By assuming asymmetric thermal contact resistivity of the modules, following equation was derived from Gao Min's equation[87,88] for a module with symmetric thermal contacts.

$$COP_{max} = \left(\frac{1}{1+\frac{rl_c}{l}}\right)\left[\frac{T_c}{T_h - T_c}\frac{\left(1+Z\frac{T_h+T_c}{2}\right)^{1/2} - \frac{T_h}{T_c}}{\left(1+Z\frac{T_h+T_c}{2}\right)^{1/2}+1}\right], \qquad \text{(Eqn. 4.1)}$$

where l_c and l are the length as shown in Fig. 4.5 and r corresponds to thermal conductivity of thermoelements divided by that of the contact layers (substrate + contact + metal bonding in Fig. 1.3). Variables r and Z were adjusted to fit calculated COP_{max} (lines in Fig. 4.1e) to experimental COP_{max} (filled circles in Fig. 4.1e) data. The ΔT_{max} values are easily extracted from the COP measurements as the temperature difference reached when the cooling power vanishes.

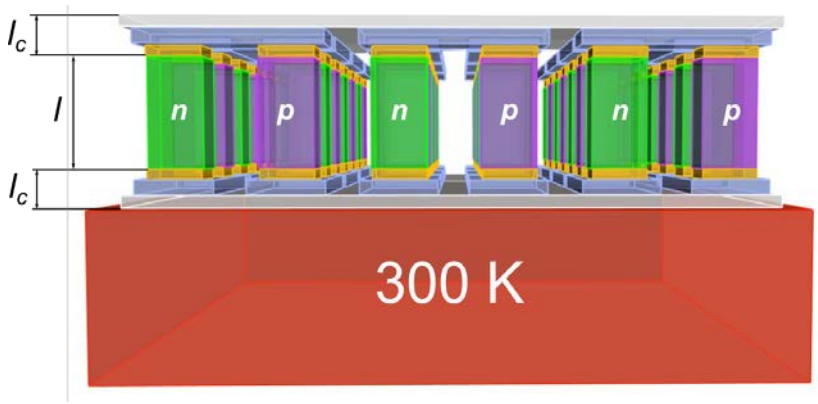

Fig. 4.5. Schematic setup for ΔT_{max} measurement in a thermoelectric module.

A key characteristic performance metric of a Peltier cooler is ΔT_{max}, which is directly related to the zT of materials. While the ΔT_{max} of Peltier cooler made from the ingot materials falls within the range of current commercial devices, 64 K < ΔT_{max} < 72 K for T_h of 300 K, the Peltier cooler made with the Te-MS *p*-type material exhibits an ΔT_{max} of 81 K for T_h of 300 K (Fig. 4.1e).

Chapter 5

Phonon scattering by grain boundary dislocations at low temperature

This section contains contents that have been submitted to a journal. Once it is accepted, permission will be asked.

5.1 Introduction

Significant improvements in thermoelectric materials have been achieved by suppressing heat conduction via phonons. Other than κ_l, all the materials variables in zT are highly coupled to one another making the optimization of zT a nontrivial task. Therefore, much effort has been devoted to reduce κ_l in order to improve zT.

Phonons scatter off any irregularities in the lattice. For example, alloy atoms[89,90], rattling atoms[91,92], and other point defects[93] can reduce the phonon mean free path. If the unit cell contains a large number of atoms[94], phonon heat conduction is also impeded because of a large fraction of heat carrying optical phonons with low group velocities[63]. The frequency dependence of the point-defect scattering (${\tau_{PD}}^{-1} \sim \omega^4$, where τ^{-1} and ω are the phonon relaxation rate and the phonon frequency, respectively) and Umklapp scattering (${\tau_U}^{-1} \sim \omega^2$) makes both scattering mechanisms effective at high phonon frequencies.

Phonons at low frequencies can be targeted by frequency-independent boundary scattering (${\tau_B}^{-1} \sim \omega^0$). The majority of efforts to decrease the grain size in nanostructured materials aim to maximize scattering of phonons at an increased density of boundaries[27] (for low κ_l superlattices, many efforts were focused on phonon localization[95]). However, when the composition of nanostructures embedded in a matrix differs from that of the matrix the boundary scattering alone cannot describe the intensity of scattering at the interfaces accurately[81,96]. He *et al*.[81] observed misfit dislocations at the interfaces of spinodally decomposed

PbTe and PbS (nanoscale in size). In addition to the boundary scattering, He *et al*. included scattering from dislocations to predict the phonon scattering at interfaces/boundaries. However, amid many other scattering mechanisms considered, the importance of dislocation scattering in reducing κ_l was not fully stressed.

Recently, Kim *et al*.[1], developed a pathway to encircle grains of polycrystalline $Bi_{0.5}Sb_{1.5}Te_3$ with dense dislocation arrays to achieve a substantial κ_l reduction (zT = 1.86 at 320 K). In contrast to the previous misfit dislocations at interfaces of a two-phase material[81], the dislocation arrays were formed along grain boundaries of single phase $Bi_{0.5}Sb_{1.5}Te_3$. Kim *et al*. demonstrated that the grain boundary dislocation scattering was responsible for the dramatic reduction in κ_l. Nonetheless, the effect of dislocation scattering mechanism at low temperature was not studied.

In this work, we present the low temperature experimental κ_l of the sample whose maximum zT is 1.86 (at 320 K). Here we show that grain boundary dislocation scattering mechanism is required to model the κ_l satisfactorily at low temperatures where boundary and dislocation scatterings are dominant. Both models used separately to calculate the κ_l at high temperatures (T > 300 K) and at low temperatures (T < 200 K) are thoroughly discussed and compared.

5.2 Lattice thermal conductivity model for T > 300 K

The κ_l can be calculated from the heat capacity of phonons (C), phonon velocity (v), total relaxation time (τ_{total}), and the phonon frequency (ω) as shown in Eqn. 5.1.

$$\kappa_l = \frac{1}{3}\int C(\omega)\, v^2(\omega)\, \tau_{total}(\omega)\, d\omega. \qquad \text{(Eqn. 5.1)}$$

Assuming that the phonon group velocity is constant (Debye model) and that scattering mechanisms are independent of each other, Callaway's equation for the κ_l can be approximated to

$$\kappa_l = \frac{k_B}{2\pi^2 v}\left(\frac{k_B T}{\hbar}\right)^3 \int_0^{\theta_a/T} \frac{\tau_{total}(z)\, z^4 e^z}{(e^z-1)^2} dz, \qquad \text{(Eqn. 5.2)}$$

where k_B, $\hbar$, θ_a, and z are the Boltzmann constant, reduced Planck's constant, acoustic Debye temperature, and $\hbar\omega/k_{\mathrm{B}}T$, respectively[97]. When the τ_{total} is obtained from individual relaxation times (τ_i) for different scattering mechanisms according to $\tau_{total}(z)^{-1} = \sum_i \tau_i(z)^{-1}$ the calculation of κ_l using Eqn. 5.2 is straightforward. Therefore, a careful characterization of each τ_i is essential to model κ_l with high predictive power.

Recently, a drastic κ_l reduction led to dramatic zT improvement in $Bi_{0.5}Sb_{1.5}Te_3$[(1)]. The κ_l of the polycrystalline samples (named as BM, S-MS, and Te-MS) produced using three different methods were computed consecutively to single out a cause for the reduction in thermal conductivity (Fig. 5.1). The BM sample was fabricated by ball-milling (hence the name BM) $Bi_{0.5}Sb_{1.5}Te_3$ ingots followed by Spark Plasma Sintering (SPS) the ball-milled powder. The S-MS and Te-MS samples were also sintered via SPS at the end. However, powders used in SPS for the S-MS and Te-MS were melt-spun from $Bi_{0.5}Sb_{1.5}Te_3$ ingots (S-MS, which stands for stoichiometric-MS) and from those with 25 wt. % Tellurium excess (Te-MS), respectively.

First, in order to calculate κ_l of the BM sample with 20 μm average grain size, relaxation times associated with Umklapp scattering (τ_U), point-defect scattering (τ_{PD})[18], and boundary scattering (τ_B) were considered as relevant scattering mechanisms (Table 5.2). Although the τ_B given by[63]

$$\tau_B{}^{-1} = \frac{v}{\alpha_t d}, \qquad \text{(Eqn. 5.3)}$$

where d and α_t are the experimentally determined grain size and the grain boundary transmission coefficient, respectively, has no free parameter (α_t = 1 was used for T > 300 K), the τ_U and the τ_{PD} include variables, which need to be adjusted to the measured κ_l. The Umklapp scattering is a phonon-phonon scattering in which the total crystal momentum is not conserved. Its relaxation time, τ_U, is of the form[63]

$$\tau_U{}^{-1} = A_{\mathrm{N}} \frac{2}{(6\pi^2)^{1/3}} \frac{k_{\mathrm{B}} V^{1/3} \gamma^2 \omega^2 T}{M v^3}, \qquad \text{(Eqn. 5.4)}$$

where V, γ, M, and A_N are the atomic volume, Grüneisen parameter, average atomic mass, and the free parameter, which takes momentum-conserving Normal scattering into account[98]. Point-defect scattering originates from alloy atoms scattering phonons, which is expressed as[82]

$$\tau_{PD}{}^{-1} = \frac{V\omega^4}{4\pi v^3}\Gamma\,, \qquad \text{(Eqn. 5.5)}$$

where Γ is the scattering parameter. In Eqn. 5.5, another free parameter (G) is hidden inside of the Γ[(18)],

$$\Gamma = x(1-x)\left[\left(\frac{\Delta M}{M}\right)^2 + \frac{2}{9}\left\{(G+6.4\gamma)\frac{1+r}{1-r}\right\}^2\left(\frac{\Delta a}{a}\right)^2\right], \qquad \text{(Eqn. 5.6)}$$

where x, ΔM, G, r, and Δa are the fractional concentraition of either of constituents, difference in mass, parameter representing a ratio of fractional change of bulk modulus to that of local bond length, Poisson ratio, and the difference in lattice constant, respectively. The A_N and G in Eqn. 5.4 and 5.6, respectively were fit to experimental κ_l varying with x in $(Bi_{1-x}Sb_x)_2Te_3$ alloy[99] by Stordeur and Sobotta to model κ_l of BM sample in Fig. 5.1 (purple solid line). The use of reliable experimental literature data by independent scientists, which give values that are consistent with other studies and expected for this material, demonstrates the reasonableness of the model. Including parameters that were fitted, other material-dependent or experimentally determined parameters used to calculate theoretical κ_l of the BM, S-MS, and Te-MS samples at high temperature (as shown in Fig. 5.1) are listed in Table 5.1. All the parameters in Table 5.1 except A_N, $B_{D,eff}$, N_D, and α_t were also used in low temperature κ_l modeling in Fig. 5.2.

Table 5.1. Parameters used to model κ_l of BM, S-MS and Te-MS samples in Fig. 5.1 (at high temperature from ref. 1) and in Fig. 5.2 (at low temperature except A_N, $B_{D,eff}$, N_D, and α_t).

Parameters	Description	Values	Ref.
θ_a	acoustic Debye temp.	94 K	[100]
v	avg. phonon velocity	2147 m/s	[101]
v_L	longitudinal velocity	2884 m/s	[101]
v_T	transverse velocity	1780 m/s	[101]
M	atomic mass of BST†	2.22×10^{-25} kg	–
V	atomic vol. of BST†	31.26 Å^3	[63]
$M_{Bi_2Te_3}$	atomic mass of Bi_2Te_3	2.79×10^{-25} kg	–
$M_{Sb_2Te_3}$	atomic mass of Sb_2Te_3	2.07×10^{-25} kg	–
$V_{Bi_2Te_3}$‡	atomic vol. of Bi_2Te_3	3.40×10^{-29} m^3	–
$V_{Sb_2Te_3}$‡	atomic vol. of Sb_2Te_3	3.13×10^{-29} m^3	–
A_N	parameter in Eqn. 5.4	2.6	fit
G	parameter in Eqn. 5.6	23.8	fit
γ	Grüneisen parameter	2.3	[102]
r	Poisson's ratio	0.24	[103]
N_D	dislocation density	2×10^{11} cm^{-2}	exp.
$B_{D,eff}$	effective Burgers vector	12.7 Å	fit
d_{BM}	BM grain size	20 μm	exp.
d_{MS}	S-MS, Te-MS grain size	300 nm	exp.
α_t	transmission coefficient	1	–
c_0	conc. of Bi_2Te_3	0.25	–
K	bulk modulus of Sb_2Te_3	44.8 GPa	[102]
T_a	annealing temp.	753 K	exp.

† BST = $Bi_{0.5}Sb_{1.5}Te_3$

‡ Lattice constant (a) was obtained by taking cube root of the atomic volume

Since, the only difference between the BM sample and the melt-spun $Bi_{0.5}Sb_{1.5}Te_3$ sample with 300 nm grain size (S-MS) was the size of the grain (20 μm in BM), κ_l of the S-MS was calculated by simply changing the τ_B (to d = 300 nm) in the τ_{total} of the BM sample (Table 5.2) while keeping τ_U and τ_{PD} the same as for BM. A good fit between the theory (blue solid line) and the experimental data (empty blue circle) was achieved for the S-MS sample (Fig. 5.1).

Lastly, in order to compute κ_l of melt-spun $Bi_{0.5}Sb_{1.5}Te_3$ sample with 25 wt. % Te excess (Te-MS), scattering relaxation times from dislocation cores (τ_{DC}) and dislocation strain field (τ_{DS}) were introduced to τ_{total} of S-MS (Table 5.2). Because the excess Te flowed out of the Te-MS sample during SPS (keeping its composition the same as the S-MS), and the grain size of the Te-MS was similar to that of S-MS, we could use the same τ_U, τ_{PD}, and τ_B in τ_{total} of the S-MS for that of the Te-MS. However, unlike S-MS, Moiré fringes indicative of dense dislocation arrays were observed in grain boundaries of the Te-MS sample. As arrays

of dislocations at grain boundaries can be equally treated as a sum of isolated dislocations inside a grain[104], the following equations can be used to describe grain boundary dislocation scattering in Te-MS:

$$\tau_{DC}^{-1} = N_D \frac{V^{4/3}}{v^2}\omega^3, \qquad \text{(Eqn. 5.7)}$$

$$\tau_{DS}^{-1} = 0.6 \times B_{\mathrm{D,eff}}^2 N_D(\gamma+\gamma_1)^2\omega\left[\frac{1}{2}+\frac{1}{24}\left(\frac{1-2r}{1-r}\right)^2\left\{1+\sqrt{2}\left(\frac{v_L}{v_T}\right)^2\right\}^2\right], \qquad \text{(Eqn. 5.8)}$$

where $B_{\mathrm{D,eff}}$, N_D, γ_1, v_L, and v_T are the magnitude of effective Burgers vector, dislocation density, change in Grüneisen parameter, longitudinal phonon velocity, and the transverse phonon velocity, respectively. While determining τ_{DC} is straightforward (N_D was computed with measured spacing between dislocation cores), an explanation is required on the details of the τ_{DS} equation before using it. First of all, the numerical prefactor 0.6 in τ_{DS} (Eqn. 5.8) is a product of the most recent constant of proportionality (1.1) Klemens placed in the τ_{DS} formula (Klemens has modified the number multiple times[64,105,106]) and another factor of 0.55 to account for arrays of dislocation oriented in random directions[106]. A factor of 18 was multiplied by Klemens[105] to the first constant of proportionality (0.06) he theoretically calculated to minimize the discrepancy between the theory and experiments.

Further phonon scattering from inhomogeneously distributed solute atoms in alloys near grain boundary dislocations (due to the strain field) was accounted by a change of the Grüneisen parameter, γ_1[(107)], in Eqn. 5.8. Even though the solute atoms were treated as point defects to theoretically quantify γ_1, this scattering was different from the point defect scattering (Eqn. 5.5) in that it only described the combined scattering from modulation of the point defect concentration[108], not the scattering from individual point defects as in Eqn. 5.5. The γ_1 changes the intensity of scattering from the dislocation strain field. Eqns. 5.9 and 5.10 can be utilized to determine γ_1

$$\gamma_1 = \frac{V_{\mathrm{Sb_2Te_3}} c_0 K}{k_{\mathrm{B}} T_{\mathrm{a}}}(\gamma\alpha^2-\alpha\beta), \qquad \text{(Eqn. 5.9)}$$

$$\alpha = \frac{\left(V_{\mathrm{Bi_2Te_3}} - V_{\mathrm{Sb_2Te_3}}\right)}{V_{\mathrm{Sb_2Te_3}}} \qquad \beta = \frac{1}{2}\frac{\left(M_{\mathrm{Sb_2Te_3}} - M_{\mathrm{Bi_2Te_3}}\right)}{M_{\mathrm{Sb_2Te_3}}}\ , \qquad \text{(Eqn. 5.10)}$$

where V_{Bi2Te3}, V_{Sb2Te3}, M_{Bi2Te3}, M_{Sb2Te3}, K, c_0, and T_a are the atomic volume of Bi_2Te_3, that of Sb_2Te_3, the average atomic mass of Bi_2Te_3, that of Sb_2Te_3, the bulk modulus of Sb_2Te_3, the concentration of Bi_2Te_3 in $(Bi_{0.25}Sb_{0.75})_2Te_3$ and the sample annealing temperature. Because Te-MS is an alloy between Sb_2Te_3 (75%) and Bi_2Te_3 (25%), the γ_1 estimated for Te-MS is 1.1 strengthening the scattering from the dislocation strain field (Eqn. 5.8_ by a factor of ~2.2. Although this strengthening factor would vary depending on the details of alloys considered, the factor of 2.2 was physically attainable (order of magnitude wise) when considering that of copper-aluminum alloy[109] (10 atomic % Al), which was experimentally estimated to be ~2[(110)].

Moreover, because the spacing between dislocations situated in grain boundaries of Te-MS (~2.5 nm) is smaller than the wavelength of most phonons (the median phonon wavelength contributing to κ_l of Bi_2Te_3 is approximately 3.6 nm according to Wang's calculation[111]) those parallel dislocations can be grouped into one dislocation with larger effective Burgers vector ($B_{\mathrm{D,eff}}$)[106,112] fortifying the scattering from dislocation strain (Eqn. 5.8). However, owing to the uncertainty involved in this compounding effect and characterization of Burgers vector in dislocation arrays, the $B_{\mathrm{D,eff}}$ was fit to the experimental κ_l of Te-MS (green empty circles in Fig. 5.1). The fit $B_{\mathrm{D,eff}}$ value (12.7 Å) is reasonable when compared to the reported Burgers vectors in Bi_2Te_3[113]. The theoretical κ_l of Te-MS (green solid line in Fig. 5.1) agrees well with the measured data (green empty circles in Fig. 5.1) showing how effective scattering by dislocations is for reducing κ_l. Individual relaxation times chosen to calculate κ_l of BM, S-MS, and Te-MS at high temperatures (T > 300 K) are shown in Table 5.2.

Table 5.2 Contributions to the total relaxation rate (τ_{total}^{-1}) used to model κ_l of BM, S-MS and Te-MS samples from ref. 1 at high temperatures ("HT grey model" in Fig. 5.1 only).

Sample	τ_{total}^{-1}
BM	$\tau_U^{-1} + \tau_{PD}^{-1} + \tau_{B(d_{\mathrm{BM}},\, \alpha_t=1)}^{-1}$
S-MS	$\tau_U^{-1} + \tau_{PD}^{-1} + \tau_{B(d_{\mathrm{MS}},\, \alpha_t=1)}^{-1}$
Te-MS	$\tau_U^{-1} + \tau_{PD}^{-1} + \tau_{B(d_{\mathrm{MS}},\, \alpha_t=1)}^{-1} + \tau_{DS}^{-1} + \tau_{DC}^{-1}$

5.3 Estimation of bipolar thermal conductivity at $T > 300$ K

Significant bipolar effects were present in the thermal conductivities of all three samples (BM, S-MS, and Te-MS) at high temperatures as observed in Fig 5.1. The bipolar contributions (κ_{bp}) were estimated by a two (parabolic) band model (an extension of a single parabolic band model (SPB)[8]) assuming acoustic phonon scattering. In the two band model, thermoelectric parameters of each band (valence and conduction bands in this case) computed from Boltzmann transport equations (see ref. 8) can be substituted into the following equations,

$$\sigma_{total} = \sum_i \sigma_i \ , \qquad \text{(Eqn. 5.11)}$$

$$S_{total} = \frac{\sum_i S_i \sigma_i}{\sum_i \sigma_i} \ , \qquad \text{(Eqn. 5.12)}$$

$$R_{H\,total} = \frac{\sum_i R_{Hi} {\sigma_i}^2}{(\sum_i \sigma_i)^2} \ , \qquad \text{(Eqn. 5.13)}$$

$$\kappa_{total} = \kappa_l + \sum_i L_i \sigma_i T + \left(\sum_i {S_i}^2 \sigma_i - S^2 \sigma\right) T \ , \qquad \text{(Eqn. 5.14)}$$

where R_{Hi} and L_i are the Hall coefficient and the Lorenz number of each band (properties with subscript *i* represent those of an individual band), respectively, used to calculate the total thermoelectric properties from the two bands. In Eqn. 5.14, $\sum_i L_i \sigma_i T$ and $\left(\sum_i {S_i}^2 \sigma_i - S^2 \sigma\right) T$ describe electronic and bipolar contributions to the total thermal conductivity, respectively. The κ_{bp} of the BM, S-MS, and Te-MS samples were taken from $\left(\sum_i {S_i}^2 \sigma_i - S^2 \sigma\right) T$.

In order to obtain theoretical κ_{bp}, calculated σ_{total} and S_{total} of one sample were fitted to experimental electrical conductivity and Seebeck coefficient of the sample by adjusting deformation potentials and density-of-states (DOS) effective masses (m^*) of its valence and conduction bands (Table 5.3). Due to high crystal symmetry of $Bi_{0.5}Sb_{1.5}Te_3$, more than one pocket of Fermi surface contribute to m^* as $m^* = N_V^{2/3} m_b^*$ where N_V and m_b^* are the valley (pocket) degeneracy and the band-mass of a single valley, respectively. While the N_V for the highest valence band of $Bi_{0.5}Sb_{1.5}Te_3$ is known to be 6 (Fig. 3.1c) that for the lowest conduction band is found to be 2 as listed in Table 5.3[41]. Since $Bi_{0.5}Sb_{1.5}Te_3$ is a *p*-type material, its carrier concentration of holes (p) and electrons (n) follow the charge neutrality equation,

$$p = N_{AC} + n, \qquad \text{(Eqn. 5.15)}$$

where N_{AC} is the number of acceptors. The R_{Hi} (inversely proportional to p for valence band and n for conduction band) was calculated by fitting N_{AC}, for experimental R_{Hi} data at high temperatures (> 300 K) were not available.

Table 5.3 Band parameters used to model κ_{bp} of the BM, S-MS and Te-MS samples from ref. 1 using the two band model at high temperatures ("HT grey model" in Fig. 5.1 only).

Band parameters	BM	S-MS	Te-MS
Valence band (VB) E_{def}[†] (eV)	10.5	9.45	8.75
VB m^* (in m_0)[‡]	1.33	1.33	1.33
VB N_V[§]	6	6	6
Conduction band (CB) E_{def}[†] (eV)	8.34	10.6	12.4
CB m^* (in m_0) [‡]	0.79	0.79	0.79
CB N_V[§]	2	2	2
No. of acceptors (10^{-19} cm^{-3})	2.22	2.00	1.75
Energy band gap (eV)	0.145	0.145	0.145
C_l (GPa)[‖]	35	35	35

[†] E_{def} = deformation potential
[‡] m^* = density-of-states effective mass (m_0 = electron mass)
[‖] C_l = longitudinal elastic constant
[§] N_V = number of valley degeneracy

The approximated κ_{bp} for each sample was added to corresponding κ_l predicted above to obtain theoretical $\kappa_l + \kappa_{bp}$ in Fig. 5.1 (solid lines). These results are labelled as "HT grey model" for BM and S-MS because

the frequency-independent boundary scattering term (grey model) in Eqn. 5.3 was used to model κ_l at high temperature (HT). For Te-MS sample, it is called "HT grey + dislocation" as dislocation scattering terms (Eqns. 5.7 and 5.8) were included in addition to the boundary scattering (Eqn. 5.3) to explain phonon scattering at grain boundaries of the Te-MS sample (Table 5.2).

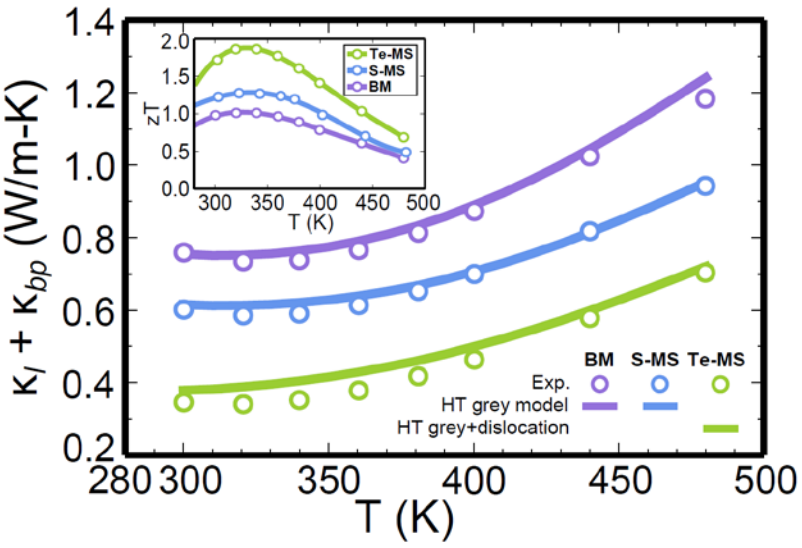

Fig. 5.1. Lattice and bipolar contributions to thermal conductivities of BM, S-MS, and Te-MS samples of ref. 1. Empty circle – experimental data, solid line – sum of calculated κ_l and κ_{bp}. Corresponding experimental zT curves are given in the inset.

5.4 Lattice thermal conductivity model for T < 200 K

At low temperatures, the frequency-independent boundary scattering dominates (${\tau_B}^{-1} \sim \omega^0$). Among the other scattering mechanisms considered to calculate the "HT grey model" ("HT grey + dislocation" for Te-MS) in Fig. 5.1, the dislocation scattering from strain field (${\tau_{DS}}^{-1} \sim \omega^1$, Eqn. 5.8) is also prominent due to its frequency dependence. As the scattering from the dislocation strain field is stronger than that from the core (${\tau_{DC}}^{-1} \sim \omega^3$, Eqn. 5.7)[105], especially at low temperature it can be concluded that the scattering from grain boundary dislocations (strain field + core) and the boundary scattering play a vital role in determining the low temperature κ_l.

The κ_l of the S-MS and Te-MS samples were measured at low temperatures (T < 200 K) by a Quantum Design Physical Property Measurement System (PPMS). Because the average grain size for both the samples was 300 nm (the same boundary scattering effect), by comparing their κ_l the effect of dense dislocation arrays, only observable in the Te-MS sample, on reducing κ_l at low temperature could be examined more closely.

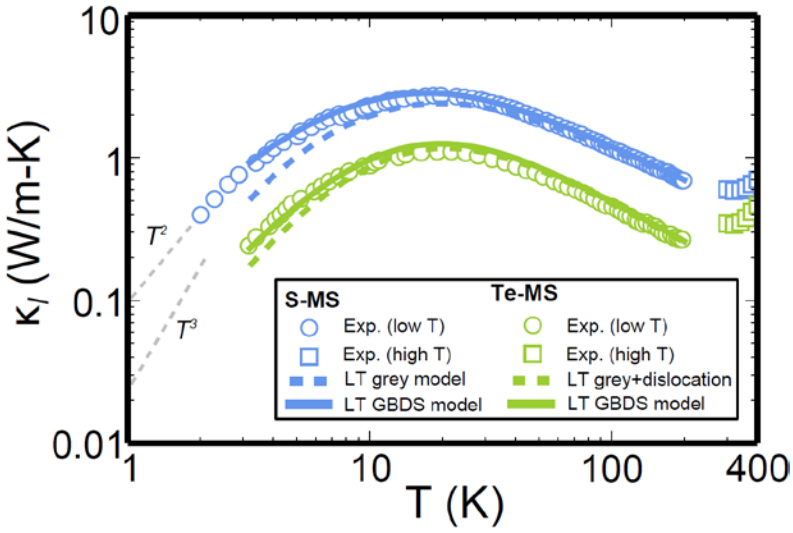

Fig. 5.2. Lattice contribution to thermal conductivities of the S-MS, and Te-MS samples. Empty circle – experimental data measured with PPMS at T < 200K, empty square – experimental data measured by laser-flash method using TC-9000, ULVAC-Riko at T > 300K, dashed line – calculated κ_l with "LT grey model" ("LT grey + dislocation" for Te-MS), and solid line – calculated κ_l with "LT GBDS model".

Similar to the high temperature κ_l calculation (T > 300 K), Umklapp, point-defect, and boundary scatterings were taken into account to compute low temperature κ_l of S-MS. However, different equation for Umklapp scattering ($\tau_{U,LT}{}^{-1}$ for low temperatures) and α_t > 1 (from Eqn. 5.3) were employed while utilizing the same $\tau_{PD}{}^{-1}$ as in Eqn. 5.5. The $\tau_{U,LT}{}^{-1}$ has an exponential term ($e^{(-\theta_a/3T)}$) as[18]

$$\tau_{U,LT}{}^{-1} = A_{N,LT}\frac{\hbar\gamma^2\omega^2 T}{M v^2 \theta_a} e^{(-\theta_a/3T)}, \qquad \text{(Eqn. 5.16)}$$

where $A_{N,LT}$ is a fitting parameter that accounts for the momentum-conserving Normal scattering contribution. The absence of this exponential term in $\tau_U{}^{-1}$ (Eqn. 5.4) makes it only applicable at high temperatures. As grain boundaries of a polycrystalline material are not as effective as sample boundaries in

limiting phonon mean free path, it is not surprising that the phonon mean free path can be much greater than the grain size at low temperatures[114,115] (hence $\alpha_t > 1$). The total scattering relaxation rates for the low temperature κ_l calculation of the S-MS and Te-MS samples are given in Table 5.4 including the parameters required for the computation (in addition to the ones in Table 5.1).

Table 5.4. Contributions to the total relaxation rate ($\tau_{total,LT}^{-1}$) and related parameters used to model κ_l of S-MS and Te-MS samples at low temperatures (Fig. 5.2 only).

Model	Sample	$\tau_{total,LT}^{-1}$	$A_{N,LT}$	α_t	$B_{D,\mathrm{eff},LT}$ (Å)	N_D (cm^{-2})
LT grey	S-MS	$\tau_{U,LT}^{-1} + \tau_{PD}^{-1} + \tau_{B_{(d_{\mathrm{MS}},\, \alpha_t>1)}}^{-1}$	3	8.3	–	–
LT grey + dislocation	Te-MS	$\tau_{U,LT}^{-1} + \tau_{PD}^{-1} + \tau_{B_{(d_{\mathrm{MS}},\, \alpha_t>1)}}^{-1} + \tau_{DC}^{-1} + \tau_{DS}^{-1}$	10	8.3	3.3	2×10^{11}
LT GBDS	S-MS	$\tau_{U,LT}^{-1} + \tau_{PD}^{-1} + \tau_{DC}^{-1} + \tau_{DS}^{-1}$	3	–	3.3	5.2×10^{10}
	Te-MS	$\tau_{U,LT}^{-1} + \tau_{PD}^{-1} + \tau_{DC}^{-1} + \tau_{DS}^{-1}$	10	–	3.3	2.1×10^{11}

For low temperature κ_l of the S-MS sample calculated using "LT grey model" (blue dashed line in Fig. 5.2), $\alpha_t = 8.3$ was obtained (Table 5.4). The name "LT grey model" originates from the frequency-independent τ_B^{-1} (Eqn. 5.3) used in the model. For $T < 20$ K, the trend of experimental data of the S-MS (blue empty circle in Fig. 5.2) differed from that of the "LT grey model" (blue dashed line). The slope of the "LT grey model" below 20 K was not affected by changing α_t.

Once a reasonable fit between the experimental data and the "LT grey model" was achieved in the S-MS sample, the same scattering mechanisms and parameters (i.e. $A_{N,\,LT}$ and α_t) were adopted for the Te-MS sample (with the same composition and grain size). To account for the fact that the Te-MS sample had dense dislocations at grain boundaries which were not observed in the S-MS sample, dislocation scattering relaxation rates were also included to determine $\tau_{total,LT}^{-1}$ of the Te-MS (Te-MS "LT grey + dislocation" in Table 5.4). A larger $A_{N,LT}$ for Te-MS than for S-MS was required to describe the low κ_l of Te-MS at ~200 K (lower than that of S-MS). Nonetheless this discrepancy did not influence the κ_l behavior at $T < 20$ K where the Umklapp scattering is negligible. Furthermore the large measurement error systematically present in PPMS at higher end of the low temperatures[116] (~100 K) might provide an explanation for different $A_{N,LT}$ obtained for S-MS and Te-MS (Table 5.4). Experimental κ_l measured via laser-flash method for $T > 300$ K

(empty square in Fig. 5.2) were also provided for reference. The further reduction of κ_l in Te-MS compared to S-MS at low temperatures was explained with added phonon scattering from dislocations ("LT grey + dislocation" - green dashed line in Fig. 5.2) with the effective Burgers vector close to Bi_2Te_3 lattice constant and the dislocation density (N_D = 2×10^{11} cm^{-2}) also used in "HT grey + dislocation" (Table 5.4). Unfortunately, the reason for $B_{D,eff,LT}$ (for LT model) being different from $B_{D,eff}$ (for HT model) is not known.

5.5 Frequency-independent boundary scattering at low temperature

Below 10 K in Fig. 5.2, particularly for the S-MS sample, the "LT grey model" deviated from the experimental data (~T^2 trend for measured data and ~T^3 for S-MS "LT grey model" – guided with dashed lines in grey color). According to Wang *et al.*[117], the discrepancy between the experiment and the "LT grey model" (dashed lines in Fig. 5.2) stemmed from frequency-independent boundary scattering relaxation rate ($\tau_B{}^{-1}$ in Eqn. 5.3) utilized in the model. Wang *et al.* showed that the use of frequency-dependent boundary scattering relaxation rate,

$$\tau_{B,\omega}{}^{-1} \sim \frac{v}{\alpha_t d}\omega \,, \qquad \text{(Eqn. 5.17)}$$

much improved the predictive power of κ_l modelling at low temperatures. In Fig. 5.2, Te-MS "LT grey + dislocation" (green dashed line) followed closer to ~T^2 instead of ~T^3 as in S-MS "LT grey model". This was because the scattering from dislocation strain field ($\tau_{DS}{}^{-1} \sim \omega^1$) considered along with the frequency-independent boundary scattering (Eqn. 5.3) in Te-MS "LT grey + dislocation" contributed to $\tau_{total,LT}{}^{-1}$ greater than $\tau_B{}^{-1}$ did due to the significant scattering of dislocation strain field from the dense dislocation arrays.

As an alternative to the frequency-dependent boundary scattering suggested by Wang *et al.*[8], the frequency-independent boundary scattering term (Eqn. 5.3) was completely substituted by dislocation scattering terms (Eqns. 5.7 and 5.8). This model is named as low temperature grain boundary dislocation strain model ("LT

GBDS model") as the frequency-independent boundary scattering term is completely removed from $\tau_{total,LT}^{-1}$ (Table 5.4). Although the dense dislocation arrays were not observed in the S-MS sample, as grain boundaries were composed of dislocations by definition replacing boundary scattering by scattering from disloctions formed at grain bounries was not far-stretched.

As presented in Table 5.4, for S-MS "LT GBDS model", with theoretical dislocation density of 5.2×10^{10} (cm^{-2}) (with the same $B_{D,eff,LT}$ as in Te-MS "LT grey + dislocation"), the boundary scattering could be translated into the scattering by dislocations at grain boundaries (blue solid line in Fig. 5.2). For the Te-MS sample, where the dislocation scattering term was already present even when "LT grey + dislocation" was used, removing the boundary scattering was compensated only by 5 % increase in the dislocation density ("LT GBDS model" in Table 5.4 and green solid line in Fig. 5.2). As expected, according to "LT GBDS model", about 5 time denser dislocation density was required to predict the κ_l of Te-MS (green solid line in Fig. 5.2) as opposed to that of S-MS (blue solid line in Fig. 5.2).

At low temperature, drastic lattice thermal conductivity reduction in Te-MS was observed. We modelled the low temperature κ_l of Te-MS satisfactorily with grain boundary dislocation scattering. Although the parameters in the phonon scattering mechanisms differ between the high and low temperature models for the κ_l calculation, both models provide strong evidence for the presence of grain boundary dislocation scattering in polycrystalline $(Bi_{0.25}Sb_{0.75})_2Te_3$.

Chapter 6

Dislocation strain as the mechanism of phonon scattering at grain boundaries

This section contains contents reproduced with permission from *Materials Horizons* (2016).
DOI: 10.1039/C5MH00299K.

6.1 Introduction

A Reduction of lattice thermal conductivity has been one of the most productive routes towards improving thermoelectric figure of merit[10]. The thermal conductivity, κ, can be attributed to heat transported along with the conduction of electrons and holes (κ_e), and from phonons (lattice vibrations) travelling through the lattice (κ_l). The lattice thermal conductivity, κ_l, can be suppressed with disorder among many length scales, ranging in size from as small as an atom (point-defect scattering) up to a few millimeters (boundary scattering)[118]. The effects of boundary scattering especially are of utmost importance for thermoelectric performance.

Boundary scattering was first observed in a single crystal by de Haas and Biermasz[119]. The phonon scattering at sample boundaries was explained by Casimir[120] who suggested that the phonon mean free path (MFP) could be approximated as the sample size (frequency-independent). The frequency independence of the Casimir model means that the sample boundaries are just as effective at limiting the MFP of short wavelength phonons as they are for long wavelength phonons. The Casimir model could be considered phenomenological, in the sense that it does not specify a real condition (at the atomic level) of the interface.

Berman suggested that scattering of phonons at grain boundaries could limit the MFP the same way phonon scattering on sample boundaries did, and since then the grain size of polycrystalline materials has been adopted as the MFP in the Casimir model (also known as grey model)[114,121]. Although it may be suitable to

use sample dimension as the MFP due to perfect acoustic mismatch at perfectly rough sample surfaces, it is not entirely appropriate for grain size because adjacent grains have similar acoustic impedance.

Recently, Wang *et al.* demonstrated that the grey model failed to explain the κ_l of nanocrystalline silicon[117]. At low temperature, it was observed that the measured κ_l followed a T^2 trend instead of a T^3, which was predicted in the grey model. This result implies a MFP that depends on frequency as $\Lambda_B^{-1} \sim \omega$, where Λ_B and ω are the boundary scattering MFP and phonon frequency, respectively.

Frequency-dependent Λ_B was first introduced by Ziman in an attempt to apply the Casimir model to materials with real boundaries[104]. Roughness of sample boundaries was taken into consideration in a frequency-dependent specularity term included in the Λ_B. However, the Ziman model did not predict $\Lambda_B^{-1} \sim \omega$; it can be considered a phenomenological term. Hua and Minnich[122] successfully predicted Wang *et al.*'s results via Monte Carlo simulations which included frequency-dependent phonon transmissivity at grain boundaries[117] (consistent with $\Lambda_B^{-1} \sim \omega$). The frequency-dependent interfacial (Kapitza) resistance of grain boundaries manifested itself even in molecular-dynamics simulations[123,124]. For example, Young and Maris[125] found phonon transmission coefficient decreasing with increasing frequency for the Kapitza resistance at an interface between two dissimilar solids. Moreover, the thermal conduction in thin films was commonly depicted with Fuchs-Sondheimer equation with the frequency-dependent specularity term from the Ziman model[126-128]. Unfortunately, above models and simulations for frequency-dependent Λ_B are only phenomenological without any mechanisms because they do not specify real conditions of the boundaries.

In this work, we propose that interface scattering could be due to strain at grain boundaries described analytically as dislocation strain as formulated by Klemens[105]. Here we show that the κ_l calculated previously with the grey model can be equally satisfactorily modelled with Klemens' grain boundary dislocation scattering term by using appropriate value for dislocation density. A most promising example is a recent demonstration of exceptional zT (~1.86 at 320 K) in $Bi_{0.5}Sb_{1.5}Te_3$ where grain boundary dislocations are produced by liquid-phase compaction[1]. The grey model plus dislocation scattering we used

in Kim *et al.*[1] is here entirely replaced by the dislocation scattering. The dislocation model demonstrates its superiority by predicting a T^2 trend instead of the T^3 of the grey model for the nanocrystalline silicon system of Wang *et al.*[117].

Finally we show that the Klemens model suggests dislocation boundary scattering can be enhanced by engineering compositional changes around dislocations in alloys as observed in silicon-germanium alloys[129-131] (not predicted by Casimir model).

6.2 Models for phonon scattering

From the kinetic theory of gases, the lattice thermal conductivity (κ_l) can be expressed as arising from the heat capacity of phonons (C), phonon velocity (v), and total relaxation time (τ_{total}), as a function of ω such that

$$\kappa_l = \frac{1}{3}\int C(\omega)\, v^2(\omega)\, \tau_{\text{total}}(\omega)\, d\omega. \qquad \text{(Eqn. 6.1)}$$

Using the Debye model (phonon group velocity is constant), Callaway's equation for the κ_l becomes

$$\kappa_l = \frac{k_B}{2\pi^2 v}\left(\frac{k_B T}{\hbar}\right)^3 \int_0^{\theta/T} \frac{\tau_{\text{total}}(z)\, z^4 e^z}{(e^z-1)^2}\, dz, \qquad \text{(Eqn. 6.2)}$$

where k_B, $\hbar$, θ, and z are the Boltzmann constant, reduced Planck's constant, Debye temperature, and $\hbar\omega/k_B T$, respectively[97]. The κ_l of a material can be calculated using Eqn. 6.2, once its τ_{total} (z) is determined from individual relaxation times (τ_i) for different scattering processes according to Matthiessen's rule

$$\tau_{\text{total}}(z)^{-1} = \sum_i \tau_i(z)^{-1} = {\tau_U}^{-1} + {\tau_{PD}}^{-1} + {\tau_B}^{-1}. \qquad \text{(Eqn. 6.3)}$$

Relaxation times associated with Umklapp scattering (τ_U), point-defect scattering (τ_{PD}), and frequency-independent boundary scattering (τ_B), which assumes completely inelastic (specularity zero) scattering at the grain boundaries are most commonly considered. The τ_B has been found to be a good model for surfaces

(of nanowires for instance) where there is perfect acoustic mismatch at the interface between the material and vacuum. Frequency-independent τ_B is given by[63]

$$\tau_B{}^{-1} = \frac{v}{d}, \qquad \text{(Eqn. 6.4)}$$

where d is the experimentally determined grain size. Umklapp scattering occurs when phonons in a crystal are scattered by other phonons. Its relaxation time is of the form[63]

$$\tau_U{}^{-1} = A_N \frac{2}{(6\pi^2)^{1/3}} \frac{k_B V^{1/3} \gamma^2 \omega^2 T}{M v^3}, \qquad \text{(Eqn. 6.5)}$$

where V, γ, and M are the atomic volume, Grüneisen parameter, and the atomic mass. The parameter A_N takes normal phonon-phonon scattering (total crystal momentum conserving process) into account[98]. Point-defect scattering arises from an atomic size disorder in alloys. The disorder is described in terms of the scattering parameter (Γ) within the τ_{PD} formula as[82]

$$\tau_{PD}{}^{-1} = \frac{V\omega^4}{4\pi v^3}\Gamma. \qquad \text{(Eqn. 6.6)}$$

In Eqn. 6.6, Γ is related to the difference in mass (ΔM) and lattice constant (Δa) between two constituents of an alloy as[18]

$$\Gamma = x(1-x)\left[\left(\frac{\Delta M}{M}\right)^2 + \frac{2}{9}\left\{(G + 6.4\gamma)\frac{1+r}{1-r}\right\}^2 \left(\frac{\Delta a}{a}\right)^2\right], \qquad \text{(Eqn. 6.7)}$$

where x and r are the fractional concentration of either of constituents and the Poisson ratio, respectively. The parameter (G) represents material dependent ($\Delta K/K$)($R/\Delta R$) where ΔK and ΔR are the contrast in the bulk modulus and that in the local bond length, respectively. The G was regarded as an adjustable parameter in the calculation.

Phonon scattering of dislocations in a grain boundary can be treated as resulting from scattering by dislocation cores (τ_{DC}) and by the dislocation strain (τ_{DS}) as[105,106]

$$\tau_{DC}^{-1} = \left(\frac{2}{sd}\right)\frac{V^{4/3}}{v^2}\omega^3 , \qquad \text{(Eqn. 6.8)}$$

$$\tau_{DS}^{-1} = 0.6 \times B_{\mathrm{D,eff}}^2\left(\frac{2}{sd}\right)(\gamma+\gamma_1)^2\omega\left[\frac{1}{2}+\frac{1}{24}\left(\frac{1-2r}{1-r}\right)^2\left\{1+\sqrt{2}\left(\frac{v_L}{v_T}\right)^2\right\}^2\right], \qquad \text{(Eqn. 6.9)}$$

where $B_{\mathrm{D,eff}}$, γ, γ_1, v_L, and v_T are the magnitude of effective Burgers vector, Grüneisen parameter, change in Grüneisen parameter, longitudinal phonon velocity, and the transverse phonon velocity, respectively. The change in Grüneisen parameter (γ_1) in τ_{DS}^{-1} describes the modulation of solute atom concentration by strain fields around dislocations in alloys. Initially, Klemens derived Eqns. 6.8 and 6.9 for collections of single dislocations (with density N_D) within a grain. As dislocations could be easily introduced into grains by deformation, Klemens' equations were often used to compute κ_l of strained materials[132,133]. When arrays of dislocations at boundaries (or interfaces) were found physically equivalent to a sum of individual dislocations within a grain[104], κ_l reductions from dislocations, which originated due to lattice mismatch between thin film and substrate[134], or between different phases in polycrystalline materials[81] were explained by Klemens' equations. Nevertheless, the consideration of the scattering effect of dislocation arrays at grain boundaries of single-phase polycrystalline materials has been scarce. Here we replace the density of dislocations per unit area (N_D) used by Klemens with $N_D \approx 2/(d \times s)$, where d is the average grain size and s is the average spacing between dislocation cores in order to apply Klemens equations to phonon scattering of grain boundary dislocations where average grain size can be an observed parameter.

6.3 Dislocation scattering can explain κ_l without the need for boundary scattering

Recently, a dramatic zT improvement in $Bi_{0.5}Sb_{1.5}Te_3$ was attributed to substantially low κ_l[(1)]. In ref. 1 we showed that modelling the boundary scattering with the normally expected τ_B^{-1} along with the experimentally determined $\tau_U^{-1} + \tau_{PD}^{-1}$ was insufficient to explain the low κ_l of $Bi_{0.5}Sb_{1.5}Te_3$ with dense dislocation arrays at grain boundaries. The additional scattering mechanisms, τ_{DC}^{-1} and τ_{DS}^{-1} from

dislocations were required to explain the κ_l. In this section we show that within the range of physically reasonable parameters, once dislocation scattering is included, since an array of dislocations situated in the plane makes a grain boundary[64] the traditional boundary scattering τ_B^{-1} is not necessary to satisfactorily model the data.

In ref. 1 various forms of $Bi_{0.5}Sb_{1.5}Te_3$ samples were considered to self-consistently model the κ_l. The parameters A_N and G in τ_U^{-1} and τ_{PD}^{-1} (Eqns. 6.5 and 6.6), respectively were determined by fitting the modelled κ_l to the experimental κ_l of large grained $(Bi_{1-x}Sb_x)_2Te_3$ alloys[99] with varying x. The use of reliable literature values determined experimentally eliminates or minimizes the parameters needed for the κ_l calculation.

The κ_l of the samples fabricated via different processing routes (Ball milling: BM, melt spun with stoichiometric tellurium: S-MS, and melt spun with excess tellurium: Te-MS) were modelled using the τ_B^{-1} expected from the average grain size (d) observed in the microscopy ("grey model" in Table 6.1) where significant bipolar contributions (κ_{bp}) were present at high temperatures. For BM and S-MS samples, the scattering terms $\tau_U^{-1} + \tau_{PD}^{-1} + \tau_B^{-1}$ were sufficient to explain the κ_l. However, the Te-MS required the introduction of dislocation scatterings τ_{DC}^{-1} and τ_{DS}^{-1} using values of the observed N_D and the fitted $B_{D,eff}$ as listed in Table 6.1, "grey + dislocation". The fitted $B_{D,eff}$ was within reasonable expectation[113], especially considering the compounding effect leading to reinforcement of grain boundary dislocation scattering expected by Klemens[105].

Table 6.1. Theoretical total relaxation rate (τ_{total}^{-1}) considered for grey model and GBDS model.

Sample	$\tau_{\text{total}}(z)^{-1} = \tau_U{}^{-1} + \tau_{PD}{}^{-1} + \tau_i{}^{-1}$									
	grey model ("grey + dislocation" for Te-MS)					GBDS model				
	$\tau_i{}^{-1}$	$B_{\text{D,eff}}$ (Å)	d (μm)	s (nm)	N_D (cm^{-2})	$\tau_i{}^{-1}$	$B_{\text{D,eff}}$ (Å)	d (μm)	s (nm)	N_D (cm^{-2})
BM	$\tau_B{}^{-1}$	-	20	-	-	$\tau_{DC}{}^{-1} + \tau_{DS}{}^{-1}$	12.7	20	9.1	1.1×10^{9}
S-MS	$\tau_B{}^{-1}$	-	0.3	-	-	$\tau_{DC}{}^{-1} + \tau_{DS}{}^{-1}$	12.7	0.3	21.5	3.1×10^{10}
Te-MS	$\tau_B{}^{-1} + \tau_{DC}{}^{-1} + \tau_{DS}{}^{-1}$	12.7	0.3	3.3	2.0×10^{11}	$\tau_{DC}{}^{-1} + \tau_{DS}{}^{-1}$	12.7	0.3	3.0	2.2×10^{11}

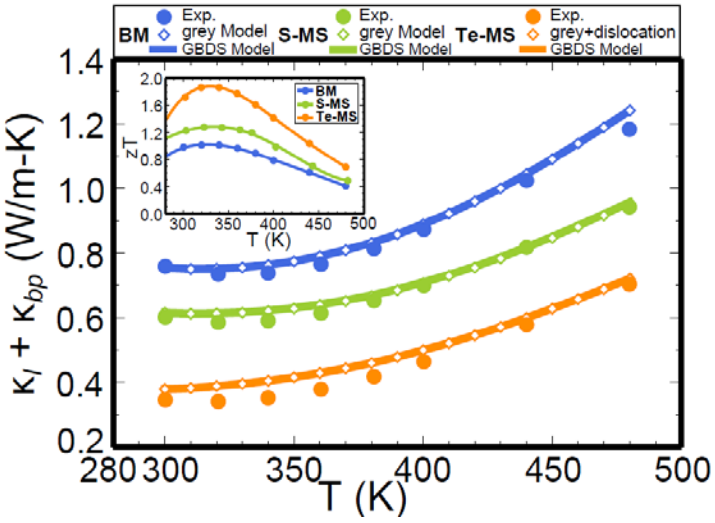

Fig. 6.1. Lattice and bipolar contribution to thermal conductivity of BM, S-MS, and Te-MS samples. Filled circle – experimental data, empty diamond – frequency-independent boundary scattering model (grey model), and solid line – grain boundary dislocation strain scattering model (GBDS model).

Now that we have concluded that $\tau_{DC}{}^{-1}$ and $\tau_{DS}{}^{-1}$ are required to model some of the grain boundary scattering in some samples, we can explore the possibility of this mechanism replacing the $\tau_B{}^{-1}$ term entirely to model all of the boundary scattering in all the samples studied.

Indeed, an equally satisfactory model exists by entirely replacing the $\tau_B{}^{-1}$ term in $\tau_{total}{}^{-1}$ of BM, S-MS, and Te-MS with $\tau_{DC}{}^{-1}$ and $\tau_{DS}{}^{-1}$ by using reasonable values of $B_{\text{D,eff}}$ and N_D as shown in Table 6.1 ("GBDS model"). The scattering from strain field induced by the dislocations is stronger than that from dislocation cores[105]. Therefore the scattering by grain boundary dislocations (from both strain field and

cores) is termed as grain boundary dislocation strain (GBDS) scattering for simplicity. The $B_{\mathrm{D,eff}}$ and γ_1 values were kept unchanged from those acquired for Te-MS in the "grey + dislocation".

There are different kinds of grain boundaries, consisting of different kinds of defects, that produce the strain that scatters phonons. Nevertheless, it has been suggested that most if not all defects at grain boundaries can be described as some combination of dislocations[105,135-140]. Even if all types of grain boundaries cannot be entirely defined by dislocations, the usefulness of GBDS model requires only that dislocation strain is a dominant mechanism for boundary scattering.

Smaller grain size, d, which leads to increased scattering in ${\tau_B}^{-1}$ ("grey model") translates into a larger dislocation density (N_D) in "GBDS model" (Table 6.1). Besides, the stronger GBDS (given the same d) which could not be described in terms of phenomenological ${\tau_B}^{-1}$ was taken into account in a greater N_D. Therefore, N_D for different samples were fit to the experimental κ_l (κ_{bp} is the same for both models, more details on estimation of the κ_{bp} can be found in Chapter 5.3) whose numbers are given in Table 6.1 ("GBDS model").

Previously, the N_D estimated from experimentally determined dislocation spacing in Te-MS and used in "grey + dislocation" was 2.0×10^{11} (cm^{-2})[1], but with only a 10% increase in N_D, 2.2×10^{11} (cm^{-2}) (which is still physically reasonable), we can equally adequately describe the exceptionally low κ_l of Te-MS using "GBDS model" (orange solid line in Fig. 6.1). As anticipated, much weaker scatterings from GBDS in BM and S-MS are manifested in their fitted N_D (Table 6.1), which are one or two orders magnitude smaller than that of Te-MS while in the range expected for polycrystalline materials[141]. Similar results can be applied to PbTe given removing boundary scattering by GBDS scattering can sufficiently explain the data like we show in Bi-Sb-Te.

Effect of scatterings from dislocation cores and strain field can be best understood when the spectral thermal conductivity (κ_s) is plotted.

$$\kappa_s = \frac{3k_B\omega^2}{2\pi^2 v}\tau(\omega) \qquad \text{(Eqn. 6.10)}$$

As described in the κ_s for S-MS (Fig. 6.2), while Umklapp scattering is effective in all frequency range, point defect scattering and boundary scattering (frequency-independent) only scatter high and low frequency phonons, respectively. Similar to the boundary scattering (green line – grey model), dislocation cores and strain field scatterings reduce thermal conductivity at low frequencies (orange line – GBDS model). Although the κ_s curves for the grey model (green curve Fig 6.2) and the GBDS model (orange curve Fig 6.2) do not coincide exactly in Fig. 6.2, their κ_l agree well (green curves Fig 6.1) with each other because the κ_l is the area under the κ_s curve.

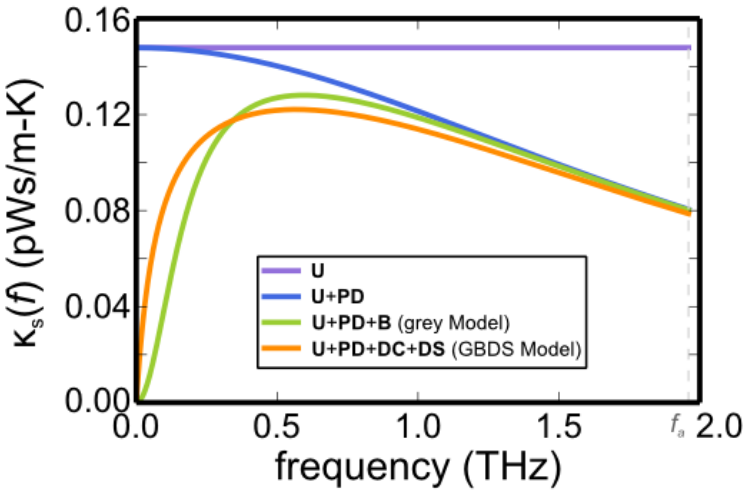

Fig. 6.2. Spectral thermal conductivity of S-MS. U (Umklapp), PD (Point-Defect), and B (frequency-independent Boundary scattering) are accounted for the calculation. For grey model, U, PD, and B are considered as relevant scattering mechanisms (green solid line). Meanwhile, in GBDS model B has entirely been replaced by DC and DS (orange solid line).

6.4 Dislocation scattering model superior to boundary scattering model at low temperatures

In a recent study by Wang *et al.* on nanocrystalline Si[117], it was shown that the traditional frequency-independent boundary scatterings fails to correctly predict the observed κ_l, even qualitatively. The grey model predicts a T^3 temperature dependence (green dotted line in Fig. 6.3) while the experimental measurements show a temperature dependence closer to T^2 at low temperatures.

Wang *et al.* were able to predict a T^2 temperature dependence using Born von Karman (BvK) model (group velocity is not constant), along with frequency-dependent boundary scattering relaxation rate ($\tau_{B,\omega}{}^{-1}$) approximated as

$$\tau_{B,\omega}{}^{-1} = c\frac{v\omega}{d}, \qquad \text{(Eqn. 6.11)}$$

where c is the dispersion relation dependent constant. The model in ref. 117, however, is phenomenological in that no mechanism was given for the frequency dependence (although it is consistent with atomistic calculations predicting the same frequency dependence).

Here we propose that GBDS may be the mechanism that leads to the frequency dependence. Because the GBDS model includes both a dislocation strain field term with ω dependence and a dislocation core term with ω^3 dependence (for scattering relaxation rates) it cannot exactly reproduce the model in ref. 117, instead we show the GBDS model gives a satisfactory fit (Fig. 6.3). All the parameters and constants from Debye model in ref. 117 were re-utilized except for the boundary scattering, which was replaced by $\tau_{DC}{}^{-1}$ and $\tau_{DS}{}^{-1}$. The γ_l for Si was taken to be zero as Si is not an alloy, and for simplicity, lattice constant of Si (5.4 Å) was substituted for $B_{\mathrm{D,eff}}$. Similar to the $(Bi_{0.25}Sb_{0.75})_2Te_3$ case, the dislocation spacing (s) was adjusted to match the experimental results. The fitted s (0.76 ~ 0.94 nm) for nanocrystalline Si was still above the minimum theoretical dislocation spacing (lattice constant ~ 0.5 nm). The fit is nearly as good

as the frequency-dependent BvK model in ref. 117, suggesting dislocation scattering may be the underlying mechanism in κ_l reduction due to grain boundary scattering.

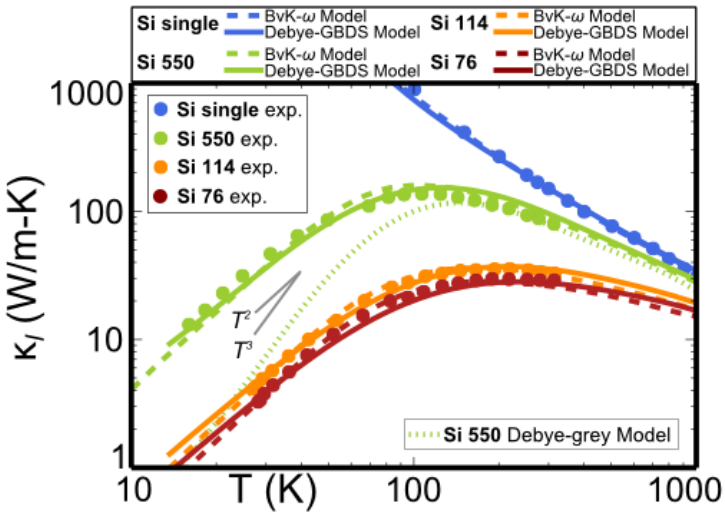

Fig. 6.3. Lattice contribution to thermal conductivity of various Si samples. Si single (Si single crystal), Si 550 (nanocrystalline Si with 550 nm average grain size), Si 114 (nanocrystalline Si with 114 nm average grain size), and Si 76 samples (nanocrystalline Si with 76 nm average grain size) are plotted. Filled circle – experimental data, dashed line – Wang and Dames' Born von Karman model using frequency-dependent boundary scattering model ("BvK-ω model"), and solid line – Wang and Dames' Debye model using our GBDS scattering model in lieu of Wang and Dames' frequency-dependent boundary scattering model ("Debye-GBDS model"). For comparison, Wang and Dames' Debye model using frequency-independent boundary scattering ("Debye-grey model") for Si 550 is plotted in green dotted line.

6.5 Alloys

Experimental κ_l data of Si-Ge alloys by Savvides and Goldsmid[129,130] were also examined to show that the GBDS model can replace the grey model completely, which also revealed a new strategy for further suppressing κ_l. This mechanism utilizes the change in Grüneisen parameter that accompanies the compositional changes around dislocations in alloys.

The change in Grüneisen parameter (γ_1) of ${\tau_{DS}}^{-1}$ can strengthen or weaken the scattering due to GBDS depending on mass and volume mismatch between constituents of the alloy. The γ_1 can be estimated as

$$\gamma_1 = \frac{V c_0 K}{k_B T_a}(\gamma\alpha^2 - \alpha\beta) \ , \qquad \text{(Eqn. 6.12)}$$

with α and β being

$$\alpha = \frac{(V'-V)}{V}, \quad \beta = \frac{1}{2}\frac{(M-M')}{M}, \qquad \text{(Eqn. 6.13)}$$

where V', V, M', M, K, c_0, and T_a are the atomic volume of impurity, that of host, average atomic mass of impurity, that of host, bulk modulus of host, concentration of impurity in the alloy, and the sample annealing temperature, respectively. For Te-MS, which is a $(Bi_{0.25}Sb_{0.75})_2Te_3$ alloy, the theoretical γ_1 is positive reinforcing the GBDS scattering[1].

Savvides and Goldsmid[129,130] compared the relative change in κ_l from nanostructuring for different Si-Ge alloy compositions. In particular, they plotted the κ_l ratio of polycrystalline Si-Ge with different grain sizes (containing boundaries and point defects, $\kappa_{PD,B}$) relative to that of single crystal alloy (containing only point defects, κ_{PD}). Simply comparing two 30% alloys (Fig. 6.4) cannot provide any information on relative strength of the boundary scatterings in the alloys since the Fig. 6.4 plots the ratio of $\kappa_{PD,B}$ and κ_{PD}. In fact, according to Savvides and Goldsmid's calculated $\kappa_{PD,B}/\kappa_{PD}$ using the grey model (dashed lines in Fig. 6.4), less intense point-defect scattering in $Si_{0.7}Ge_{0.3}$ was held responsible for the lower $\kappa_{PD,B}/\kappa_{PD}$ of $Si_{0.7}Ge_{0.3}$.

Replacing the τ_B^{-1} in the Savvides and Goldsmid' model with the GBDS model, a reasonable fit to the experimental data was achieved (solid lines in Fig. 6.4) considering the uncertainty involved in determining the size of the grains (represented with error bars in Fig. 6.4).

For $Si_{0.7}Ge_{0.3}$ and $Si_{0.3}Ge_{0.7}$, $s = B_{D,eff} = 7$ Å (in Eqns. 6.8 and 6.9) was adopted to produce the solid lines in Fig. 6.4. Even if the effective Burgers vector is larger than that normally expected for Si and Ge (5.4 Å and 5.5 Å, respectively), given the uncertainty of the models, we can still deduce that the GBDS model can provide an alternative to the Casimir model for boundary scattering.

If GBDS is indeed the correct mechanism for boundary scattering, the Klemens theory implies that the scattering due to impurity modulation around grain boundary dislocation strain field in Si-Ge alloys plays a vital role in further reducing the κ_l. The change in Grüneisen parameter (γ_1 in Eqn. 6.12) of the Si-Ge alloys increase the overall Grüneisen parameter ($\gamma + \gamma_1$) in Eqn. 6.12 by 3.4 times for $Si_{0.7}Ge_{0.3}$ and about

2.1 times for $Si_{0.3}Ge_{0.7}$ reinforcing GBDS scattering accordingly. Now that the increased GBDS scattering becomes the dominant scattering mechanism, the discrepancy in $\kappa_{PD,B}$ / κ_{PD} for the two 30% alloys can be explained with the degree of impurity modulation (γ_1). The theoretical γ_1 for various thermoelectric materials are listed in Table 6.2.

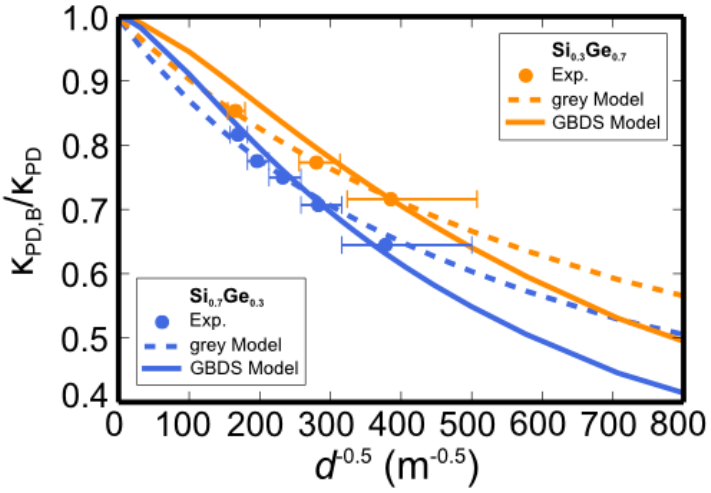

Fig. 6.4. Ratio of thermal conductivities whose departure from unity measures the boundary scattering effect. The ratio between $\kappa_{PD,B}$ (κ_l where point-defect and boundary scatterings are present) and κ_{PD} (κ_l where only point-defect scattering is present) for different grain sizes (d) is shown at 300 K. Plots in orange are for $Si_{0.3}Ge_{0.7}$ alloy and blue for $Si_{0.7}Ge_{0.3}$ alloy. Filled circle – experimental data, dashed line – Savvides and Goldsmid' model using grey model (grey model), and solid line – Savvides and Goldsmid' model using our GBDS scattering model in lieu of the grey model (GBDS model).

Table 6.2. Theoretical change in Grüneisen parameter (γ_1) for thermoelectric materials.

Material	α	β	γ	K (GPa)	T_a (K)	γ_1	$(\gamma + \gamma_1) / \gamma$
$(Bi_{0.25}Sb_{0.75})_2Te_3$	0.09 [a]	-0.18	2.3 [b]	45 [d]	753 [c]	1.1	1.49
$PbTe_{0.75}Se_{0.25}$	-0.15 [a]	0.07	1.45 [a]	39 [d]	700 [e]	1.4	1.99
$Pb_{0.97}Mg_{0.03}Te$	-0.02 [a]	0.27	1.45 [a]	39 [d]	700 [e]	0.03	1.02
$Si_{0.7}Ge_{0.3}$	0.13 [f]	-0.79	0.56 [a]	98 [d]	1200 [g]	1.3	3.32
$Si_{0.3}Ge_{0.7}$	-0.12 [f]	0.31	0.76 [a]	75 [d]	1200 [g]	0.8	2.07
$Mg_2Si_{0.7}Sn_{0.3}$	0.19 [a]	-0.09	1.32 [a]	49 [d]	1000 [h]	1.6	2.20

Taken from: [a]ref. 63; [b]ref. 142; [c]ref. 1; [d]ref. 143; [e]ref. 144; [f]ref. 145; [g]ref. 146; [h]ref. 147

In summary, straightforwardly applicable frequency-dependent phonon scattering due to dislocation strain in grain boundaries (GBDS model as illustrated in Fig. 6.5) can replace the most commonly used frequency-independent boundary scattering (grey model) to accurately predict the κ_l. Although the grey model is in wide use, it has been difficult to align with observed phenomena. The theoretical κ_l of Bi-Sb-Te, Si, and Si-Ge previously modelled with grey model were recalculated using GBDS model with equally satisfactory results. At low temperatures, boundary scattering is better described with scattering due to GBDS. We revisited Wang *et al.*'s thermal conductivity calculation (Debye model) using frequency-independent boundary scattering ($\sim T^3$) which deviated from experimental thermal conductivity ($\sim T^2$) at low temperatures. Accuracy of the Debye model is much improved when frequency-independent boundary scattering is changed to GBDS scattering. It is concluded that the scattering from GBDS is the more likely mechanism for the grain boundary scattering than the grey model derived for boundary scattering at the sample boundaries. Strengthening of the GBDS scattering via impurity modulation around dislocations in alloys opens possibilities for grain boundary engineering as a means toward more efficient thermoelectric materials.

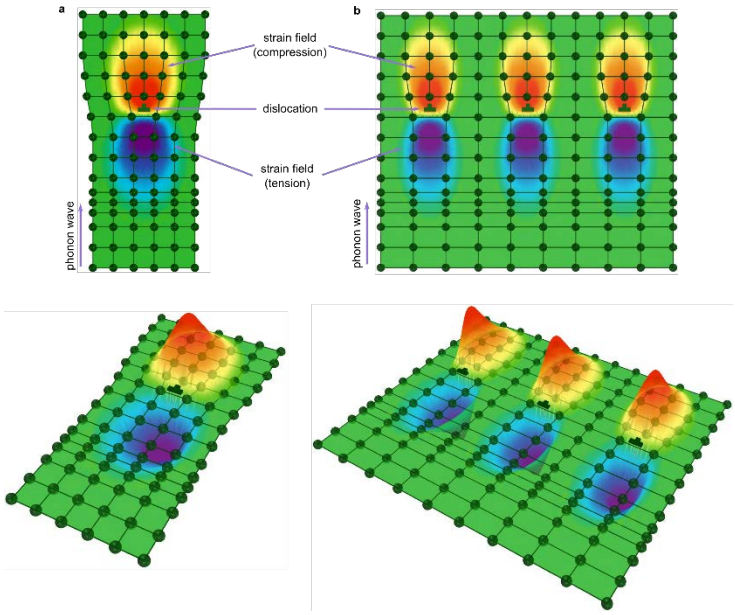

Fig. 6.5. Schematic diagram of phonon scattering by a single dislocation (a) and a grain boundary (b)

Chapter 7

Band gap estimation from temperature dependent Seebeck measurement

This section contains contents reproduced with permission from *Applied Physics Letters* **106**, 022112 (2015). DOI: 10.1063/1.4905922.

7.1 Introduction

In a typical plot of *zT* versus temperature for a good thermoelectric material (Figure 7.1 inset), the *zT* will rise until reaching a peak value after which it decreases. Since the peak *zT* values are often the measure by which materials are compared, it is worthwhile to understand the origins of the peak and what factors can influence it. Typical degenerate thermoelectric semiconductors display thermopower (magnitude of the Seebeck coefficient, |*S*|) which rises linearly with temperature to a maximum (Figure 7.1) followed by a decrease. Because the Seebeck coefficient is squared in the formula for *zT*, a maximum in the thermopower also results in a maximum in the temperature dependent *zT*.

It is well known that the origin of the thermopower peak is most often related to the onset of bipolar conduction which involves thermal excitation of both electrons and holes across the band gap. The contribution to the overall Seebeck coefficient by both the positive and negative charge carriers can be described by the conductivity weighted average:

$$S = \frac{\sigma_p S_p - \sigma_n |S_n|}{\sigma_p + \sigma_n} \quad . \qquad \text{(Eqn. 7.1)}$$

Because the minority carriers are (by definition) fewer in number, they will also have higher thermopower contributions (Seebeck coefficient is inversely proportional to carrier concentration). However, at low temperatures the population of minority carriers is small, meaning that they will not contribute much to the

overall *S*. At higher temperatures, though a broadening Fermi distribution leads to an exponential increase in minority carrier conductivity resulting in a reduction (and therefore peak) in the thermopower[148].

The strength of bipolar conduction is determined by the value of the semiconductor band gap. Goldsmid and Sharp developed an analytical expression relating the band gap and the maximum thermopower, $|S|_{max}$ (defined as the magnitude of the Seebeck coefficient), and the temperature at which it occurs (T_{max}) in the bipolar regime by: $E_g = 2e|S|_{max}T_{max}$[148]. This simple method of estimating the band gap is ubiquitous in the thermoelectrics community because temperature dependent Seebeck coefficient is so commonly measured. Figure 7.1 shows a calculated temperature dependent Seebeck coefficient and corresponding *zT* (inset) for a valence and conduction band model with a band gap of 0.13 eV at various carrier concentrations. We can see that the Goldsmid-Sharp band gap formula (dashed line) accurately predicts the maximum thermopower over a wide range of carrier concentrations and temperatures.

While the Goldsmid-Sharp gap serves as a quick estimate of the band gap in a given material, it is important to understand where deviations might occur when using this analysis. In Goldsmid-Sharp's full equation, the weighted mobility ratio: $A = \frac{\mu_{maj}N_{v,maj}}{\mu_{min}N_{v,min}}\left(\frac{m^*_{b,maj}}{m^*_{b,min}}\right)^{3/2} = \frac{\mu_{maj}}{\mu_{min}}(\frac{m^*_{maj}}{m^*_{min}})^{\frac{3}{2}} = \frac{B_{maj}}{B_{min}}$ (where μ is the mobility, N_v is the valley degeneracy, m^* and $m_b{}^*$ are the density-of-states and single valley effective mass, and *B* is the quality factor for majority and minority charge carriers) governs the relative contributions of the electron and hole bands to the electronic properties in the case of bipolar conduction. We can also consider *A* as the ratio of the quality factors, $B = \frac{\mu_0 m^{*3/2}}{\kappa_l}$ (where μ_0 is the non-degenerate mobility, and κ_l is the lattice thermal conductivity), between the majority and minority bands, which relate directly to the maximum attainable *zT* (for any doping level) for a given band[149-153]. One of the primary conclusions of the Goldsmid-Sharp paper was that the $2e|S|_{max}T_{max}$ band gap was within ~20 % of the actual value and was roughly independent of the weighted mobility ratio, but this assumed that the dimensionless band gap ($\epsilon_g = \frac{E_g}{k_B T}$) — the parameter that governs the strength of bipolar conduction — was equal to 10. For some common

thermoelectric materials (Bi_2Te_3[154,155], PbSe[156,157], PbTe[144,158]) the value of the band gap is actually 5 – 6 k_BT at T_{max}. Recent work by Schmitt, Gibbs *et al*. shows that for ZrNiSn half-Heuslers, the Goldsmid-Sharp band gap can deviate by 50 – 100 % of the optical band gap value mainly due to the large majority-to-minority weighted mobility ratio (A = 5) and an ϵ_g much lower than 10 as used in the derivations by Goldsmid-Sharp[159]. Further, because E_g is often within ~6 k_BT_{max} ($\epsilon_g \sim 6$), Maxwell-Boltzmann statistics — applied in Goldsmid-Sharp's derivation — should be replaced with Fermi-Dirac statistics which can more accurately represent semiconductor processes in narrow-gap ($\epsilon_g < 10$), heavily doped materials. We thoroughly probe the limitations of the $2e|S|_{max}T_{max}$ relation, particularly by exploring the effect of varying majority-to-minority weighted mobility ratio (A) and the dimensionless band gap (ϵ_g). We generate a chart that can be used to quickly estimate the relationship between the true and the Goldsmid-Sharp band gaps depending on A and $|S|_{max}$.

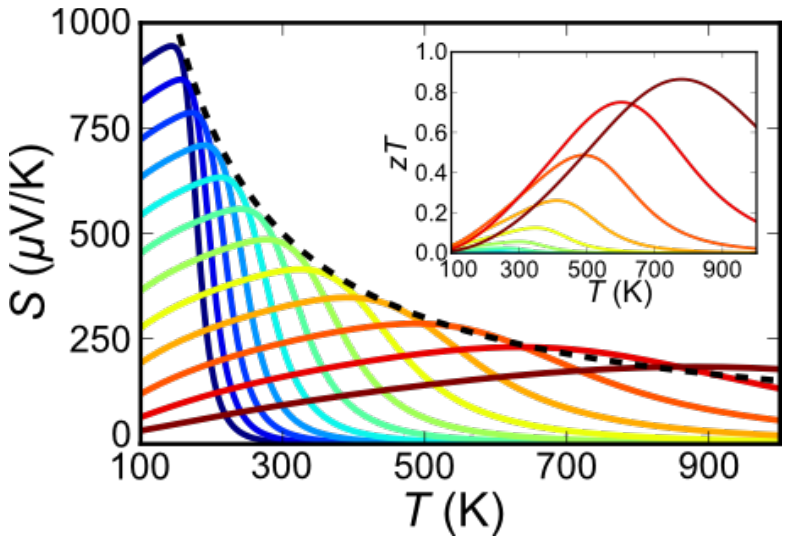

Fig. 7.1. Calculated temperature dependent Seebeck coefficient and zT (inset) for various defect concentrations ($N_{AC} = p - n = 1\times10^{15}$ cm^{-3} in blue to 1×10^{20} cm^{-3} in red) for two parabolic bands with a band gap of 0.13 eV, $m^* = 1.0\ m_e$, and $\mu_0(300\text{ K}) = 820\text{ cm}^2/\text{Vs}$ (valence and conduction bands). Dashed line indicates the Goldsmid-Sharp band gap: $S = E_g/2eT$. The lattice thermal conductivity was estimated as $\kappa_l(T) = 1.7\ (300/T)$ W/m-K, following Umklapp scattering is used for the zT estimate.

7.2 Different methods of estimating the $|S|_{max}$

The expression for the Seebeck coefficient in a multi band (valence/conduction) can be expressed by rearranging Eqn. 7.1[19]:

$$S = \frac{1}{1+\frac{\sigma_{maj}}{\sigma_{min}}}\left(S_{min} + \frac{\sigma_{maj}}{\sigma_{min}}S_{maj}\right) , \qquad \text{(Eqn. 7.2)}$$

where S, S_{maj}, and S_{min} are the overall, majority carrier, and minority carrier Seebeck coefficients, respectively. σ_{maj}, and σ_{min} are the majority and minority carrier conductivities, respectively. In the interest of maintaining general relationships applicable for either *p* or *n*-type materials, we chose to use the majority and minority carrier labels; in the case of a primarily *p*-type material, the majority carrier will be holes. While Goldsmid and Sharp proceed assuming Maxwell-Boltzmann, non-degenerate statistics: $\frac{\sigma_{maj}}{\sigma_{min}} = A\exp(\eta_{maj} - \eta_{min})$, where $A = \frac{\mu_{maj}N_{v,maj}}{\mu_{min}N_{v,min}}\left(\frac{m^*_{maj}}{m^*_{min}}\right)^{3/2}$, we will consider the Fermi integral solution to the Boltzmann transport equation (assuming scattering by acoustic phonons and parabolic bands). In this context, the Seebeck coefficient of a specific carrier type (S_i) and electrical conductivity ratio between the majority and minority carriers can be written as a function of the dimensionless chemical potential ($\eta = \xi/k_BT$) — where ξ is the electronic chemical potential:

$$S_i = \frac{k_B}{e}\left(\frac{2F_1(\eta_i)}{F_0(\eta_i)} - \eta_i\right) \qquad \text{(Eqn. 7.3)}$$

$$\frac{\sigma_{maj}}{\sigma_{min}} = A\frac{F_0(\eta_{maj})}{F_0(\eta_{min})} , \qquad \text{(Eqn. 7.4)}$$

where A has the same definition as in the Goldsmid-Sharp formulation and represents the weighted mobility ratio and F_j represents the Fermi integral:

$$F_j(\eta) = \int_0^\infty \frac{\epsilon^j d\epsilon}{1+\exp(\epsilon-\eta)} \ . \qquad \text{(Eqn. 7.5)}$$

Table 7.1. Description of the three different methods of estimating the maximum thermopower in this work.

Method Name	Criterion for Maximum	Statistics
Goldsmid-Sharp	$dS/d\eta = 0$	Maxwell-Boltzmann
Fermi	$dS/d\eta = 0$	Fermi
Exact	$dS/dT = 0$	Fermi

In order to find the maximum thermopower, several methods can be used as differentiated in Table 7.1. The derivation of the Goldsmid-Sharp band gap does not explicitly find the maximum in thermopower with temperature; rather, Goldsmid-Sharp find a maxima with respect to reduced chemical potential, $dS/d\eta = 0$, which is equivalent to $dS/dT = 0$ when $d\eta/dT$ is much larger than $\frac{d(\epsilon_g)}{dT}$ as pointed out by Goldsmid and Sharp[148]. In this work, the "Fermi" method (Table 7.1) also assumes $dS/d\eta = 0$, as in the "Goldsmid-Sharp" method, but it uses Fermi-Dirac rather than Maxwell-Boltzmann statistics. We can test the $dS/d\eta = 0$ approximation by performing a full, temperature dependent calculation of the Seebeck coefficient — the "Exact" method. This is accomplished by applying a charge counting balance, $N_{AC} - N_{DO} = p - n$, at various temperatures, where N_{AC} and N_{DO} are the number of electron acceptors and donors respectively, and p and n are the number of holes and electrons, respectively (for simplicity we have assumed that $A_{m^*} = \frac{m^*_{maj}}{m^*_{min}} = 1$). The full, temperature dependent, numerically calculated results ("Exact" method) will be presented along with the simpler $dS/d\eta = 0$ solutions using both Maxwell-Boltzmann ("Goldsmid-Sharp") and Fermi-Dirac ("Fermi") statistics. The expression for $\frac{dS}{d\eta}$ used in the "Fermi" method derived using the single parabolic band Fermi integrals with acoustic phonon scattering can be written as:

$$\frac{dS}{d\eta} = F_0(\eta)^2 - 2F_{-1}(\eta)F_1(\eta) + A\left[2F_1\left(-\eta - \frac{E_g}{k_B T}\right)F_{-1}(\eta) + F_0\left(-\eta - \frac{E_g}{k_B T}\right)\left\{\frac{E_g}{k_B T}F_{-1}(\eta) + 2F_0(\eta)\right\} + F_{-1}\left(-\eta - \frac{E_g}{k_B T}\right)\left\{\frac{E_g}{k_B T}F_0(\eta) + 2F_1(\eta)\right\}\right] + A^2\left[F_0\left(-\eta - \frac{E_g}{k_B T}\right)^2 - 2F_{-1}\left(-\eta - \frac{E_g}{k_B T}\right)F_1\left(-\eta - \frac{E_g}{k_B T}\right)\right] \quad .$$

(Eqn. 7.6)

7.3 Deviations from Goldsmid-Sharp band gap due to degeneracy

First, in order to probe the applicability Goldsmid-Sharp's assumption of Maxwell-Boltzmann (non-degenerate) statistics, Figure 7.2 considers a weighted mobility ratio of A = 1. Figure 7.2a shows the chemical potential dependent Seebeck coefficient (with η = 0 being the valence band edge, $\epsilon_g = 5$ being the conduction band edge). As expected, the "Goldsmid-Sharp" result overlaps well with the "Fermi" result for chemical potentials in the gap ($0 < \eta < 5$), but deviations begin for chemical potentials of about 1.5 $k_B T$ from either band edge which become larger as the chemical potential becomes degenerate (chemical potential within the band, $\eta < 0$ or $\eta > \epsilon_g = 5$).

Figure 7.2b quantifies the effectiveness of the $2e|S|_{max}T_{max}$ estimate for band gap at different ϵ_g for the three cases of interest: the $dS/d\eta = 0$ model using both the "Fermi" and "Goldsmid-Sharp" methods, as well as the $dS/dT = 0$ (or "Exact") case. For large ϵ_g, the "Fermi" and "Goldsmid-Sharp" solutions ($dS/d\eta = 0$) converge to $2e|S|_{max}T_{max}/E_g$ very near 1.0 (although the exact value is ~10 % less at ϵ_g = 10). However, as the band gap becomes small, (ϵ_g < ~5), $2e|S|_{max}T_{max}/E_g$ increases for all three methods. The divergence for small gaps is a consequence of increasingly degenerate chemical potentials which yield the maximum thermopower. Experimentally, this would be observed for heavily doped samples that do not reach a maximum thermopower until very high temperatures.

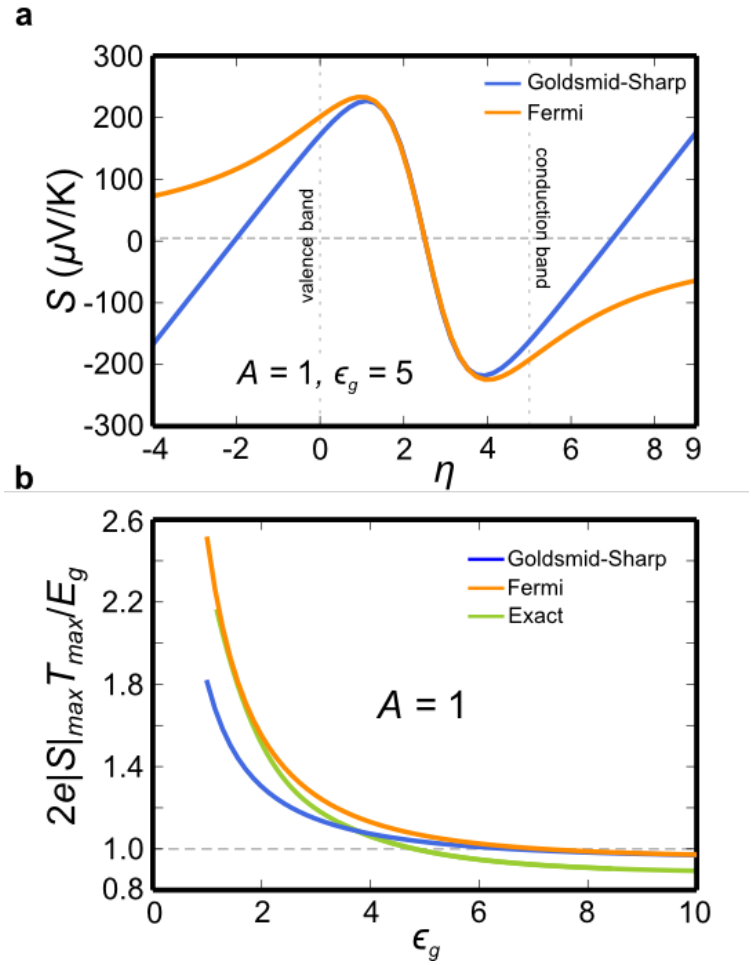

Fig. 7.2. Result of the "Exact", "Fermi", and "Goldsmid-Sharp" methods calculated assuming ϵ_g = 5 and A = 1 for (a) Seebeck coefficient as a function of η, (b) the ratio of the $2e|S|_{max}T_{max}$ estimate to E_g as a function of the dimensionless band gap ϵ_g.

7.3.1 Theoretical $|S|_{max}$ for materials with A = 1

Fig. 7.3a shows the magnitude of the maximum Seebeck coefficient predicted using the three different methods (as shown in Table 7.1). The result is useful for estimating the maximum attainable thermopower at a given temperature (which would be set to T_{max}) for a material which has an electron-to-hole weighted mobility ratio (A) near 1 and a known band gap. As demonstrated in Fig. 7.1, one would not be able to obtain higher thermopower regardless of extrinsic doping concentration. For example, E_g/k_BT for Bi_2Te_3 (A~1[160], E_g ~ 0.13 eV[160,161]) is ~5.2 for operation at room temperature (T_{max} = 300 K), yielding a maximum Seebeck coefficient near 230 μV/K — a reasonable estimate[162-165].

By evaluating $dS/d\eta$ = 0 from Fig. 7.2a for different dimensionless band gaps, the value of chemical potential (η_{max}) that yields these maxima can be obtained — the results are plotted in Fig. 7.3b. η_{max} converges with the classical solution from the "Goldsmid-Sharp" method when the band gap is larger than ~6 $k_B T$. Below this value, the η_{max} values start to deviate.

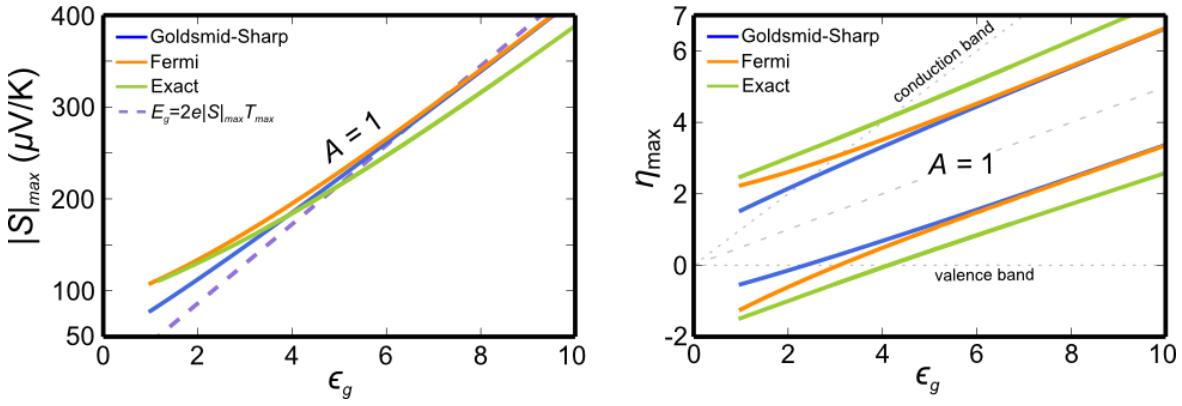

Fig. 7.3. Maximum attainable thermopower (a) and the reduced chemical potential which yields it (b) as a function of reduced band gap (at the rollover temperature). Dashed line in (a) represents the Goldsmid-Sharp band gap equation result. The dashed line (in the middle) in Figure (b) represents half way between the valence and conduction bands, the dotted grey lines represent the position of the valence and conduction bands. All calculations are done for a majority-to-minority carrier weighted mobility ratio of A = 1.

7.4 Deviations from Goldsmid-Sharp band gap due to weighted mobility ratio

We have shown that the degree of degeneracy can result in some deviations to the Goldsmid-Sharp band gap, but the weighted mobility ratio (A) can also play a substantial role. While Bi_2Te_3 has similar majority and minority carrier weighted mobility[160,161], other systems such as ZrNiSn[(159)], Si, Ge, and others[166], are believed to have values that exceed two (5 in the case of ZrNiSn). In order to illustrate the effect of an increasing weighted mobility ratio, the η-dependent Seebeck is plotted for ZrNiSn (ϵ_g ~ 5 at room temperature)[159] in Figure 7.4a. We see that the magnitude of the maximum Seebeck coefficient obtained for *p*-type ZrNiSn (A = 1/5) is significantly lower than that for *n*-type ZrNiSn (A = 5). The effect of having an A different from one is that the magnitude of the maximum Seebeck coefficient ($|S|_{max}$) as well as the

temperature where it occurs (T_{max}) is increased for the carrier type with higher weighted mobility while those of the lower weighted mobility carrier are decreased. So in a system like ZrNiSn, the *n*-type material maintains a high thermopower to much higher temperatures than might be expected from its narrow band gap (~0.13 eV) and therefore can reach an impressive zT from 0.5 – 1.0[167,168]. On the other hand, the *p*-type ZrNiSn prematurely experiences reduced thermopower due to compensating high-mobility electrons. In Figure 7.4b, it is obvious that $2e|S|_{max}T_{max}/E_g$ is larger than 1.0 for all values of ϵ_g when $A = 5$ while it is less than 1.0 for all ϵ_g for $A = 1/5$ (except at quite low ϵ_g). Figure 7.4c shows how $2e|S|_{max}T_{max}/E_g$ increases with increasing A values; larger deviations are observed as E_g/k_BT becomes smaller. In comparison with Goldsmid-Sharp's conclusion that only ~20% deviation is observed for $A = 10$, we find that 50 - 100% errors in the estimated gap can be obtained for ϵ_g values reasonable for many relevant thermoelectric materials (ϵ_g ~ 4 - 5).

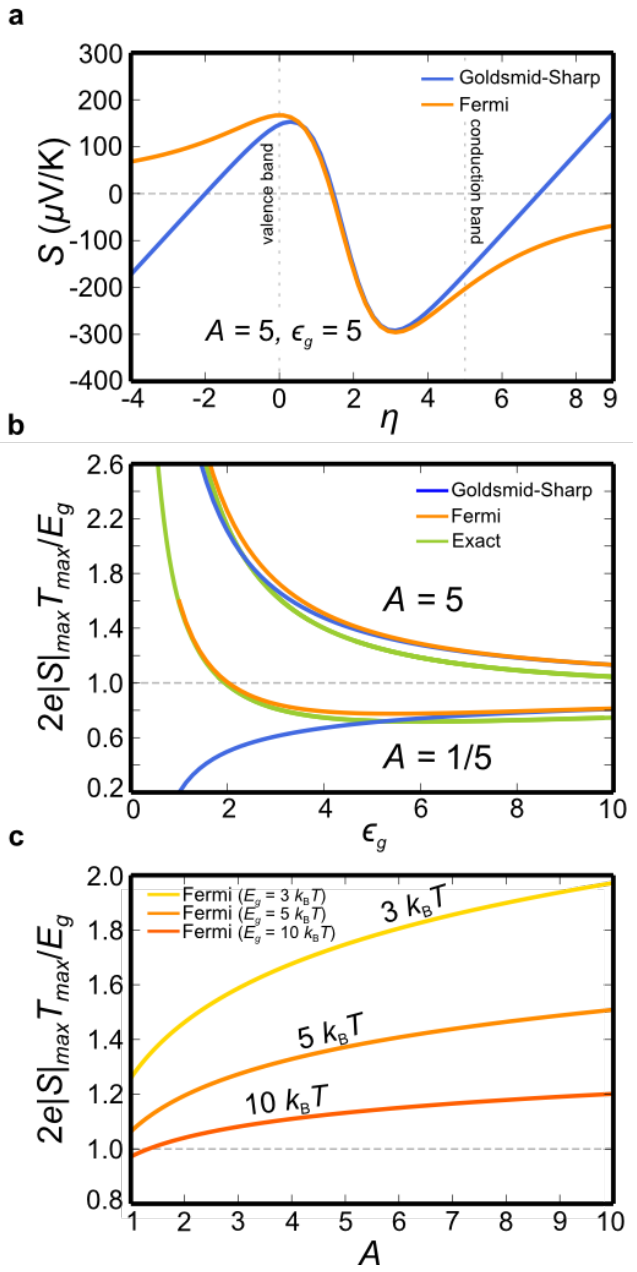

Fig. 7.4. Result of the "Exact", "Fermi", and "Goldsmid-Sharp" methods assuming ϵ_g = 5 and A = 5 (weighted mobility ratio) for (a) Seebeck coefficient as a function of η. (b) the ratio of the $2e|S|_{max}T_{max}$ estimate to the actual model E_g as a function of ϵ_g, and (c) the same ratio with respect to the weighted mobility ratio A at different E_g values (3, 5, and 10 k_BT as indicated on the figure).

7.4.1 Theoretical $|S|_{max}$ for materials with A = 5

In the case of non-unity A value, $|S|_{max}$ is always larger for the A=5 (majority carrier five times the weighted mobility as minority) case than for the A=1/5 (minority carrier five times the weighted mobility as majority) for all values of E_g/k_BT as shown in Fig. 7.5a. Although some differences between the "Goldsmid-Sharp"

and the other two methods occur for small values of E_g/k_BT in the A = 1/5 calculation (probably breaking down of the classical approximations in favor of Fermi statistics), all three methods show qualitatively the same trends. In terms of the chemical potential which yields the maximum Seebeck coefficient, Fig. 7.5b shows that if the majority carrier has a lower weighted mobility (A = 1/5), η_{max} tends to occur nearer to the band edge ($\eta_{max} = 0$ at a larger value of E_g/k_BT_{max}). This results in larger deviations from the Goldsmid-Sharp band gap.

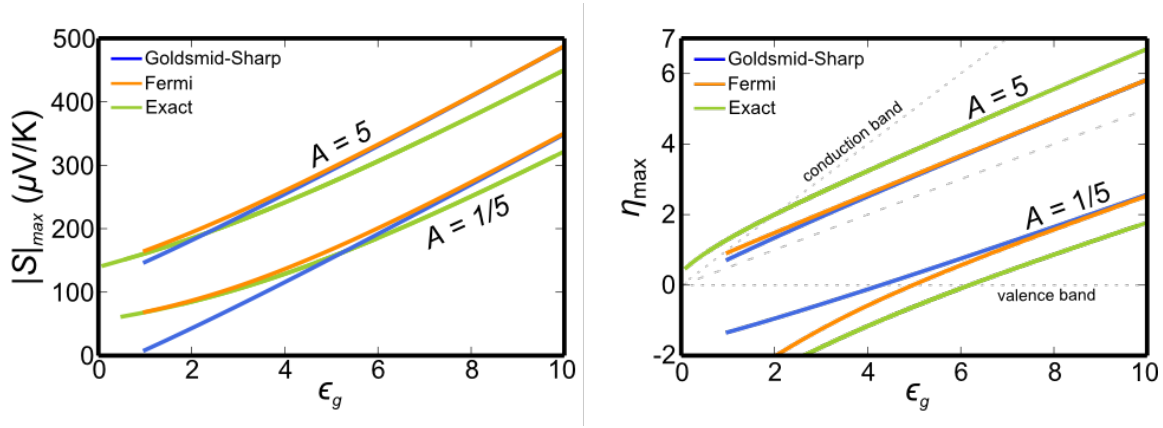

Fig. 7.5. Maximum attainable thermopower (a) and the reduced chemical potential which yields it (b) as a function of reduced band gap (at the rollover temperature). The dashed line in Figure (b) represents half way between the valence and conduction bands, the dotted grey lines represent the position of the valence and conduction bands. All calculations are done for a majority-to-minority carrier weighted mobility ratio of A = 5 and 1/5.

7.5 Engineering guide for estimation of the real band gap

While the Goldsmid-Sharp band gap has proven to be a simple and useful estimate for the real band gap, it is not without its limitations. In this work, we have shown several cases for which this simple approximation breaks down. Fig. 7.6 shows the deviation between the Goldsmid-Sharp band gap and the true band gap for a wide variety of these parameters. Ultimately, we observe that the magnitude of the deviation is largest for materials with large differences between the weighted mobility of electrons and holes ($A \neq 1$). From an experimental perspective, $A \neq 1$ will result in a larger value of $2e|S|_{max}T_{max}$ for the higher weighted mobility species, and a lower value for the one with lower weighted mobility. In the case of ZrNiSn, the more mobile

electrons (A = 5) result in an observation of about a five-fold difference in the *p*-type (~0.05 eV) and the *n*-type (~0.25 eV) Goldsmid-Sharp band gaps[159].

Figure 7.6 can be useful in determining either an unknown A value for a material if the true band gap is known, or it can show the expected deviations of the Goldsmid-Sharp band gap relative to the true band gap for a given A value. For instance, in the case of *n*-type ZrNiSn with $2e|S|_{max}T_{max}/E_g$ = 2.1 (using $E_{g,optical}$ = 0.13 eV[(159)]) and observed maximum Seebeck coefficient (~200 μV/K), we determine $A \sim 5$. Alternatively, if the majority-to-minority carrier weighted mobility ratio (A) is known, one can (based on the magnitude of the maximum Seebeck coefficient) obtain an estimate a value for $2e|S|_{max}T_{max}/E_g$ from Figure 7.6, which can be used to estimate the true band gap (as described in the numbered list below).

1. Measure temperature dependent thermopower and obtain a maximum
2. Calculate the Goldsmid-Sharp band gap: $E_g = 2e|S|_{max}T_{max}$
3. If $|S|_{max} < 150\ \mu$V/K, be aware that the true E_g may significantly differ from $2e|S|_{max}T_{max}$ (see below)
4. For $|S|_{max} > 150\ \mu$V/K, estimate the majority-to-minority carrier weighted mobility ratio, A.
5. Find the $2e|S|_{max}T_{max}/E_g$ ratio (r) from Figure 7.6 that is consistent with that A and S_{max} value to then calculate the corrected $E_g = 2e|S|_{max}T_{max}/r$

The $S_{max} < 150\ \mu$V/K describes the degenerate crossover that leads to the upward trend in Figure 7.6 mentioned previously for low values of S_{max}. For degenerate, heavily doped samples (η_{max} in the majority band) E_g/k_BT_{max} becomes a poor metric for describing the bipolar effects; rather, we believe the thermal band gap ($\frac{E_{g,thermal}}{k_BT} = \epsilon_g + \eta$) is the relevant parameter. This effect is even more pronounced as A is decreased because the lower mobility majority carrier requires a chemical potential deep within the band (large η) to mitigate the effects of a highly mobile minority carrier.

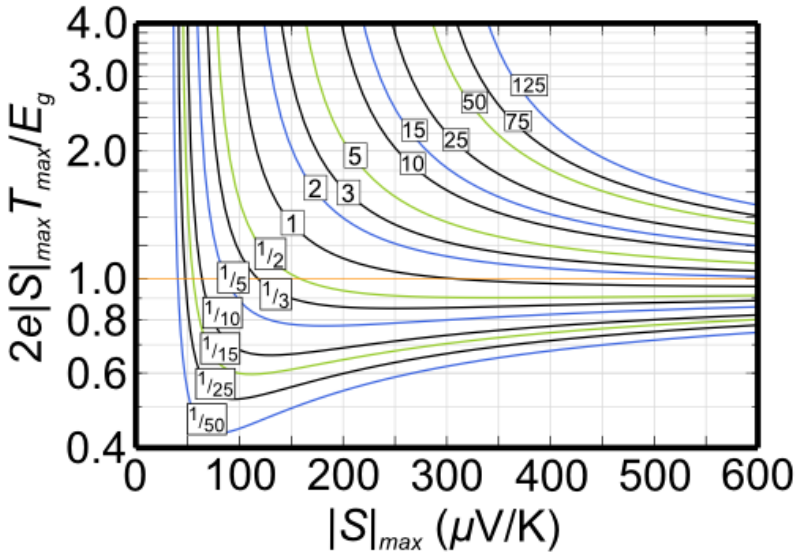

Fig. 7.6. The ratio of the $2e|S|_{max}T_{max}$ estimate to the actual model E_g as a function of thermopower for a wide variety of A and E_g values. A values are noted in a rectangular box laid on top of each solid lines in black, blue, and green.

In summary, the Goldsmid-Sharp band gap ($E_g = 2e|S|_{max}T_{max}$) is an extremely useful tool for obtaining an estimate for a material's band gap through temperature dependent Seebeck measurements. While most researchers understand that this is not an exact estimate, it is important to understand when and why the simple relation can break down and to what extent. In this work, we show that large deviations can occur for several reasons: a breakdown of Maxwell-Boltzmann statistics (used to derive the Goldsmid-Sharp band gap) for materials with narrow gaps, or materials with very large (or small) majority-to-minority carrier weighted mobility ratio (A). Because bipolar conduction is detrimental to thermoelectric performance, results from this work using the Goldsmid-Sharp gap could be used to validate strategies for suppressing bipolar effects beyond altering band gap and doping[155,169-171] but also by other methods (including nanostructures[27,172-174]) given that both *n*-type and *p*-type samples are obtainable.

Chapter 8

Characterization of Lorenz number with Seebeck coefficient measurement

This section contains contents reproduced with permission from *APL Materials* **3**, 041506 (2015).

8.1 Introduction

A semiconductor with large Seebeck coefficient, high electrical conductivity, and low thermal conductivity is a good candidate for a thermoelectric material. Because the charge carriers (electrons in *n*-type or holes in *p*-type semiconductors) transport both heat and charge, the electronic contribution to the thermal conductivity (κ_e) is commonly estimated from the measured electrical conductivity (σ) using the Wiedemann-Franz law: $\kappa_e = L\sigma T$, where L and T are the Lorenz number and the temperature, respectively. Once κ_e is known, lattice thermal conductivity (κ_l) is computed by subtracting the κ_e from the total thermal conductivity, $\kappa_{total} = \kappa_e + \kappa_l$. For this method, the bipolar thermal conductivity (κ_{bp}) will also be included, which can be written $\kappa_{bp} + \kappa_l = \kappa_{total} - L\sigma T$.

Since a high zT requires low κ_{total} but high σ simultaneously, one of the more popular routes towards improving zT has been to reduce κ_l[10]. However, depending on the value of L, which maps from σ to κ_e, the resulting κ_l can often be misleading. For instance, in the case of lanthanum telluride, incautious determination of L can even cause κ_l to be negative, which is not physical[175]. Therefore, careful evaluation of L is critical in characterizing enhancements in zT due to κ_l reduction.

For most metals, where charge carriers behave like free-electrons, L converges to $\frac{\pi^2}{3}\left(\frac{k_B}{e}\right)^2 = 2.44\times10^{-8}$ $W\Omega K^{-2}$ (degenerate limit). Although some heavily doped semiconductor thermoelectric materials have an L very close to the degenerate limit, properly optimized materials often have charge carrier concentrations

between the lightly doped (non-degenerate) and heavily doped (degenerate) regions[176] ($\xi_{optimum}$ is near the band edge where ξ is the electronic chemical potential) which can result in errors of up to ~40 %[(177)].

Direct measurement of L[(178)], requires high mobility — typically beyond that attainable at the temperatures of interest (> 300 K). Thus L is typically estimated either as a constant (2.44×10^{-8} WΩK^{-2}) or by applying a transport model — such as the single parabolic band (SPB) model obtained by solving the Boltzmann transport equations —to experimental data.

For example, Larsen *et al*. proposed an approximate analytical solution of L based on the SPB model as a function of carrier concentration (n) and $(m^*T)^{-3/2}$ (where m^* is the density-of-states effective mass) along with various sets of parameters for distinct carrier scattering mechanisms[179]. However, when the Hall carrier concentration, n_H, of a material is not available, the use of the approximate solution by Larsen is not possible. It can be shown that for the SPB model with acoustic phonon scattering (SPB-APS), both L and S are parametric functions of only the reduced chemical potential ($\eta = \xi/k_{\mathrm{B}}T$, where k_{B} is Boltzmann constant); thus no explicit knowledge of temperature (T), carrier concentration (n), or effective mass (m^*) is required to relate them[180]. We have utilized this correlation between L and measured S to estimate κ_l for a few known thermoelectric materials including: PbTe[(144,181,182)], Zintl materials[183-185], Co-doped $FeV_{0.6}Nb_{0.4}Sb$ Half Heusler[186], $La_{3-x}Te_4$[(175)], resulting in much more satisfactory values for κ_l than the degenerate limit result ($L = 2.44 \times 10^{-8}$ WΩK^{-2}) would have.

While the SPB model works well to estimate L, a transcendental set of equations is needed to solve for L in terms of S — requiring a numerical solution. Considering that the typical measurement uncertainty for κ_{total} is 10 % and that SPB-APS is only an approximation, a much simpler equation would supply sufficient accuracy. Here we propose the equation

$$L = 1.5 + \exp\left[-\frac{|S|}{116}\right], \qquad \text{(Eqn. 8.1)}$$

where L is in 10^{-8} WΩK^{-2} and S in μV/K) as a satisfactory approximation for L.

8.2 Lorenz number as a function of thermopower – from Single Parabolic Band model

We examine the *L* function in terms of *S* for the SPB-APS case and provide a simple expression relating the two (Eqn. 8.1). Eqn. 8.1 allows for a facile estimation of *L* from an experimental *S* only without requiring a numerical solution. We characterize the effectiveness of this estimate for *L* using some experimental data from some relevant thermoelectric materials (PbSe[187], PbS[188], PbTe[30,189], Zintl material (Sr_3GaSb_3)[183], Half Heusler (ZrNiSn)[190], and $Si_{0.8}Ge_{0.2}$[191]).

For a single parabolic band, *L* and *S* are both functions of reduced chemical potential (η) and carrier scattering factor (λ) only:

$$L = \left(\frac{k_B}{e}\right)^2 \frac{(1+\lambda)(3+\lambda)F_\lambda(\eta)F_{\lambda+2}(\eta)-(2+\lambda)^2F_{\lambda+1}(\eta)^2}{(1+\lambda)^2F_\lambda(\eta)^2} \qquad \text{(Eqn. 8.2)}$$

$$S = \frac{k_B}{e}\left(\frac{(2+\lambda)F_{\lambda+1}(\eta)}{(1+\lambda)F_\lambda(\eta)} - \eta\right), \qquad \text{(Eqn. 8.3)}$$

where $F_j(\eta)$ represents the Fermi integral:

$$F_j(\eta) = \int_0^\infty \frac{\epsilon^j d\epsilon}{1+Exp[\epsilon-\eta]}. \qquad \text{(Eqn. 8.4)}$$

By assuming that the carrier relaxation time is limited by acoustic phonon scattering (one of the most relevant scattering mechanisms for thermoelectric materials above room temperature[30,192]), Eqns. 8.2 and 8.3 can be solved numerically for *L* and the corresponding *S* as shown in Fig. 8.2 along with the proposed approximation (Eqn. 8.1).

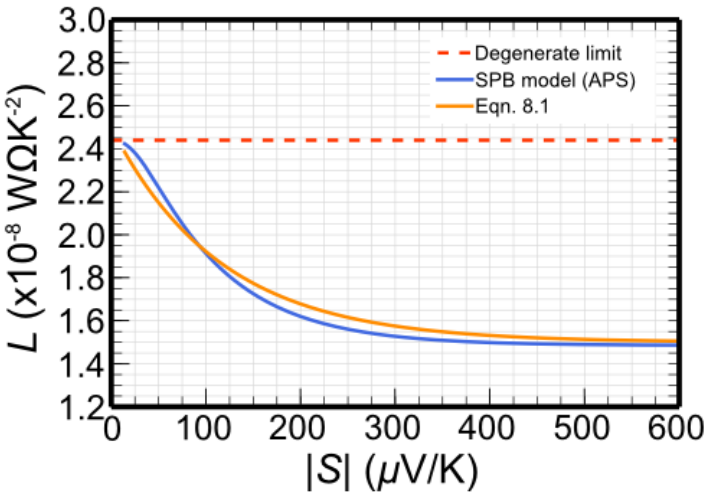

Fig. 8.1. Thermopower dependent Lorenz number calculated by the SPB model with APS, and Eqn. 8.1. For comparison, the degenerate limit of 2.44×10^{-8} WΩK^{-2} is also presented in a red dashed line.

According to the Fig. 8.1, the degenerate limit of L (2.44×10^{-8} WΩK^{-2}) is valid with errors less than 10 % for materials whose thermopower is smaller than 50 μV/K (highly degenerate). In contrast, if the thermopower is large, the discrepancy with the degenerate limit can be up to 40 %.

To decide an appropriate value of L with a known S easily, rather than graphically extracting it from Fig. 8.1, Eqn. 8.1 can be used to quickly estimate L, given a measured thermopower. Eqn. 8.1 is accurate within 5 % for single parabolic band where acoustic phonon scattering is dominant scattering mechanism when $|S|$ > ~10 μV/K. For $|S|$ < 10 μV/K, while the SPB model converges to the degenerate limit, Eqn. 8.1 increases exponentially, thus reducing the accuracy of the Eqn. 8.1. Although estimation of L with an accuracy within 0.5 % for SPB-APS is possible, this requires an approximate equation more complex than Eqn. 8.1 (see Chapter 8.5 for the more complex equation).

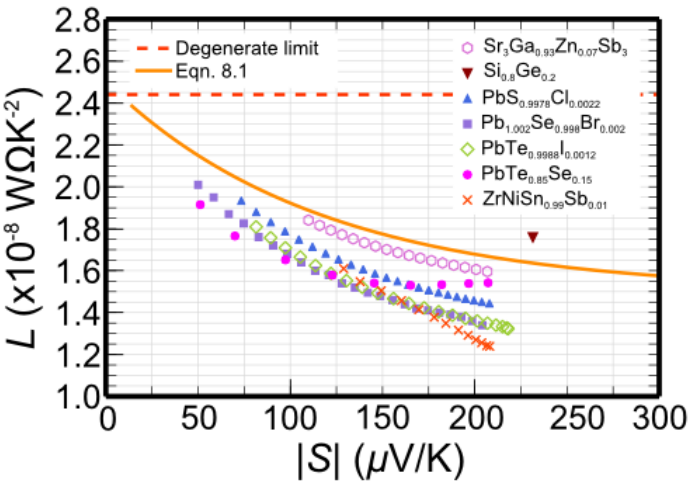

Fig. 8.2. Thermopower dependent Lorenz number obtained from materials whose band structure and scattering assumptions are different from those assumed in SPB-APS along with Eqn. 8.1 calculation. For comparison, the degenerate limit of 2.44 $\times 10^{-8}$ WΩK^{-2} is also presented in a red dashed line.

8.3 Lorenz number for non-parabolic band model

Exceptions are known where L has been found to be outside the uncertainty described above for SPB-APS which are presented in Fig. 8.2 and Table 8.1. Temperature dependent S and L were directly extracted from corresponding literature for $Sr_3Ga_{0.93}Zn_{0.07}Sb_3$[183], $ZrNiSn_{0.99}Sb_{0.01}$[190], and $PbTe_{0.85}Se_{0.15}$[30]. Pairs of S and L at each temperature were then plotted in Fig. 8.2. In cases of $PbTe_{0.9988}I_{0.0012}$[189], $Pb_{1.002}Se_{0.998}Br_{0.002}$ (labeled as 3E19 in the literature)[187], and $PbS_{0.9978}Cl_{0.0022}$ (4E19 in the literature)[188], temperature dependent L was calculated from temperature dependent resistivity ($\rho = 1/\sigma$), κ_{total}, and κ_l from $\kappa_l = \kappa_{total} - L\sigma T$ (temperature dependent S was given in the literature). For $Si_{0.8}Ge_{0.2}$[191], theoretical carrier concentration (n_c) dependent Hall mobility (μ_H) and κ_e were used to calculate theoretical n_c dependent σ and L using the relations: $\sigma = n_c e \mu_H$ and $\kappa_e = L\sigma T$. The acquired n_c dependent σ along with theoretical n_c dependent zT and κ_{total} given in the literature were utilized to obtain n_c dependent S at 1300 K ($zT = \sigma S^2 T / \kappa_{total}$). From the theoretical n_c dependent S and L, pairs of S and L at each n_c were extracted for $Si_{0.8}Ge_{0.2}$ at 1300 K. Since Vining provided experimental temperature dependent S (labeled as T373) in the range 700 K ~ 1300 K, the

S value at 1300K was taken for T373 and corresponding *L* was found from the theoretical pairs of *S* and *L*, where the theoretical *S* corresponds to that of T373.

These exceptions typically involve either non-parabolic band structures (PbTe, PbSe, PbS) or alternative scattering mechanisms (other than acoustic phonons). Narrow-gap semiconductors (lead chalcogenides for example) are often better described by the non-parabolic Kane model which yields a different η dependence of *L* and κ_e which depends on the non-parabolicity parameter: $\alpha = \frac{k_B T}{E_g}$ (ref. 17,193). For well-studied lead chalcogenides (PbTe, PbSe, PbS), a reasonable range of α is from 0.08 (300 K) to 0.16 (850 K)[9]. Figure 8.2 shows that *L* is at most ~26 % lower than that of the SPB-APS and Eqn. 8.1 result over the entire range of temperatures. In other words, κ_l estimates will maintain the order: $\kappa_{l,deg} < \kappa_{l,SPB-APS} < \kappa_{l,SKB-APS}$ (where SKB stands for the single Kane band model) with the largest errors being for the degenerate limit when applied in the non-degenerate case.

For narrow-gap semiconductors, because the energy gap (E_g) between the valence and conduction band extrema is small, the two nearest bands interact to each other making the energy dependence of crystal momentum non-quadratic, and effective mass a function of energy. A thermoelectric transport model incorporating the non-parabolicity of a band is called a single Kane band (SKB) model[194]. For a single Kane band (assuming acoustic phonon scattering), *L* and *S* are both functions of reduced chemical potential (η) and non-parabolicity parameter ($\alpha = \frac{k_B T}{E_g}$):

$$L = \left(\frac{k_B}{e}\right)^2 \left[\frac{{}^2F_{-2}^1}{{}^0F_{-2}^1} - \left(\frac{{}^1F_{-2}^1}{{}^0F_{-2}^1}\right)^2\right] \qquad \text{(Eqn. 8.5)}$$

$$S = \frac{k_B}{e}\left(\frac{{}^1F_{-2}^1}{{}^0F_{-2}^1} - \eta\right), \qquad \text{(Eqn. 8.6)}$$

where ${}^nF_k^m(\eta)$ represents the following integral with the Fermi-Dirac distribution, f:

$$ {}^{n}F_{k}^{m}(\eta) = \int_{0}^{\infty} \left(-\frac{\partial f}{\partial \epsilon}\right) \epsilon^{n} (\epsilon + \alpha\epsilon^{2})^{m} [(1 + 2\alpha\epsilon)^{2} + 2]^{k/2} d\epsilon \ . \qquad \text{(Eqn. 8.7)} $$

The thermopower dependent L calculated for different α using SKB model for acoustic phonon scattering is shown in Fig. 8.3. At a given temperature, the narrower the E_g gets (the larger the α), the more L deviates from the SPB result ("SPB model (APS)" in Fig. 8.3). Although it is not presented in the figure, the SKB result without non-parabolicity ($\alpha = 0,\ E_g \sim \infty$) exactly coincides with the SPB model result as there is no interaction between valence and conduction band due to their infinite separation. Narrow-gap thermoelectric materials ($PbTe_{0.9988}I_{0.0012}$[189], $Pb_{1.002}Se_{0.998}Br_{0.002}$[187], and $PbS_{0.9978}Cl_{0.0022}$[188], and $PbTe_{0.85}Se_{0.15}$[30]) require temperature dependent E_g (between conduction and valence bands) for accurate determination of S and L using SKB model (Eqns. 8.5 and 8.6 in functions of η and α for acoustic phonon scattering). For instance, E_g/eV = 0.17 + 4×10^{-4} T/K is employed for SKB model of $Pb_{1.002}Se_{0.998}Br_{0.002}$[187].

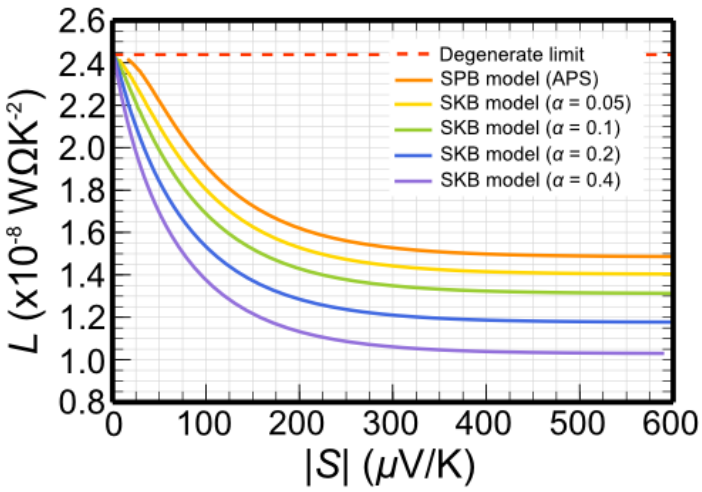

Fig. 8.3. Calculated thermopower dependent Lorenz number for a single Kane band with assumption of acoustic phonon scattering for different band non-parabolicity parameter (α). For comparison, the SPB-APS result (orange) and the degenerate limit of 2.44 ×10^{-8} WΩK^{-2} (red) are also presented.

Alternative scattering mechanisms can also yield deviations from the SPB-APS. For example, when ionized impurity scattering dominates (λ = 2), the L actually increases with increasing S, however, this example is not particularly prevalent in materials which have high dielectric constants (including the lead

chalcogenides)[195] or at high temperatures. At low temperatures (< 100 K), as *S* approaches zero, it is expected that *L* converges to the degenerate limit regardless of carrier scattering mechanism[180] and parabolicity of bands involved in transport. However, a pronounced inelastic electron-electron scattering due to high mobility of carriers decreases *L* from the degenerate limit, even for strongly degenerate materials. In case of *n*-type PbTe, *L* at 100 K is approximately 40 % lower than its value at 300 K[(17)].

When there is more than one dominant scattering mechanism affecting the transport of a non-parabolic band, Eqns. 8.5 and 8.6 need to be replaced by the following equations[188]:

$$L = \left(\frac{k_B}{e}\right)^2 \left[\frac{\int_0^\infty \left(-\frac{\partial f}{\partial \epsilon}\right)\tau_{total}(\epsilon)\,\epsilon^{7/2}(1+\alpha\epsilon)^{3/2}(1+2\alpha\epsilon)^{-1}d\epsilon}{\int_0^\infty \left(-\frac{\partial f}{\partial \epsilon}\right)\tau_{total}(\epsilon)\,\epsilon^{3/2}(1+\alpha\epsilon)^{3/2}(1+2\alpha\epsilon)^{-1}d\epsilon} - \left(\frac{\int_0^\infty \left(-\frac{\partial f}{\partial \epsilon}\right)\tau_{total}(\epsilon)\,\epsilon^{5/2}(1+\alpha\epsilon)^{3/2}(1+2\alpha\epsilon)^{-1}d\epsilon}{\int_0^\infty \left(-\frac{\partial f}{\partial \epsilon}\right)\tau_{total}(\epsilon)\,\epsilon^{3/2}(1+\alpha\epsilon)^{3/2}(1+2\alpha\epsilon)^{-1}d\epsilon}\right)^2\right]$$

(Eqn. 8.8)

$$S = \frac{k_B}{e}\left(\frac{\int_0^\infty \left(-\frac{\partial f}{\partial \epsilon}\right)\tau_{total}(\epsilon)\,\epsilon^{5/2}(1+\alpha\epsilon)^{3/2}(1+2\alpha\epsilon)^{-1}d\epsilon}{\int_0^\infty \left(-\frac{\partial f}{\partial \epsilon}\right)\tau_{total}(\epsilon)\,\epsilon^{3/2}(1+\alpha\epsilon)^{3/2}(1+2\alpha\epsilon)^{-1}d\epsilon} - \eta\right), \qquad \text{(Eqn. 8.9)}$$

where $\tau_{total}(\epsilon)^{-1} = \sum \tau_i(\epsilon)^{-1}$ ($\tau_i(\epsilon)$ is a relaxation time of a scattering mechanism *i*). Detailed equations for acoustic phonon, polar, and alloy scattering can be found in literatures for $PbS_{0.9978}Cl_{0.0022}$[(188)] and $ZrNiSn_{0.99}Sb_{0.01}$[(190)].

Table 8.1. Estimated maximum error to Eqn. 8.1 for *L* with different band structure and scattering assumptions.

Band[a]	Scattering[b]	Examples	Max. error (%)	Ref.
P	AP	$Sr_3Ga_{0.93}Zn_{0.07}Sb_3$	4.4	183
2P	AP+II	$Si_{0.8}Ge_{0.2}$	7.5	191
K	AP	$PbTe_{0.9988}I_{0.0012}$	19.7	189
		$Pb_{1.002}Se_{0.998}Br_{0.002}$	19.5	187
K	AP+PO	$PbS_{0.9978}Cl_{0.0022}$	19.4	188
K	AP+PO+AL	$ZrNiSn_{0.99}Sb_{0.01}$	25.6	190
2K+P	AP	$PbTe_{0.85}Se_{0.15}$	14.9	30

[a]Band is the type and number of bands involved in evaluating *L*. For instance, "2K+P" means two non-parabolic Kane bands (K) and a parabolic band (P).

[b]Scattering is the type of scattering mechanism assumed in estimating *L*. AP, II, PO, and AL are acoustic phonon, ionized impurities, polar, and alloy scattering, respectively. For example, "AP+PO" means that both acoustic phonon and polar scatterings are assumed in calculating *L*.

8.4 Lorenz number for multiple-band model

Multiple band behavior (present in *p*-type $PbTe_{0.85}Se_{0.15}$, and *n*-type $Si_{0.8}Ge_{0.2}$ Fig. 8.2) can also lead to deviations in the thermopower-dependence of the Lorenz number. In the case of PbTe, hole population of both the light and heavy bands yields a more complicated relationship between *L* and *S*; it is not simply a parametric function of η and depends on the specific effective mass and mobility contributions from each band.

When more than a single band is involved in a transport, total *S* and *L* are expressed as follows:

$$L = \frac{\sum L_i \sigma_i}{\sum \sigma_i} \qquad \text{(Eqn. 8.10)}$$

$$S = \frac{\sum S_i \sigma_i}{\sum \sigma_i} , \qquad \text{(Eqn. 8.11)}$$

where S_i, σ_i, and L_i are Seebeck coefficient, electrical conductivity, and Lorenz number for a band denoted as *i*, respectively. Total *S* and *L* were calculated using Eqns. 8.10 and 8.11 for $Si_{0.8}Ge_{0.2}$[191] (valence band and conduction band, both parabolic bands) and $PbTe_{0.85}Se_{0.15}$[30] (one conduction band and two valence bands where the lower valence band in parabolic while other bands are all Kane type bands).

One last, prevalent source of error occurs because the Wiedemann-Franz law does not take the bipolar thermal conductivity into consideration. κ_l calculated from the difference between κ_{total} and κ_e does include varying portion of bipolar conduction with respect to temperature and band structure of materials (which can become important for lightly doped materials with narrow gaps at high temperatures[196]).

An equation for *L* entirely in terms of the experimentally determined *S* is proposed and found to be accurate (within 20 %) for most common band structures/scattering mechanisms found for thermoelectric materials. Use of this equation would make estimates of lattice thermal conductivity much more accurate without requiring additional measurement.

8.5 Approximate L function with an accuracy within 0.5 %

$$L = 1.49 - 0.49\exp\left[-\frac{|S|}{21}\right] + 1.40\exp\left[-\frac{|S|}{85}\right] \qquad \text{(Eqn. 8.12)}$$

Eqn. 8.12 estimates results of SPB model under APS with a maximum error less than 0.5 % for |S| > ~10 μV/K.

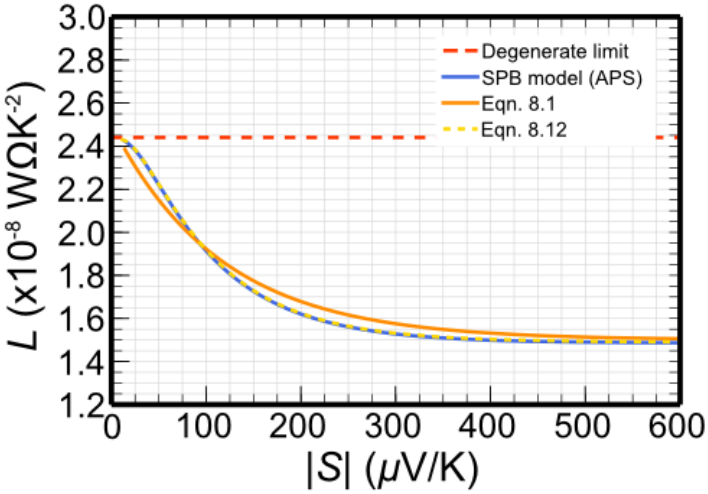

Fig. 8.4. L calculated from Eqn. 8.1 and Eqn. 8.12 in comparison to results of SPB model under APS

Chapter 9

Improved Mechanical Properties of Thermoelectric $(Bi_{0.2}Sb_{0.8})_2Te_3$ by Nanostructuring

This section contains contents that have been accepted to *APL Materials*. Once it is published online, permission will be asked.

9.1 Introduction

Thermoelectric (TE) devices based on Bi_2Te_3 are important for cooling and emerging power generation applications[197]. TE devices are relatively robust and reliable because they are made of solid-state components without any moving parts. However, significant thermal stresses placed on TE materials during material processing, device fabrication, and use can ultimately lead to a mechanical failure if stresses exceed the strength of the materials[198,199]. Although the mechanical strength of a TE material is often overlooked in comparison with its TE figure of merit, $zT = \alpha^2\sigma T/\kappa$ (α, σ, T, and κ are the Seebeck coefficient, electric conductivity, absolute temperature, and the thermal conductivity, respectively), it is also an important parameter to consider especially when the material is to be included within a TE module.

TE materials are commonly prepared by zone-melting[200], Czochralski[201] or Bridgman methods[202]. In Bi_2Te_3-based alloys, these growth methods produce single or oriented polycrystals due to anisotropy in the solidification rate – faster within the *a*-*b* cleavage plane and slower parallel to the *c*-direction. Producing preferentially oriented crystals is advantageous as these materials show a maximum in zT parallel to the growth direction and normal to the *c*-direction[12]. The zT of $(Bi_{0.25}Sb_{0.75})_2Te_3$ single crystal was reported to be ~0.87 at 300 K[(12)]. Among the listed crystal growth methods, the vertical zone-melting is the most widespread method for the industrial production of textured $(Bi, Sb)_2Te_3$ crystals with large-sized grains.

However, in lab-scale experiments, higher zT has been observed in polycrystalline $(Bi, Sb)_2Te_3$ with micron sized grains. Although the grinding of material to decrease grain size disrupts the preferable orientation of grains thereby lowering σ, the zT of p-type $(Bi, Sb)_2Te_3$ at 300 K increases to the value ~1.0 because of increased grain boundary scattering of phonons, which results in a much lower κ[203]. Further enhancement in zT was achieved by reducing the average grain size of the polycrystalline $(Bi, Sb)_2Te_3$ down to nanoscale ($zT \approx 1.1$-1.3)[27,203-205]. Many methods of synthesizing bulk nanocrystalline $(Bi, Sb)_2Te_3$ involve ball-milling powders to nanosize and subsequently compacting the powders by hot pressing or spark plasma sintering (SPS)[27,203-205]. Some of the preferred grain orientation lost during ball-milling can also be recovered through high-temperature extrusion of $(Bi, Sb)_2Te_3$ samples[206-209].

Although there are many reports on thermoelectric properties of $(Bi, Sb)_2Te_3$ samples prepared via different processing routes, the temperature-dependent mechanical properties of the samples are not sufficiently investigated[210-212]. In particular, there are few studies comparing the mechanical properties of nanostructured $(Bi, Sb)_2Te_3$ with those of state-of-the-art zone-melted $(Bi, Sb)_2Te_3$[213-215]. In this work, temperature-dependent fracture strengths of $(Bi, Sb)_2Te_3$ processed by vertical zone-melting, hot extrusion, and SPS are presented. In addition, a mechanism is proposed for the low brittle-ductile transition temperature observed in the nanostructured sample prepared by SPS. These strength data along with an understanding of their underlying mechanisms are essential for developing TE materials optimized for high and reliable performance within TE modules.

9.2 Experimental

Ingots were produced with a stoichiometric composition of $(Bi_{0.2}Sb_{0.8})_2Te_3$ by melting the elemental components in sealed quartz ampoules at a temperature of 720 °C for 2 hours followed by quenching. The ingots were confirmed to be single phase by X-ray diffraction (XRD). These ingots were further processed by three different methods, vertical zone-melting, hot extrusion, and hot compaction, using SPS. Vertical zone-melting was performed using a Kristall-810 with resistive heating. Temperature of the molten zone

was between 700-780 (±1) °C and the temperature gradient at the crystallization front was ~100 °C/cm. The molten zone passed through the ingot twice: downwards with a speed of ~0.5 mm/min followed by upwards at a reduced speed of ~0.1-0.15 mm/min.

Hot extrusion was performed using an IP2500 250-ton hydraulic press equipped with a temperature control system maintained between 400-450 °C. Samples were extruded at a pressure of 250-300 MPa at a punch speed of 0.5 mm/min producing an extrusion factor of 18.

For the SPS processed materials, ingots were first ball-milled to a particle size of ~8-10 nm using a Retsch PM 400 high-speed planetary mill. The techniques for obtaining nano-sized powders and estimating size of the powders are described in more details in refs. 203-205. The nanopowder was compacted into disks 20 mm diameter and 5 mm thickness under a pressure of 250 MPa in protective atmosphere at room temperature. Next, the disks were sintered using a Fuji SPS-511S SPS at a temperature of 450-500 °C for 10 min under pressure of 50 MPa. The speed of heating and cooling was 16 °C/min.

To determine the mechanical properties, rectangular samples of size $5 \times 5 \times 6$ mm^3 were cut using electrical discharge machining (EDM) from the materials fabricated by each of the three methods. The length scale of material affected by EDM is in the order of 10 μm, significantly lower than the dimensions of the samples for mechanical testing. This was estimated from changes of width in XRD peaks before and after EDM. Any change in strength due to EDM is negligible regardless of the processing route. An Instron model 5982 controlled using “Bluehill Materials Testing Software” was used for mechanical tests under uniaxial compression. The uncertainty of loading on the sample is not expected to exceed 0.4 %, and the uncertainty of travel is ± 0.001 mm. Tests were performed with speed of 0.05 mm/min. A demountable hinged electric furnace was used for heating samples during measurement; temperature was measured using a Type-K thermocouple. The cut samples were placed under uniaxial compression in such a way that the compression direction was along the growth direction and the extrusion direction for the zone-melted and extruded

samples, respectively. For SPS processed samples, loading was normal to the compaction direction during SPS.

9.3 Fracture strength of materials prepared via different methods

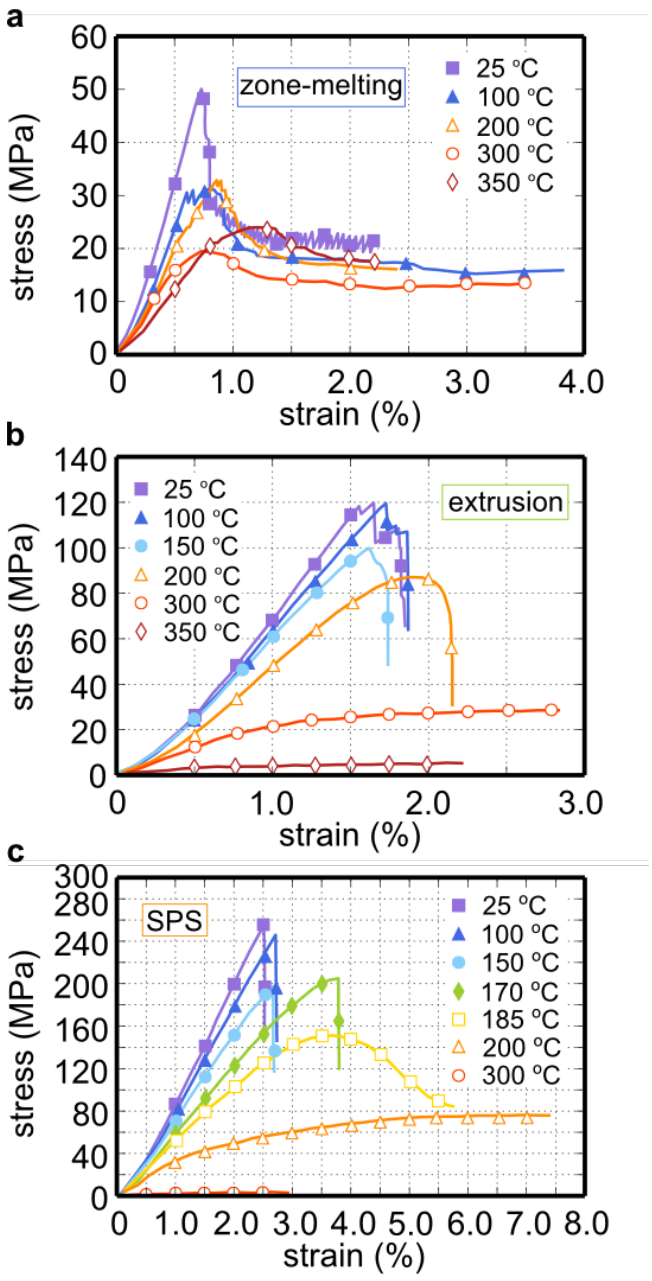

Fig. 9.1. Stress – strain curves for the samples processed by zone-melting (a), hot extrusion (b), and SPS (c) at temperatures: (■) – 25 ºC; (▲) – 100 ºC; (●) – 150 ºC, (♦) – 170 ºC, (□) – 185 ºC, (Δ) – 200 ºC, (○) – 300 ºC, (◊) – 350 ºC

The stress-strain curves recorded during sample deformation are presented in Fig. 9.1. For all of the $(Bi_{0.2}Sb_{0.8})_2Te_3$ samples at low strains, the deformation is elastic and follows Hooke's law. At 25 ^oC, the slope of the plots, a measure of the elastic stiffness of the material, is highest in the SPS processed nanograined material, followed by the extruded and then zone melted materials. The nanograined material is roughly fifty percent more stiff than the zone melted. Compounds of the form $(Bi,Sb)_2(Te,Se)_3$ are highly anisotropic in their mechanical properties. This is due to the strong covalent bonding present within the a-b planes and weak van der Waals bonding between neighboring Te/Se planes. For example, in Bi_2Te_2Se, the elastic stiffness constant is over 7 times smaller parallel to the c-axis as compared to the a or b axes[22]. The stiffness variation between materials produced via different methods can be understood in terms of grain size and preferred orientation. In the nanograined materials, the random orientation of grains results in an averaging effect of the elastic properties within the material. In contrast, the extruded and zone melted materials exhibit more preferential orientation in their grains making them weaker in specific directions and easier to deform.

Brittle fracture is observed in all samples without appreciable plastic deformation at temperatures below 200 ^oC. In the stress – strain curves for the zone-melted sample, pronounced jumps in the deformation curves are observed due to the formation of cracks or deformation twinning (purple curves in Fig. 9.1a for 25 ^oC). Overall, the stress at failure is highest in the nano-grained SPS material and lowest in the zone-melted material. This difference is attributable to grain size and orientation differences. Nano-grained materials are known to fracture through grain boundaries (inter-granular fracture) while coarse-grained materials (> 10 μm) fracture along specific crystallographic planes within grains (transgranular fracture)[216]. In the larger grained zone melted material, failure occurs via transgranular cleavage between the weakly bonded neighboring Te planes. The cleavage planes throughout the sample are far more aligned in zone melted materials than randomly oriented SPS materials. At smaller grain sizes, cleavage planes no longer align over appreciable distances and failure proceeds by inter-granular means. The small grain size limits the length of any initiating cracks which can be present and the material is markedly more resistant to

fracture. Unlike others, the zone-melted sample went through partial plastic deformation before the fracture even at $T < 200$ °C. Because grains in the zone-melted sample have not experienced heavy deformation like those in extruded or SPS sample during the synthesis, there may be more room for the movement of dislocations in the sample under stress[217].

As the temperature is raised, a marked brittle-ductile transition is observed and plastic deformation begins to occur. For samples produced by zone-melting or extrusion, the brittle-ductile transition occurs within a broad temperature range from 200 to 300 °C. When average grain size of the samples prepared by zone-melting and extrusion was reduced to tens of μm (from the order of mm) the materials became much stronger at low temperatures. Nonetheless, even with smaller grain size, they also weakened above 200 °C. In the nanostructured material (SPS sample), the transition occurs at lower temperatures between 170-200 °C.

At high temperatures, there was no ultimate destruction of the sample during the course of testing; instead plastic deformation was accompanied by deformation hardening. This behavior was observed for the extruded sample at 300-350 °C and for nanostructured at 200-300 °C. Therefore, the maximum stress values for these samples cannot be considered as true strengths-to-failure although they effectively characterize the mechanical strength of the materials.

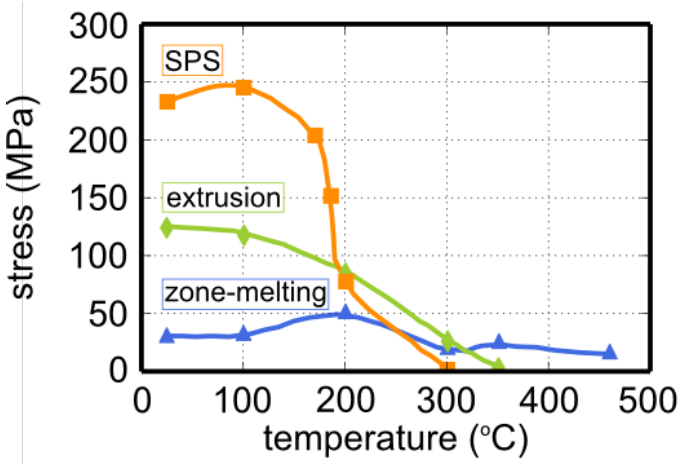

Fig. 9.2. Temperature-dependent strength of the samples fabricated by zone-melting (▲), extrusion (♦), and SPS (■). The maximum pressure during the course of high-temperature testing of the extruded and SPS samples without destruction were obtained from Fig. 2.1.

The temperature dependence of the maximum stress values is shown in Fig. 9.2. A rapid decrease in mechanical strength above 200 °C is found for all of the $(Bi_{0.2}Sb_{0.8})_2Te_3$ samples. Above 100 °C the samples prepared by zone-melting, have strength of only 20-30 MPa which varies only slightly with temperature.

The plastic deformation behavior of the samples prepared by zone-melting and extrusion at elevated temperature can be described by dislocation slip and dislocation pile-up within grains[218-223]. During deformation, the dislocation density is increased by bowing of dislocations between pinning points such as in Frank-Read sources or screw dislocations which have experienced a segment of double cross-slip. Materials which possess high initial dislocation density are able to generate more during deformation.

Dislocation motion is impeded at grain boundaries due to the misalignment of slip planes between neighboring grains. As grain size decreases, the interactions between dislocations and grain boundaries can have a significant strengthening effect. Dependence of the grain size (L) reduction to strengthening is described by the Hall–Petch relationship:

$$\sigma_T = \sigma_0 + K \cdot L^{-1/2}, \qquad \text{(Eqn. 9.1)}$$

where σ_T is yield strength, σ_0 is the yield strength of a single-crystal, and K is the material dependent Hall–Petch factor[224]. Our experimental work qualitatively follows the Hall–Petch equation. The grain size of extruded samples is smaller than that in the zone-melted samples approximately by a factor of 18 (from the extrusion factor). If we assume σ_0 to be negligible, the ratio of the σ_T of the extruded sample to that of the zone-melted sample can be roughly estimated to be $\sim 18^{-1/2} \approx 4.2$. Accordingly, the strength of extruded samples at room temperature (≈ 130 MPa), is 4-5 times higher than that of the zone-melted sample (Fig. 9.2 green and blue lines).

The Hall-Petch relationship is related to stress-induced dislocation motion near grain boundaries. A pile-up of dislocations against a grain boundary exerts a reinforced stress proportional to the number of dislocations within the pile-up[85]. Yielding occurs when the stress concentration of the pile-up exceeds the threshold

required to activate dislocation generation and slip to neighboring grains. Due to the repulsive interactions between dislocations with Burger's vector of the same sign, the dislocation spacing within a pile-up is determined by the applied stress. Smaller grain size can effectively limit the number of dislocations which can be present in a pile-up, thereby limiting the stress compounding effect. A material with smaller grain size is thus expected to require a higher applied stress to yield via this mechanism.

However, for materials with grain size below 100 nm, the Hall-Petch equation overestimates the yield strength[225-227]. For a given applied stress, at a small enough grain size only a single dislocation can be present near a boundary and the compounding effect of a pile-up will no longer exist[228]. Consequently, the Hall-Petch relation breaks down[229]. Dislocations are either absent in nanograins or present in only small quantities. As a result there are no heterogeneous sources for dislocation generation and reproduction, and homogeneous formation of dislocations requires stresses on the order of $\tau \approx 900$ MPa (from $\tau \approx G/30$ where the shear modulus, G, for Bi_2Te_3 is ~ 27 GPa), well beyond the fracture strength of the nanostructured sample in Fig. 9.2 (orange line)[230,231].

Alternatively, grain-boundary sliding has been proposed as the dominant deformation mechanism for the nanostructured SPS sample. This process is characterized by grain-restricted slippage, migration, and dynamic recrystallization[224,232-234]. Simulation has shown that in nano-grained material, deformation occurs by grain-boundary sliding instead of dislocation slip within grains typically observed in large grains[39]. This behavior has been confirmed experimentally in the grain-size dependent flow stress of Cu[40]. Thermally-activated grain boundary shear was found to be the deformation mechanism in nano-scale grains. If a second phase other than $(Bi_{0.2}Sb_{0.8})_2Te_3$ were present on the grain boundaries, this could negatively influence on the strength of the material. However, when the SPS nanostructured sample was analyzed by high-resolution transmission electron microscopy (HRTEM) equipped with energy dispersive spectroscopy (EDS) detector from EDAX, the composition of grain boundaries was found to be homogeneous and the same as within the grains. Furthermore, the grain boundaries were atomically-sharp without any chemical heterogeneity or intermediate phases. Even if the Te-phase separation (Fig. 9.6) did happen at high

annealing temperature, the temperature at which the strength of the nanostructured sample started to drop was even lower than the annealing temperature. Thus, in this case, the deformation of the nanostructured sample may be related to the reduction grain boundary area due to recrystallization at high temperatures.

The nanostructured sample demonstrates much higher fracture strength compared to the other samples (Fig. 9.2), but as temperature increases its strength reduces to that of coarse-grained samples[226]. This drop in strength of the nanostructured sample can be attributed to increased grain-boundary diffusion coefficient at high temperature which in turn raises the plasticity under stress.

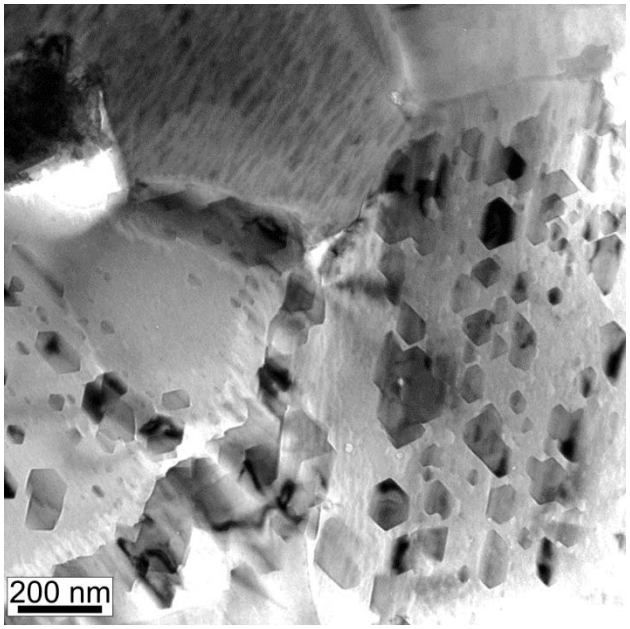

Fig. 9.3. HRTEM image of the sample produced by SPS at a temperature of 500 ºC

There is a correlation between the mechanical and thermoelectric properties of $(Bi,Sb)_2Te_3$ materials and the sintering temperature. The nanostructured samples sintered at 450-500 ºC possess not only the maximum thermoelectric figure of merit[203], but also the highest mechanical strength. At these sintering temperatures, there is a fragmentation of the initial grains due to formation of nanograins with the same structure and pores (Fig. 9.3). These may be created by the precipitation of excess elemental Te due to its low melting point (450 ºC)[235]. Although an ingot of stoichiometric composition of $(Bi_{0.2}Sb_{0.8})_2Te_3$ was used

in the nanostructured sample, not all of the Te was included in the matrix. According to the phase diagram[235] a small amount of Te (less than 0.5 at. %) can exist in elemental form because of anti-site defects (Sb in Te site)[236]. Another possibility can be the melting of nano-sized $(Bi_{0.2}Sb_{0.8})_2Te_3$. The SPS sintering temperature (500 °C) of the ball-milled ingot (in 8-10 nm) was only about 15 % lower than the melting temperature of of bulk Bi_2Te_3 (585 °C)[237]. Given the fact that the melting point of nano-sized Bi-Sn alloy (10 nm) can be reduced by 15 % of its bulk melting temperature[238], the precipitation of the nano-sized $(Bi_{0.2}Sb_{0.8})_2Te_3$ during the SPS is physically possible. However, the mechanism involved in the formation of nano-sized pores observed in Fig. 9.3 is still under investigation.

Thermoelectric properties (σ and α) of the nanostructured sample during thermocycling were measured up to temperatures of 250 °C (Fig. 9.4) and 300 °C (Fig. 9.5). The temperature-dependent σ and α stayed almost the same during five cycles of heating (up to 250 °C) and cooling (Fig. 9.4). However, upon increasing the maximum temperature to 300 °C, changes in the σ and α were observed even from the first cycle of heating and cooling (σ decreased and α increased as shown in Fig. 9.5). It could be concluded that the nanostructured sample was only thermostable at temperatures below 250 °C (its strength was significantly reduced starting at 150-200 °C as in Fig. 9.2).

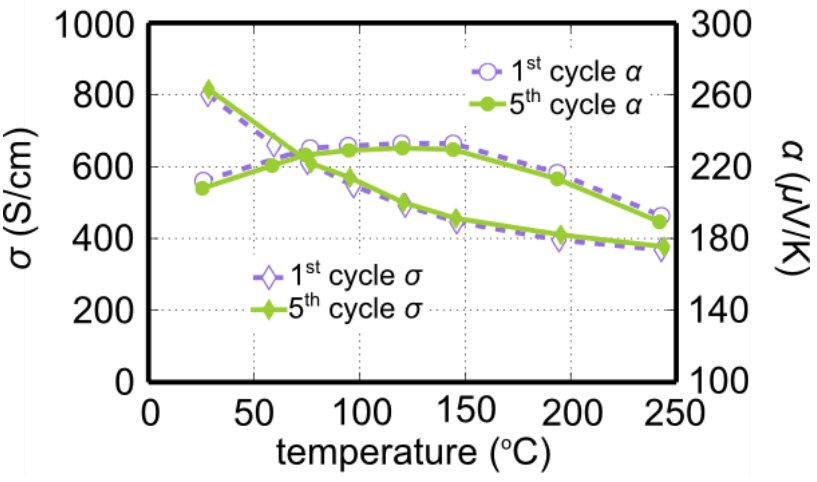

Fig. 9.4. Temperature dependences of electrical conductivity (σ) and Seebeck coefficient (α) of the nanostructured (SPS) sample at cycling (♦, ● - the first cycle; ◊, ○ - the fifth cycle).

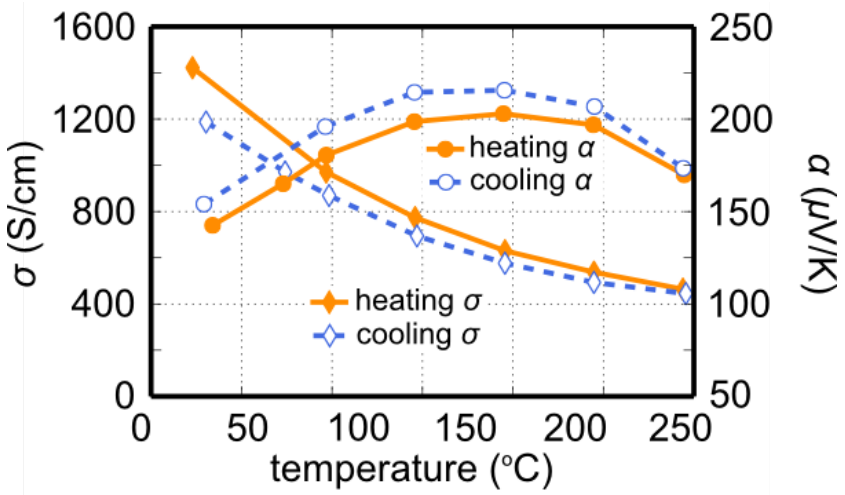

Fig. 9.5. Temperature dependences of electrical conductivity (σ) and Seebeck coefficient (α) of the nanostructured (SPS) sample at cycling (♦, ● - heating; ◊, ○ - cooling).

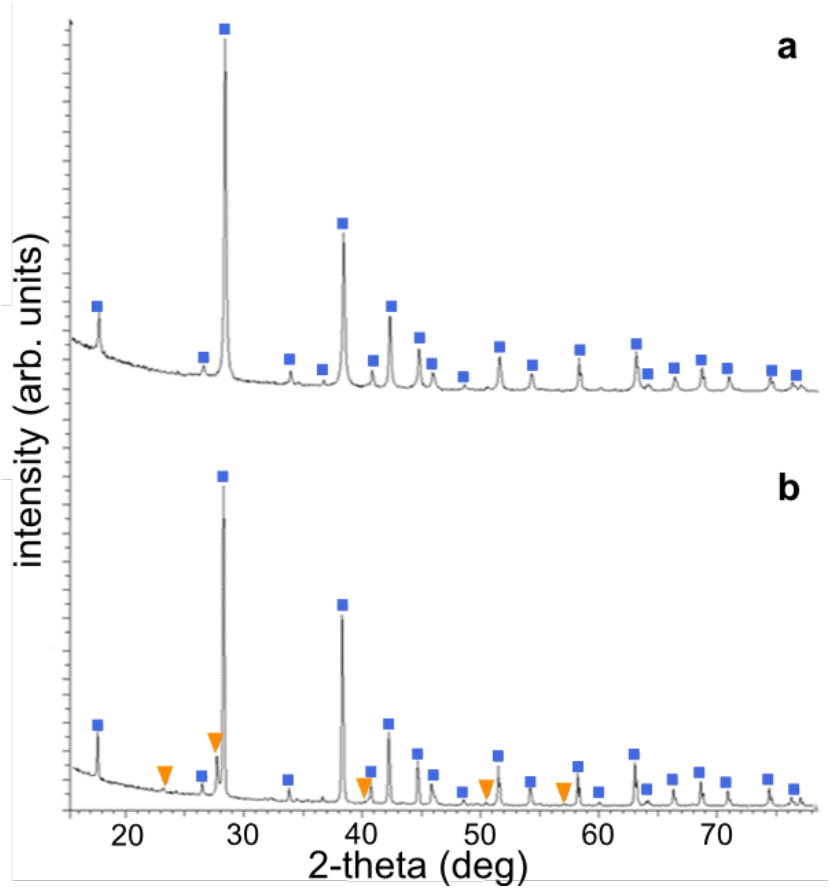

Fig. 9.6. X-ray diffraction of nanostructured samples before annealing (a) and after annealing at temperature 300 °C for 2 hours (b) (■ - $(Bi_{0.2}Sb_{0.8})_2Te_3$, ▼ - Te).

In the Bi-Sb-Te system, the composition $(Bi,Sb)_2Te_3$ is homogenous at room temperature, but a tellurium rich phase may phase separate at elevated temperatures depending on the nominal Te content[235]. As shown in the X-ray diffraction results of Fig. 9.6, annealing the samples in air at 300 ºC for 2 hours led to the separation of the elemental tellurium phase. This separation along with grain growth due to recrystallization could contribute to the thermal instability of both the thermoelectric and mechanical properties. During thermocycling to 300 ºC (Fig. 9.5), the excess tellurium phase separates into the grain boundaries (Fig. 9.6). However, the thermal activation energy provided by annealing combined with the diffusing Te may have decreased the concentration of anti-site defects[239] within the bulk (hence the reduced electrical conductivity of the cooling sample in Fig. 9.6). Even a small amount of Te present in grain boundaries of the nanostructured sample can further weaken the material since it can facilitate rotation of grains at high temperatures. The concurrent loss of thermoelectric and mechanical performance above 250 ºC defines a temperature range of practical use of nanostructured $(Bi,Sb)_2Te_3$ materials within thermoelectric generators.

The temperature-dependent fracture strength under uniaxial compression of $(Bi_{0.2}Sb_{0.8})_2Te_3$ samples produced by either vertical zone-melting, hot extrusion, or SPS were investigated. It was observed that the strength of the nanostructured sample (via SPS) was higher than that of the zone-melted or extruded sample at a room temperature. However, at $T > 300$ °C, the strength of the nanostructured sample decreased and became comparable to that of the zone-melted sample. Grain boundary slippage in the nanostructured sample was proposed as a mechanism for this sudden drop in strength at temperatures higher than 170-200°C. Based on the observed Te-phase separation in the nanostructured sample annealed at 300 °C, a maximum operating temperature for a thermoelectric generator made with the nanostructured sample was suggested (< 250 °C).

BIBLIOGRAPHY

1 Kim, S. I. *et al.* Dense dislocation arrays embedded in grain boundaries for high-performance bulk thermoelectrics. *Science* **348**, 109-114, doi:10.1126/science.aaa4166 (2015).

2 Neuburger, A. *The Technical Arts and Sciences of the Ancients.* (Kegan Paul, 2003).

3 Rees, J. *Refrigeration Nation: A History of Ice, Appliances, and Enterprise in America.* (Johns Hopkins University Press, 2013).

4 Health, N. Y. D. o. & Health, N. Y. B. o. *Annual Report.* (New York State Department of Health., 1908).

5 Freidberg, S. *Fresh - A Perishable History.* (Harvard University Press, 2009).

6 Constable, G. & Somerville, B. *A Century of Innovation: Twenty Engineering Achievements that Transformed Our Lives.* (Joseph Henry Press, 2003).

7 Velders, G. J. *et al.* Preserving Montreal Protocol climate benefits by limiting HFCs. *Science* **335**, 922-923 (2012).

8 May, A. F. & Snyder, G. J. in *Materials, Preparation, and Characterization in Thermoelectrics* 1-18 (CRC Press, 2012).

9 Wang, H. *High Temperature Transport Properties of Lead Chalcogenides and Their Alloys* Doctor of Philosophy thesis, California Institute of Technology, (2014).

10 Snyder, G. J. & Toberer, E. S. Complex thermoelectric materials. *Nat. Mater.* **7**, 105-114 (2008).

11 Goldsmid, H. J. *Thermoelectric refrigeration.* (Plenum Press, 1964).

12 Scherrer, S. & Scherrer, H. in *CRC Handbook of Thermoelectrics* (CRC Press, 1995).

13 Drabble, J. R. Galvanomagnetic Effects in p-Type Bismuth Telluride. *Proceedings of the Physical Society* **72**, 380 (1958).

14 Chen, X., Parker, D. & Singh, D. J. Importance of non-parabolic band effects in the thermoelectric properties of semiconductors. *Scientific Reports* **3**, 3168, doi:10.1038/srep03168 (2013).

15 Ikeda, T., Marolf, N. J. & Snyder, G. J. Zone Leveling Crystal Growth of Thermoelectric PbTe Alloys with Sb2Te3 Widmanstätten Precipitates. *Crystal Growth & Design* **11**, 4183-4189, doi:10.1021/cg2007588 (2011).

16 Iwanaga, S., Toberer, E. S., LaLonde, A. & Snyder, G. J. A high temperature apparatus for measurement of the Seebeck coefficient. *Rev. Sci. Instrum.* **82**, 063905, doi:doi:http://dx.doi.org/10.1063/1.3601358 (2011).

17 Ravich, Y. I., Efimova, B. A. & Smirnov, I. A. *Semiconducting Lead Chalcogenides.* Vol. 5 181, 299 (Plenum Press, 1970).

18 Wang, H., LaLonde, A. D., Pei, Y. & Snyder, G. J. The Criteria for Beneficial Disorder in Thermoelectric Solid Solutions. *Adv. Funct. Mater.* **23**, 1586-1596, doi:10.1002/adfm.201201576 (2013).

19 Putley, E. H. Galvano- and thermo-magnetic coefficients for a multi-band conductor. *Journal of Physics C: Solid State Physics* **8**, 1837 (1975).

20 Sehr, R. & Testardi, L. R. The optical properties of p-type Bi_2Te_3 - Sb_2Te_3 alloys between 2-15 microns. *J. Phys. Chem. Solids* **23**, 1219-1224, doi:http://dx.doi.org/10.1016/0022-3697(62)90169-5 (1962).

21 Gibbs, Z. M., LaLonde, A. & Snyder, G. J. Optical band gap and the Burstein–Moss effect in iodine doped PbTe using diffuse reflectance infrared Fourier transform spectroscopy. *New Journal of Physics* **15**, 075020 (2013).

22 Stordeur, M., Stölzer, M., Sobotta, H. & Riede, V. Investigation of the Valence Band Structure of Thermoelectric (Bi1−xSbx)2Te3 Single Crystals. *Phys. Status Solidi B* **150**, 165-176, doi:10.1002/pssb.2221500120 (1988).

23 Walia, S. *et al.* Sb2Te3 and Bi2Te3 based thermopower wave sources. *Energ. Environ. Sci.* **4**, 3558-3564, doi:10.1039/C1EE01370J (2011).

24 Yang, F., Ikeda, T., Snyder, G. J. & Dames, C. Effective thermal conductivity of polycrystalline materials with randomly oriented superlattice grains. *J. Appl. Phys.* **108**, -, doi:doi:http://dx.doi.org/10.1063/1.3457334 (2010).

25 Yim, W. M. & Rosi, F. D. Compound tellurides and their alloys for peltier cooling—A review. *Solid·State Electron.* **15**, 1121-1140, doi:http://dx.doi.org/10.1016/0038-1101(72)90172-4 (1972).

26 Xie, W. *et al.* Identifying the Specific Nanostructures Responsible for the High Thermoelectric Performance of (Bi,Sb)2Te3 Nanocomposites. *Nano Lett.* **10**, 3283-3289, doi:10.1021/nl100804a (2010).

27 Poudel, B. *et al.* High-Thermoelectric Performance of Nanostructured Bismuth Antimony Telluride Bulk Alloys. *Science* **320**, 634-638, doi:10.1126/science.1156446 (2008).

28 Mehta, R. J. *et al.* A new class of doped nanobulk high-figure-of-merit thermoelectrics by scalable bottom-up assembly. *Nat Mater* **11**, 233-240, doi:http://www.nature.com/nmat/journal/v11/n3/abs/nmat3213.html#supplementary-information (2012).

29 Wang, H., Pei, Y., LaLonde, A. D. & Jeffery Snyder, G. in *Thermoelectric Nanomaterials: Materials Design and Applications* (eds Kunihito Koumoto & Takao Mori) 3-32 (Springer Berlin Heidelberg, 2013).

30 Pei, Y. *et al.* Convergence of electronic bands for high performance bulk thermoelectrics. *Nature* **473**, 66-69, doi:http://www.nature.com/nature/journal/v473/n7345/abs/10.1038-nature09996-unlocked.html#supplementary-information (2011).

31 Caillat, T., Gailliard, L., Scherrer, H. & Scherrer, S. Transport properties analysis of single crystals (BixSb1 − x)2Te3 grown by the traveling heater method. *J. Phys. Chem. Solids* **54**, 575-581, doi:http://dx.doi.org/10.1016/0022-3697(93)90235-J (1993).

32 Süssmann, H. & Heiliger, W. Seebeck coefficient and electrical conductivity in p-(Bi1−xSbx)2 Te3 at room temperature. *Phys. Status Solidi A* **80**, 535-539, doi:10.1002/pssa.2210800215 (1983).

33 Stordeur, M. in *CRC Handbook of Thermoelectrics* (ed D. M. Rowe) (CRC Press, 1995).

34 Erofeev, R. S. & Ovechkina, V. N. Energy Spectrum of Solid Solutions of Bi2Te3-Sb2Te3 System. *Izv. Akad. Nauk SSSR, Neorg. Mater.* **17**, 1780-1784 (1981).

35 Gaidukova, V. S., Erofeev, R. S. & Ovechkina, V. N. Characteristics of the energy spectrum of solid solutions in the SbTe-BiTe system. *Izv. Akad. Nauk SSSR, Neorg. Mater.* **17**, 244 - 247 (1981).

36 Mishra, S. K., Satpathy, S. & Jepsen, O. Electronic structure and thermoelectric properties of bismuth telluride and bismuth selenide. *J. Phys.: Condens. Matter* **9**, 461 (1997).

37 Heinz, N. A., Ikeda, T., Pei, Y. & Snyder, G. J. Applying Quantitative Microstructure Control in Advanced Functional Composites. *Adv. Funct. Mater.* **24**, 2135-2153, doi:10.1002/adfm.201302899 (2014).

38 Heinz, N. A. *Microstructure control and iodine doping of bismuth telluride* Ph. D. thesis, California Institute of Technology, (2014).

39 Shi, H., Parker, D., Du, M.-H. & Singh, D. J. Connecting Thermoelectric Performance and Topological-Insulator Behavior: Bi2Te3 and Bi2Te2Se from First Principles. *Physical Review Applied* **3**, 014004 (2015).

40 Youn, S. J. & Freeman, A. J. First-principles electronic structure and its relation to thermoelectric properties of Bi2Te3. *Phys. Rev. B* **63**, 085112 (2001).

41 Larson, P. Effect of p1/2 corrections in the electronic structure of Bi2Te3 compounds. *Phys. Rev. B* **68**, 155121 (2003).

42 Wang, G. & Cagin, T. Electronic structure of the thermoelectric materials Bi2Te3 and Sb2Te3 from first-principles calculations. *Phys. Rev. B* **76**, 075201 (2007).

43 Biswas, S. & Bhattacharya, R. Two Valence Subbands in Single Crystals of Bismuth Telluride Doped with Lead and Its Electrical Properties. *Phys. Status Solidi B* **151**, 193-201, doi:10.1002/pssb.2221510123 (1989).

44 Von Middendorff, A. & Landwehr, G. Evidence for a second valence band in p-type Bi_2Te_3 from magneto-seebeck and Shubnikov-de Haas data. *Solid State Commun.* **11**, 203-207 (1972).

45 Kohler, H. Non-parabolicity of the highest valence band of Bi_2Te_3 from Shubnikov-de Haas effect. *Phys. Status Solidi B* **74**, 591 (1976).

46 Rönnlund, B., Beckman, O. & Levy, H. Doping properties of Sb2Te3 indicating a two valence band model. *J. Phys. Chem. Solids* **26**, 1281-1286, doi:http://dx.doi.org/10.1016/0022-3697(65)90109-5 (1965).

47 von Middendorff, A., Dietrich, K. & Landwehr, G. Shubnikov-De Haas Effect in p-type Sb_2Te_3. *Solid State Commun.* **Vol. 13**, 443 - 446 (1973).

48 Kohler, H. & Freudenberger, A. Investigation of the highest valence band in $(Bi_{1-x}Sb_x)_2Te_3$ crystals. *Phys. Status Solidi B* **84**, 195 (1977).

49 Eichler, W. & Simon, G. Galvanomagnetic transport properties of Sb2Te3. *Phys. Status Solidi B* **86**, K85-K88, doi:10.1002/pssb.2220860170 (1978).

50 Simon, G. & Eichler, W. Investigation on a Two-Valence Band Model for Sb_2Te_3. *Phys. Status Solidi B* **107**, 201 (1981).

51 Gibbs, Z. M. *et al.* Temperature dependent band gap in PbX (X = S, Se, Te). *Appl. Phys. Lett.* **103**, 262109, doi:doi:http://dx.doi.org/10.1063/1.4858195 (2013).

52 Kane, E. O. Band structure of indium antimonide. *J. Phys. Chem. Solids* **1**, 249-261, doi:http://dx.doi.org/10.1016/0022-3697(57)90013-6 (1957).

53 Sologub, V. V., Goletskaya, A. D., Lang, I. G. & Pavlov, S. T. Valence-Band Properties of Bi2Te3 from Galvanomagnetic Measurements. *Phys. Status Solidi B* **58**, 457-470, doi:10.1002/pssb.2220580205 (1973).

54 Kulbachinskii, V. A. *et al.* Thermoelectric Power and Scattering of Carriers in Bi2—xSnxTe3 with Layered Structure. *Phys. Status Solidi B* **199**, 505-513, doi:10.1002/1521-3951(199702)199:2<505::AID-PSSB505>3.0.CO;2-9 (1997).

55 Drašar, Č. *et al.* Figure of merit of quaternary (Sb0.75Bi0.25)2−xInxTe3 single crystals. *J. Appl. Phys.* **104**, 023701, doi:doi:http://dx.doi.org/10.1063/1.2956608 (2008).

56 Kulbachinskii, V. A., Kytin, A. V. G. & Tarasov, P. M. in *Thermoelectrics, 2006. ICT '06. 25th International Conference on.* 459-464.

57 Kulbachinskii, V. *et al.* Valence-band energy spectrum of solid solutions of narrow-gap-semiconductor Bi2-xSnxTe3 single crystals. *Phys. Rev. B* **50**, 16921-16930, doi:10.1103/PhysRevB.50.16921 (1994).

58 Kulbachinskii, V. A. *et al.* Influence of Sn on Galvanomagnetic Properties of Layered p-(Bi1—xSbx)2Te3 Semiconductors. *Phys. Status Solidi B* **229**, 1467-1480, doi:10.1002/1521-3951(200202)229:3<1467::AID-PSSB1467>3.0.CO;2-T (2002).

59 Goldsmid, H. J. Recent Studies of Bismuth Telluride and Its Alloys. *J. Appl. Phys.* **32**, 2198-2202, doi:doi:http://dx.doi.org/10.1063/1.1777042 (1961).

60 Dresselhaus, M. S. *et al.* New Directions for Low-Dimensional Thermoelectric Materials. *Adv. Mater.* **19**, 1043-1053, doi:10.1002/adma.200600527 (2007).

61 Medlin, D. L. & Snyder, G. J. Interfaces in bulk thermoelectric materials: A review for Current Opinion in Colloid and Interface Science. *Current Opinion in Colloid & Interface Science* **14**, 226-235, doi:http://dx.doi.org/10.1016/j.cocis.2009.05.001 (2009).

62 Fan, S. *et al.* p-type Bi0.4Sb1.6Te3 nanocomposites with enhanced figure of merit. *Appl. Phys. Lett.* **96**, 182104, doi:doi:http://dx.doi.org/10.1063/1.3427427 (2010).

63 Toberer, E. S., Zevalkink, A. & Snyder, G. J. Phonon engineering through crystal chemistry. *J. Mater. Chem.* **21**, 15843-15852, doi:10.1039/C1JM11754H (2011).

64 Klemens, P. G. The Scattering of Low-Frequency Lattice Waves by Static Imperfections. *Proc. Phys. Soc. London, Sect. A* **68**, 1113 (1955).

65 Kim, P., Shi, L., Majumdar, A. & McEuen, P. L. Thermal Transport Measurements of Individual Multiwalled Nanotubes. *Phys. Rev. Lett.* **87**, 215502 (2001).

66 Nader, M., Aldinger, F. & Hoffmann, M. J. Influence of the α/β-SiC phase transformation on microstructural development and mechanical properties of liquid phase sintered silicon carbide. *J Mater Sci* **34**, 1197-1204, doi:10.1023/a:1004552704872.

67 Jorgensen, P. J. & Bartlett, R. W. Liquid-phase sintering of SmCo5. *J. Appl. Phys.* **44**, 2876-2880, doi:doi:http://dx.doi.org/10.1063/1.1662663 (1973).

68 Nazaré, S., Ondracek, G. & Thümmler, F. in *Modern Developments in Powder Metallurgy: Volume 5: Materials and Properties Proceedings of the 1970 International Powder Metallurgy Conference, sponsored by the Metal Power Industries Federation and the American Powder Metallurgy Institute* (ed Henry H. Hausner) 171-186 (Springer US, 1971).

69 Zhao, D. & Tan, G. A review of thermoelectric cooling: Materials, modeling and applications. *Appl. Therm. Eng.* **66**, 15-24, doi:http://dx.doi.org/10.1016/j.applthermaleng.2014.01.074 (2014).

70 Williams, D. B. & Carter, C. B. in *Transmission Electron Microscopy: A Textbook for Materials Science* 463-481 (Springer US, 2009).

71 Humphreys, F. J. & Hatherly, M. in *Recrystallization and Related Annealing Phenomena (Second Edition)* 91-119 (Elsevier, 2004).

72 Peranio, N. & Eibl, O. Gliding dislocations in Bi2Te3 materials. *Phys. Status Solidi A* **206**, 42-49, doi:10.1002/pssa.200824224 (2009).

73 German, R. M., Suri, P. & Park, S. J. Review: liquid phase sintering. *J Mater Sci* **44**, 1-39, doi:10.1007/s10853-008-3008-0 (2008).

74 Herzig, C. & Mishin, Y. in *Diffusion in Condensed Matter: Methods, Materials, Models* (eds Paul Heitjans & Jörg Kärger) 337-366 (Springer Berlin Heidelberg, 2005).

75 Cahn, J. W., Mishin, Y. & Suzuki, A. Coupling grain boundary motion to shear deformation. *Acta Mater.* **54**, 4953-4975, doi:http://dx.doi.org/10.1016/j.actamat.2006.08.004 (2006).

76 Medlin, D. L., Erickson, K. J., Limmer, S. J., Yelton, W. G. & Siegal, M. P. Dissociated $$ \frac{1}{3}\langle 0\bar{1}1\rangle $$ $\frac{1}{3}\langle 0\bar{1}1\rangle$ dislocations in Bi2Te3 and their relationship to seven-layer Bi3Te4 defects. *J Mater Sci* **49**, 3970-3979, doi:10.1007/s10853-014-8035-4 (2014).

77 Hu, L.-P. *et al.* Shifting up the optimum figure of merit of p-type bismuth telluride-based thermoelectric materials for power generation by suppressing intrinsic conduction. *NPG Asia Mater* **6**, e88, doi:10.1038/am.2013.86 (2014).

78 Callaway, J. & von Baeyer, H. C. Effect of Point Imperfections on Lattice Thermal Conductivity. *Phys. Rev.* **120**, 1149-1154 (1960).

79 Slack, G. A. & Galginaitis, S. Thermal Conductivity and Phonon Scattering by Magnetic Impurities in CdTe. *Phys. Rev.* **133**, A253-A268 (1964).

80 Roufosse, M. & Klemens, P. G. Thermal Conductivity of Complex Dielectric Crystals. *Phys. Rev. B* **7**, 5379-5386 (1973).

81 He, J., Girard, S. N., Kanatzidis, M. G. & Dravid, V. P. Microstructure-Lattice Thermal Conductivity Correlation in Nanostructured PbTe0.7S0.3 Thermoelectric Materials. *Adv. Funct. Mater.* **20**, 764-772, doi:10.1002/adfm.200901905 (2010).

82 Abeles, B. Lattice Thermal Conductivity of Disordered Semiconductor Alloys at High Temperatures. *Phys. Rev.* **131**, 1906-1911 (1963).

83 Morelli, D. T., Heremans, J. P. & Slack, G. A. Estimation of the isotope effect on the lattice thermal conductivity of group IV and group III-V semiconductors. *Phys. Rev. B* **66**, 195304 (2002).

84 Cockayne, D. J. H., Ray, I. L. F. & Whelan, M. J. Investigations of dislocation strain fields using weak beams. *Philos. Mag.* **20**, 1265-1270, doi:10.1080/14786436908228210 (1969).

85 Mott, N. F. CXVII. A theory of work-hardening of metal crystals. *The London, Edinburgh, and Dublin Philosophical Magazine and Journal of Science* **43**, 1151-1178, doi:10.1080/14786441108521024 (1952).

86 Clarke, D. R. & Phillpot, S. R. Thermal barrier coating materials. *Mater. Today* **8**, 22-29, doi:http://dx.doi.org/10.1016/S1369-7021(05)70934-2 (2005).

87 Min, G. & Rowe, D. M. Cooling performance of integrated thermoelectric microcooler. *Solid·State Electron.* **43**, 923-929, doi:http://dx.doi.org/10.1016/S0038-1101(99)00045-3 (1999).

88 Gao, M. in *Thermoelectrics Handbook* 11-11-11-15 (CRC Press, 2005).

89 Pinwen, Z. *et al.* Enhanced thermoelectric properties of PbTe alloyed with Sb 2 Te 3. *J. Phys.: Condens. Matter* **17**, 7319 (2005).

90 Abeles, B., Beers, D. S., Cody, G. D. & Dismukes, J. P. Thermal Conductivity of Ge-Si Alloys at High Temperatures. *Phys. Rev.* **125**, 44-46 (1962).

91 Feldman, J. L., Singh, D. J., Mazin, I. I., Mandrus, D. & Sales, B. C. Lattice dynamics and reduced thermal conductivity of filled skutterudites. *Phys. Rev. B* **61**, R9209-R9212 (2000).

92 Sales, B. C., Mandrus, D. & Williams, R. K. Filled Skutterudite Antimonides: A New Class of Thermoelectric Materials. *Science* **272**, 1325-1328, doi:10.1126/science.272.5266.1325 (1996).

93 May, A. F., Fleurial, J.-P. & Snyder, G. J. Thermoelectric performance of lanthanum telluride produced via mechanical alloying. *Phys. Rev. B* **78**, 125205 (2008).

94 Brown, S. R., Kauzlarich, S. M., Gascoin, F. & Snyder, G. J. Yb14MnSb11: New High Efficiency Thermoelectric Material for Power Generation. *Chem. Mater.* **18**, 1873-1877, doi:10.1021/cm060261t (2006).

95 Wang, Y., Gu, C. & Ruan, X. Optimization of the random multilayer structure to break the random-alloy limit of thermal conductivity. *Appl. Phys. Lett.* **106**, 073104, doi:doi:http://dx.doi.org/10.1063/1.4913319 (2015).

96 Biswas, K. *et al.* Strained endotaxial nanostructures with high thermoelectric figure of merit. *Nat Chem* **3**, 160-166, doi:http://www.nature.com/nchem/journal/v3/n2/abs/nchem.955.html#supplementary-information (2011).

97 Callaway, J. Model for Lattice Thermal Conductivity at Low Temperatures. *Phys. Rev.* **113**, 1046-1051 (1959).

98 Steigmeier, E. F. & Abeles, B. Scattering of Phonons by Electrons in Germanium-Silicon Alloys. *Phys. Rev.* **136**, A1149-A1155 (1964).

99 Stordeur, M. & Sobotta, H. *The Proceedings of the First European Conference on Thermoelectrics*. 209 - 212 (Pereqrinus Ltd., 1988).

100 Bessas, D. *et al.* Lattice dynamics in Bi_{2}Te_{3} and Sb_{2}Te_{3}: Te and Sb density of phonon states. *Phys. Rev. B* **86**, 224301 (2012).

101 Yang, F., Ikeda, T., Snyder, G. J. & Dames, C. Effective thermal conductivity of polycrystalline materials with randomly oriented superlattice grains. *J. Appl. Phys.* **108**, 034310, doi:10.1063/1.3457334 (2010).

102 Chen, X. *et al.* Thermal expansion coefficients of Bi2Se3 and Sb2Te3 crystals from 10 K to 270 K. *Appl. Phys. Lett.* **99**, 261912, doi:doi:http://dx.doi.org/10.1063/1.3672198 (2011).

103 Landolt, H. H. & Börnstein, R. *Numerical Data and Functional Relationships in Science and Technology*. Vol. 17f (Springer, 1983).

104 Ziman, J. M. *Electrons and Phonons: The Theory of Transport Phenomena in Solids*. (OUP Oxford, 1960).

105 Klemens, P. G. in *Solid State Physics - Advances in Research and Applications* Vol. 7 (eds F. Seitz & D. Turnbull) 1-98 (Academic Press Inc., 1958).

106 Klemens, P. G. in *Thermal Conductivity* Vol. 1 (ed R. P. Tye) 1-68 (Academic Press, 1969).

107 Friedman, A. J. Lattice Thermal Conductivity of a Deformed Copper-Germanium Alloy. *Phys. Rev. B* **7**, 663-666 (1973).

108 Ackerman, M. W. & Klemens, P. G. Phonon Scattering by Impurity Atmospheres Surrounding Dislocations. III. Combined Mass and Distortion Scattering. *J. Appl. Phys.* **42**, 968-971, doi:doi:http://dx.doi.org/10.1063/1.1660194 (1971).

109 Mitchell, M. A., Klemens, P. G. & Reynolds, C. A. Lattice Thermal Conductivity of Plastically Deformed Copper plus 10 Atomic Percent Aluminum Specimens in the Temperature Range 1-4\ifmmode^\circ\else\textdegree\fi{}K. *Phys. Rev. B* **3**, 1119-1130 (1971).

110 Madarasz, F. L. & Klemens, P. G. Phonon scattering by dislocations in metallic alloys. *Phys. Rev. B* **23**, 2553-2562 (1981).

111 Wang, Y., Qiu, B., McGaughey, A. J. H., Ruan, X. & Xu, X. Mode-wise thermal conductivity of Bismuth Telluride. *J. of Heat Transfer* **135**, 091102 (2013).

112 Mott, N. F. CXVII. A theory of work-hardening of metal crystals. *Philosophical Magazine Series 7* **43**, 1151-1178, doi:10.1080/14786441108521024 (1952).

113 Medlin, D. L., Erickson, K. J., Limmer, S. J., Yelton, W. G. & Siegal, M. P. Dissociated \frac{1}{3}\langle 0\bar{1}11\rangle dislocations in Bi2Te3 and their relationship to seven-layer Bi3Te4 defects. *J Mater Sci* **49**, 3970-3979, doi:10.1007/s10853-014-8035-4 (2014).

114 Berman, R. The Thermal Conductivity of some Polycrystalline Solids at Low Temperatures. *Proceedings of the Physical Society. Section A* **65**, 1029 (1952).

115 Morelli, D. T., Uher, C. & Robinson, C. J. Transmission of phonons through grain boundaries in diamond films. *Appl. Phys. Lett.* **62**, 1085-1087, doi:doi:http://dx.doi.org/10.1063/1.108802 (1993).

116 Borup, K. A. *et al.* Measuring thermoelectric transport properties of materials. *Energ. Environ. Sci.* **8**, 423-435, doi:10.1039/C4EE01320D (2015).

117 Wang, Z., Alaniz, J. E., Jang, W., Garay, J. E. & Dames, C. Thermal Conductivity of Nanocrystalline Silicon: Importance of Grain Size and Frequency-Dependent Mean Free Paths. *Nano Lett.* **11**, 2206-2213, doi:10.1021/nl1045395 (2011).

118 Biswas, K. *et al.* High-performance bulk thermoelectrics with all-scale hierarchical architectures. *Nature* **489**, 414-418, doi:http://www.nature.com/nature/journal/v489/n7416/abs/nature11439.html#supplementary-information (2012).

119 de Haas, W. J. & Biermasz, T. The dependence on thickness of the thermal resistance of crystals at low temperatures. *Physica* **5**, 619-624, doi:http://dx.doi.org/10.1016/S0031-8914(38)80009-4 (1938).

120 Casimir, H. B. G. Note on the conduction of heat in crystals. *Physica* **5**, 495-500, doi:http://dx.doi.org/10.1016/S0031-8914(38)80162-2 (1938).

121 Berman, R. *Thermal conduction in solids*. (Clarendon Press, 1976).

122 Hua, C. & Minnich, A. J. Importance of frequency-dependent grain boundary scattering in nanocrystalline silicon and silicon–germanium thermoelectrics. *Semicond. Sci. Technol.* **29**, 124004 (2014).

123 Schelling, P. K., Phillpot, S. R. & Keblinski, P. Kapitza conductance and phonon scattering at grain boundaries by simulation. *J. Appl. Phys.* **95**, 6082-6091, doi:doi:http://dx.doi.org/10.1063/1.1702100 (2004).

124 Cahill, D. G. *et al.* Nanoscale thermal transport. II. 2003–2012. *Applied Physics Reviews* **1**, 011305, doi:doi:http://dx.doi.org/10.1063/1.4832615 (2014).

125 Young, D. A. & Maris, H. J. Lattice-dynamical calculation of the Kapitza resistance between fcc lattices. *Phys. Rev. B* **40**, 3685-3693 (1989).

126 Fuchs, K. The conductivity of thin metallic films according to the electron theory of metals. *Mathematical Proceedings of the Cambridge Philosophical Society* **34**, 100-108, doi:doi:10.1017/S0305004100019952 (1938).

127 Sondheimer, E. H. The mean free path of electrons in metals. *Adv. Phys.* **50**, 499-537, doi:10.1080/00018730110102187 (2001).

128 Chen, G. Size and Interface Effects on Thermal Conductivity of Superlattices and Periodic Thin-Film Structures. *J. Heat Transfer* **119**, 220-229, doi:10.1115/1.2824212 (1997).

129 Savvides, N. & Goldsmid, H. J. Boundary scattering of phonons in fine-grained hot-pressed Ge-Si alloys. I. The dependence of lattice thermal conductivity on grain size and porosity. *Journal of Physics C: Solid State Physics* **13**, 4657 (1980).

130 Savvides, N. & Goldsmid, H. J. Boundary scattering of phonons in fine-grained hot-pressed Ge-Si alloys. II. Theory. *Journal of Physics C: Solid State Physics* **13**, 4671 (1980).

131 Klemens, P. G. Phonon Scattering by Cottrell Atmospheres Surrounding Dislocations. *J. Appl. Phys.* **39**, 5304-5305, doi:10.1063/1.1655956 (1968).

132 Kemp, W. R. G., Klemens, P. G., Sreedhar, A. K. & White, G. K. The Thermal and Electrical Conductivity of Silver-Palladium and Silver-Cadmium Alloys at Low Temperatures. *Proceedings of the Royal Society of London A: Mathematical, Physical and Engineering Sciences* **233**, 480-493, doi:10.1098/rspa.1956.0005 (1956).

133 Lomer, J. N. & Rosenberg, H. M. The detection of dislocations by low temperature heat conductivity measurements. *Philos. Mag.* **4**, 467-483, doi:10.1080/14786435908233416 (1959).

134 Zou, J., Kotchetkov, D., Balandin, A. A., Florescu, D. I. & Pollak, F. H. Thermal conductivity of GaN films: Effects of impurities and dislocations. *J. Appl. Phys.* **92**, 2534-2539, doi:doi:http://dx.doi.org/10.1063/1.1497704 (2002).

135 Burgers, J. M. Geometrical considerations concerning the structural irregularities to be assumed in a crystal. *Proceedings of the Physical Society* **52**, 23 (1940).

136 Bragg, W. L. Discussion. Part I. *Proceedings of the Physical Society* **52**, 54 (1940).

137 Read, W. T. & Shockley, W. Dislocation Models of Crystal Grain Boundaries. *Phys. Rev.* **78**, 275-289 (1950).

138 Schindler, R., Clemans, J. E. & Balluffi, R. W. On grain boundary dislocations in plane matching grain boundaries. *Phys. Status Solidi A* **56**, 749-761, doi:10.1002/pssa.2210560243 (1979).

139 Sutton, A. P., Balluffi, R. W. & Vitek, V. On intrinsic secondary grain boundary dislocation arrays in high angle symmetrical tilt grain boundaries. *Scripta Metallurgica* **15**, 989-994, doi:http://dx.doi.org/10.1016/0036-9748(81)90240-4 (1981).

140 Schober, T. & Balluffi, R. W. Quantitative observation of misfit dislocation arrays in low and high angle twist grain boundaries. *Philos. Mag.* **21**, 109-123, doi:10.1080/14786437008238400 (1970).

141 Man, C.-S., Gao, X., Godefroy, S. & Kenik, E. A. Estimating geometric dislocation densities in polycrystalline materials from orientation imaging microscopy. *Int. J. Plast.* **26**, 423-440, doi:http://dx.doi.org/10.1016/j.ijplas.2009.08.002 (2010).

142 Chen, X. *et al.* Thermal expansion coefficients of Bi2Se3 and Sb2Te3 crystals from 10 K to 270 K. *Appl. Phys. Lett.* **99**, -, doi:doi:http://dx.doi.org/10.1063/1.3672198 (2011).

143 Madelung, O. *Landbolt-Bornstein Numerical Data and Functional Relationships in Science and Technology*. Vol. 17e 163, 432 (Springer-Verlag, 1983).

144 Pei, Y., LaLonde, A., Iwanaga, S. & Snyder, G. J. High thermoelectric figure of merit in heavy hole dominated PbTe. *Energ. Environ. Sci.* **4**, 2085-2089, doi:10.1039/C0EE00456A (2011).

145 Singman, C. N. Atomic volume and allotropy of the elements. *J. Chem. Educ.* **61**, 137, doi:10.1021/ed061p137 (1984).

146 Rowe, D. M., Shukla, V. S. & Savvides, N. Phonon scattering at grain boundaries in heavily doped fine-grained silicon-germanium alloys. *Nature* **290**, 765-766 (1981).

147 Schmidt, R., Case, E., Giles, J., III, Ni, J. & Hogan, T. Room-Temperature Mechanical Properties and Slow Crack Growth Behavior of Mg2Si Thermoelectric Materials. *J. Electron. Mater.* **41**, 1210-1216, doi:10.1007/s11664-011-1879-3 (2012).

148 Goldsmid, H. J. & Sharp, J. W. Estimation of the thermal band gap of a semiconductor from Seebeck measurements. *J Electron Mater* **28**, 869-872, doi:DOI 10.1007/s11664-999-0211-y (1999).

149 Chasmar, R. P. & Stratton, R. The Thermoelectric Figure of Merit and its Relation to Thermoelectric Generators. *Journal of Electronics and Control* **7**, 52-72 (1959).

150 Mahan, G. D. in *Solid State Physics* Vol. 51 *Solid State Physics-Advances in Research and Applications* 81-157 (Academic Press Inc, 1998).

151 Glen, A. S. in *CRC Handbook of Thermoelectrics* (CRC Press, 1995).

152 Pei, Y., LaLonde, A. D., Wang, H. & Snyder, G. J. Low effective mass leading to high thermoelectric performance. *Energ Environ Sci* **5**, 7963-7969 (2012).

153 Pei, Y., Wang, H. & Snyder, G. J. Band Engineering of Thermoelectric Materials. *Adv Mater* **24**, 6125-6135, doi:10.1002/adma.201202919 (2012).

154 Austin, I. G. The Optical Properties of Bismuth Telluride. *Proceedings of the Physical Society* **72**, 545 (1958).

155 Wang, S. *et al.* Enhanced thermoelectric properties of $Bi_2(Te_{1-x}Se_x)_3$-based compounds as n-type legs for low-temperature power generation. *J. Mater. Chem.* **22**, 20943-20951, doi:10.1039/C2JM34608G (2012).

156 Snyder, G. J., Wang, H., Pei, Y. Z. & LaLonde, A. D. Heavily Doped p-Type PbSe with High Thermoelectric Performance: An Alternative for PbTe. *Adv Mater* **23**, 1366-1370, doi:10.1002/adma.201004200 (2011).

157 Wang, H., Pei, Y., LaLonde, A. D. & Snyder, G. J. Weak electron–phonon coupling contributing to high thermoelectric performance in n-type PbSe. *Proceedings of the National Academy of Sciences* **109**, 9705-9709, doi:10.1073/pnas.1111419109 (2012).

158 LaLonde, A. D., Pei, Y. Z. & Snyder, G. J. Reevaluation of PbTe(1-x)I(x) as high performance n-type thermoelectric material. *Energ Environ Sci* **4**, 2090-2096, doi:Doi 10.1039/C1ee01314a (2011).

159 Schmitt, J., Gibbs, Z. M., Snyder, G. J. & Felser, C. Resolving the True Band Gap of ZrNiSn Half-Heusler Thermoelectric Materials. *Materials Horizons* (2014).

160 Nolas, G. S., Sharp, J. & Goldsmid, H. J. *Thermoelectrics: Basic Principles and New Materials Developments*. (Springer-Verlag, 2001).

161 Madelung, O. *Semiconductors: Data Handbook*. (Springer-Verlag, 2004).

162 Stordeur, M. & Kuhnberger, W. Nichtparabolizitat des Valenzbandes von Bi_2Te_3 gegolgert adu Transporteigenschaften. *Phys. Status Solidi B* **69**, 377 (1975).

163 Testardi, L. R., Bierly Jr, J. N. & Donahoe, F. J. Transport properties of p-type Bi_2Te_3-Sb_2Te_3 alloys in the temperature range 80–370°K. *J. Phys. Chem. Solids* **23**, 1209-1217, doi:http://dx.doi.org/10.1016/0022-3697(62)90168-3 (1962).

164 Jeon, H.-W., Ha, H.-P., Hyun, D.-B. & Shim, J.-D. Electrical and thermoelectrical properties of undoped Bi2Te3-Sb2Te3 and Bi2Te3-Sb2Te3-Sb2Se3 single crystals. *J. Phys. Chem. Solids* **52**, 579-585, doi:http://dx.doi.org/10.1016/0022-3697(91)90151-O (1991).

165 Plecháček, T., Navrátil, J., Horák, J. & Lošťák, P. Defect structure of Pb-doped Bi2Te3 single crystals. *Philos. Mag.* **84**, 2217-2228, doi:10.1080/14786430410001678226 (2004).

166 Mandrus, D. *et al.* Electronic transport in lightly doped CoSb3. *Phys Rev B* **52**, 4926-4931 (1995).

167 Heinrich, H. *et al.* Efficient dopants for ZrNiSn-based thermoelectric materials. *Journal of Physics: Condensed Matter* **11**, 1697 (1999).

168 Shen, Q. *et al.* Effects of partial substitution of Ni by Pd on the thermoelectric properties of ZrNiSn-based half-Heusler compounds. *Appl Phys Lett* **79**, 4165-4167, doi:doi:http://dx.doi.org/10.1063/1.1425459 (2001).

169 LaLonde, A. D., Pei, Y., Wang, H. & Jeffrey Snyder, G. Lead telluride alloy thermoelectrics. *Mater Today* **14**, 526-532, doi:10.1016/s1369-7021(11)70278-4 (2011).

170 Liu, W. *et al.* Studies on the Bi2Te3-Bi2Se3-Bi2S3 system for mid-temperature thermoelectric energy conversion. *Energ. Environ. Sci.* **6**, 552-560, doi:10.1039/C2EE23549H (2013).

171 Zhao, L. D. *et al.* All-scale hierarchical thermoelectrics: MgTe in PbTe facilitates valence band convergence and suppresses bipolar thermal transport for high performance. *Energ. Environ. Sci.* **6**, 3346-3355, doi:10.1039/C3EE42187B (2013).

172 Minnich, A. J., Dresselhaus, M. S., Ren, Z. F. & Chen, G. Bulk nanostructured thermoelectric materials: current research and future prospects. *Energ Environ Sci* **2**, 466-479, doi:10.1039/B822664B (2009).

173 Yu, F. *et al.* Enhanced thermoelectric figure of merit in nanocrystalline Bi2Te3 bulk. *J Appl Phys* **105**, 094303, doi:doi:http://dx.doi.org/10.1063/1.3120865 (2009).

174 Bahk, J.-H. & Shakouri, A. Enhancing the thermoelectric figure of merit through the reduction of bipolar thermal conductivity with heterostructure barriers. *Appl Phys Lett* **105**, 052106, doi:doi:http://dx.doi.org/10.1063/1.4892653 (2014).

175 May, A. F., Fleurial, J. P. & Snyder, G. J. Thermoelectric performance of lanthanum telluride produced via mechanical alloying. *Phys. Rev. B* **78**, doi:10.1103/PhysRevB.78.125205 (2008).

176 Pei, Y., Wang, H. & Snyder, G. J. Thermoelectric Materials: Band Engineering of Thermoelectric Materials (Adv. Mater. 46/2012). *Adv. Mater.* **24**, 6124-6124, doi:10.1002/adma.201290290 (2012).

177 Toberer, E. S., Baranowski, L. L. & Dames, C. Advances in Thermal Conductivity. *Annu. Rev. Mater. Res.* **42**, 179-209, doi:doi:10.1146/annurev-matsci-070511-155040 (2012).

178 Lukas, K. *et al.* Experimental determination of the Lorenz number in $Cu_{0.01}Bi_2Te_{2.7}Se_{0.3}$ and $Bi_{0.88}Sb_{0.12}$. *Phys. Rev. B* **85**, 205410 (2012).

179 Flage-Larsen, E. & Prytz, Ø. The Lorenz function: Its properties at optimum thermoelectric figure-of-merit. *Appl. Phys. Lett.* **99**, 202108, doi:doi:http://dx.doi.org/10.1063/1.3656017 (2011).

180 May, A. F. & Snyder, G. J. in *Thermoelectrics and its Energy Harvesting* Vol. 1 (ed D. M. Rowe) Ch. 11, (CRC Press, 2012).

181 Pei, Y., Lensch-Falk, J., Toberer, E. S., Medlin, D. L. & Snyder, G. J. High Thermoelectric Performance in PbTe Due to Large Nanoscale Ag2Te Precipitates and La Doping. *Adv. Funct. Mater.* **21**, 241-249, doi:10.1002/adfm.201000878 (2011).

182 Pei, Y., Heinz, N. A., LaLonde, A. & Snyder, G. J. Combination of large nanostructures and complex band structure for high performance thermoelectric lead telluride. *Energ. Environ. Sci.* **4**, 3640-3645, doi:10.1039/C1EE01928G (2011).

183 Zevalkink, A. *et al.* Thermoelectric properties of Sr3GaSb3 - a chain-forming Zintl compound. *Energ. Environ. Sci.* **5**, 9121-9128, doi:10.1039/C2EE22378C (2012).

184 May, A. F., Fleurial, J.-P. & Snyder, G. J. Optimizing Thermoelectric Efficiency in La3−xTe4 via Yb Substitution. *Chem. Mater.* **22**, 2995-2999, doi:10.1021/cm1004054 (2010).

185 Zevalkink, A., Toberer, E. S., Zeier, W. G., Flage-Larsen, E. & Snyder, G. J. Ca3AlSb3: an inexpensive, non-toxic thermoelectric material for waste heat recovery. *Energ. Environ. Sci.* **4**, 510-518, doi:10.1039/C0EE00517G (2011).

186 Fu, C. *et al.* Electron and phonon transport in Co-doped FeV0.6Nb0.4Sb half-Heusler thermoelectric materials. *J. Appl. Phys.* **114**, -, doi:doi:http://dx.doi.org/10.1063/1.4823859 (2013).

187 Wang, H., Pei, Y., LaLonde, A. D. & Snyder, G. J. Weak electron–phonon coupling contributing to high thermoelectric performance in n-type PbSe. *Proc. Natl. Acad. Sci. U.S.A.* **109**, 9705-9709, doi:10.1073/pnas.1111419109 (2012).

188 Wang, H., Schechtel, E., Pei, Y. & Snyder, G. J. High Thermoelectric Efficiency of n-type PbS. *Adv. Energy. Mater.* **3**, 488-495, doi:10.1002/aenm.201200683 (2013).

189 LaLonde, A. D., Pei, Y. & Snyder, G. J. Reevaluation of PbTe1-xIx as high performance n-type thermoelectric material. *Energ. Environ. Sci.* **4**, 2090-2096, doi:10.1039/C1EE01314A (2011).

190 Xie, H. *et al.* The intrinsic disorder related alloy scattering in ZrNiSn half-Heusler thermoelectric materials. *Sci. Rep.* **4**, doi:10.1038/srep06888 http://www.nature.com/srep/2014/141103/srep06888/abs/srep06888.html#supplementary-information (2014).

191 Vining, C. B. A model for the high-temperature transport properties of heavily doped n-type silicon-germanium alloys. *J. Appl. Phys.* **69**, 331-341, doi:doi:http://dx.doi.org/10.1063/1.347717 (1991).

192 Wood, C. Materials for thermoelectric energy conversion. *Rep. Prog. Phys.* **51**, 459 (1988).

193 Bhandari, C. M. & Rowe, D. M. Electronic contribution to the thermal conductivity of narrow band gap semiconductors-effect of non-parabolicity of bands. *J. Phys. D: Appl. Phys.* **18**, 873 (1985).

194 Ravich, Y. I., Efimova, B. A. & Smirnov, I. A. in *Semiconducting Lead Chalcogenides* (ed L. S. Stil'bans) 149-219 (Springer US, 1970).

195 Zhu, P. *et al.* Carrier-Concentration-Dependent Transport and Thermoelectric Properties of PbTe Doped with Sb_2Te_3. *Mater. Trans.* **46**, 2690-2693, doi:10.2320/matertrans.46.2690 (2005).

196 Gibbs, Z. M., Kim, H.-S., Wang, H. & Snyder, G. J. Band gap estimation from temperature-depedent Seebeck measurement - deviations from $2e|S|_{max}T_{max}$. *Appl. Phys. Lett.* **106**, 022112 (2015).

197 Bell, L. E. Cooling, Heating, Generating Power, and Recovering Waste Heat with Thermoelectric Systems. *Science* **321**, 1457-1461, doi:10.1126/science.1158899 (2008).

198 Suhir, E. Stresses in Bi-Metal Thermostats. *Journal of Applied Mechanics* **53**, 657-660, doi:10.1115/1.3171827 (1986).

199 Suhir, E. & Shakouri, A. Assembly Bonded at the Ends: Could Thinner and Longer Legs Result in a Lower Thermal Stress in a Thermoelectric Module Design? *Journal of Applied Mechanics* **79**, 061010-061010, doi:10.1115/1.4006597 (2012).

200 Pfann, W. G. Principles of zone melting. *Trans. AiME* **194**, 747-753 (1952).

201 Czochralski, J. Ein neues Verfahren zur Messung der Kristallisationsgeschwindigheit der Metalle. *Z. phys. Chemie.* **92**, 219-221 (1918).

202 Bridgman, P. W. Certain Physical Properties of Single Crystals of Tungsten, Antimony, Bismuth, Tellurium, Cadmium, Zinc, and Tin. *Proceedings of the American Academy of Arts and Sciences* **60**, 305-383, doi:10.2307/25130058 (1925).

203 Bulat, L. P. *et al.* Structure and Transport Properties of Bulk Nanothermoelectrics Based on Bi x Sb2−x Te3 Fabricated by SPS Method. *J. Electron. Mater.* **42**, 2110-2113, doi:10.1007/s11664-013-2536-9 (2013).

204 Bulat, L. *et al.* Bulk Nanostructured Polycrystalline p-Bi-Sb-Te Thermoelectrics Obtained by Mechanical Activation Method with Hot Pressing. *J. Electron. Mater.* **39**, 1650-1653 (2010).

205 Bulat, L. P. *et al.* The Influence of Anisotropy and Nanoparticle Size Distribution on the Lattice Thermal Conductivity and the Thermoelectric Figure of Merit of Nanostructured (Bi,Sb)2Te3. *J. Electron. Mater.* **43**, 2121-2126, doi:10.1007/s11664-014-2988-6 (2014).

206 Yang, J. *et al.* Microstructure control and thermoelectric properties improvement to n-type bismuth telluride based materials by hot extrusion. *J. Alloys Compd.* **429**, 156-162, doi:http://dx.doi.org/10.1016/j.jallcom.2006.04.030 (2007).

207 Keshavarz, M. K., Vasilevskiy, D., Masut, R. A. & Turenne, S. p-Type Bismuth Telluride-Based Composite Thermoelectric Materials Produced by Mechanical Alloying and Hot Extrusion. *J. Electron. Mater.* **42**, 1429-1435, doi:10.1007/s11664-012-2284-2 (2013).

208 Lognoné, Q. *et al.* Quantitative Texture Analysis of Spark Plasma Textured n-Bi2Te3. *J. Am. Ceram. Soc.* **97**, 2038-2045, doi:10.1111/jace.12970 (2014).

209 Xu, Z. J., Hu, L. P., Ying, P. J., Zhao, X. B. & Zhu, T. J. Enhanced thermoelectric and mechanical properties of zone melted p-type (Bi,Sb)2Te3 thermoelectric materials by hot deformation. *Acta Mater.* **84**, 385-392, doi:http://dx.doi.org/10.1016/j.actamat.2014.10.062 (2015).

210 Zheng, Y. *et al.* Mechanically Robust BiSbTe Alloys with Superior Thermoelectric Performance: A Case Study of Stable Hierarchical Nanostructured Thermoelectric Materials. *Adv. Energy. Mater.* **5**, n/a-n/a, doi:10.1002/aenm.201401391 (2015).

211 Ravi, V. *et al.* Thermal Expansion Studies of Selected High-Temperature Thermoelectric Materials. *J. Electron. Mater.* **38**, 1433-1442, doi:10.1007/s11664-009-0734-2 (2009).

212 Sootsman, J. R. *et al.* Microstructure and Thermoelectric Properties of Mechanically Robust PbTe-Si Eutectic Composites. *Chem. Mater.* **22**, 869-875, doi:10.1021/cm9016672 (2010).

213 Zheng, Y. *et al.* High-Temperature Mechanical and Thermoelectric Properties of p-Type Bi0.5Sb1.5Te3 Commercial Zone Melting Ingots. *J. Electron. Mater.* **43**, 2017-2022, doi:10.1007/s11664-013-2938-8 (2013).

214 Xiao, Y. *et al.* Enhanced thermoelectric and mechanical performance of polycrystalline p-type Bi0.5Sb1.5Te3 by a traditional physical metallurgical strategy. *Intermetallics* **50**, 20-27, doi:http://dx.doi.org/10.1016/j.intermet.2014.02.010 (2014).

215 Wereszczak, A. A., Kirkland, T. P., Jadaan, O. M. & Wang, H. in *Advances in Electronic Ceramics II* 131-140 (John Wiley & Sons, Inc., 2010).

216 Farkas, D., Van Swygenhoven, H. & Derlet, P. M. Intergranular fracture in nanocrystalline metals. *Phys. Rev. B* **66**, 060101 (2002).

217 Kim, J.-K. *et al.* On the Tensile Behavior of High-Manganese Twinning-Induced Plasticity Steel. *Metall and Mat Trans A* **40**, 3147-3158, doi:10.1007/s11661-009-9992-0 (2009).

218 van Bueren, H. G. Theory of creep of germanium crystals. *Physica* **25**, 775-791, doi:http://dx.doi.org/10.1016/0031-8914(59)90003-5 (1959).

219 Alexander, H. & Haasen, P. in *Solid State Phys.* Vol. Volume 22 (eds David Turnbull Frederick Seitz & Ehrenreich Henry) 27-158 (Academic Press, 1969).

220 Taylor, G. I. The Mechanism of Plastic Deformation of Crystals. Part I. Theoretical. *Proceedings of the Royal Society of London A: Mathematical, Physical and Engineering Sciences* **145**, 362-387, doi:10.1098/rspa.1934.0106 (1934).

221 Gilman, J. J. Dislocation Sources in Crystals. *J. Appl. Phys.* **30**, 1584-1594, doi:doi:http://dx.doi.org/10.1063/1.1735005 (1959).

222 Milvidskii, M. G. & Osvenskii, V. B. *Structure defects in semoconductor single crystals.* (Mettallurgia, 1984).

223 de Kock, A. J. R., Roksnoer, P. J. & Boonen, P. G. T. The introduction of dislocations during the growth of floating-zone silicon crystals as a result of point defect condensation. *J. Cryst. Growth* **30**, 279-294, doi:http://dx.doi.org/10.1016/0022-0248(75)90001-9 (1975).

224 Malygin, G. A. Plasticity and strength of micro- and nanocrystalline materials. *Phys. Solid State* **49**, 1013-1033, doi:10.1134/S1063783407060017 (2007).

225 Pande, C. S., Masumura, R. A. & Armstrong, R. W. Viewpoint Set of Selected Papers from a Special Symposium on Nanocrystalline MaterialsPile-up based hall-petch relation for nanoscale materials. *Nanostruct. Mater.* **2**, 323-331, doi:http://dx.doi.org/10.1016/0965-9773(93)90159-9 (1993).

226 Nieman, G. W., Weertman, J. R. & Siegel, R. W. Microhardness of nanocrystalline palladium and copper produced by inert-gas condensation. *Scripta Metallurgica* **23**, 2013-2018, doi:http://dx.doi.org/10.1016/0036-9748(89)90223-8 (1989).

227 Suryanarayanan Iyer, R., Frey, C. A., Sastry, S. M. L., Waller, B. E. & Buhro, W. E. Plastic deformation of nanocrystalline Cu and Cu–0.2 wt.% B. *Materials Science and Engineering: A* **264**, 210-214, doi:http://dx.doi.org/10.1016/S0921-5093(98)01027-2 (1999).

228 Meyers, M. A., Mishra, A. & Benson, D. J. Mechanical properties of nanocrystalline materials. *Prog. Mater Sci.* **51**, 427-556, doi:http://dx.doi.org/10.1016/j.pmatsci.2005.08.003 (2006).

229 Nieh, T. G. & Wadsworth, J. Hall-petch relation in nanocrystalline solids. *Scripta Metallurgica et Materialia* **25**, 955-958, doi:http://dx.doi.org/10.1016/0956-716X(91)90256-Z (1991).

230 Cottrell, A. H. *Dislocations and plastic flow in crystals.* (Clarendon Press, 1965).

231 Hirth, J. P. & Lothe, J. *Theory of Dislocations.* (Krieger Publishing Company, 1982).

232 Glezer, A. & Pozdnyakov, V. Structural mechanism of plastic deformation of nanomaterials with amorphous intergranular layers. *Nanostruct. Mater.* **6**, 767-769, doi:http://dx.doi.org/10.1016/0965-9773(95)00171-9 (1995).

233 Rostislav, A. A. & Aleksandr, M. G. Strength of nanostructures. *Physics-Uspekhi* **52**, 315 (2009).

234 Hahn, H., Mondal, P. & Padmanabhan, K. A. Plastic deformation of nanocrystalline materials. *Nanostruct. Mater.* **9**, 603-606, doi:http://dx.doi.org/10.1016/S0965-9773(97)00135-9 (1997).

235 Abrikosov, N. K. & Poretskaya, L. V. Study of the ternary system Sb-Bi-Te. *Inorg. Mater. (USSR)* **1**, 462-469 (1965).

236 Starý, Z., Horák, J., Stordeur, M. & Stölzer, M. Antisite defects in Sb2−xBixTe3 mixed crystals. *J. Phys. Chem. Solids* **49**, 29-34, doi:http://dx.doi.org/10.1016/0022-3697(88)90130-8 (1988).

237 Drabble, J. R. *Progress in Semiconductors.* Vol. 7 (John Wiley & Sons, Inc., 1963).

238 Chen, C. L., Lee, J.-G., Arakawa, K. & Mori, H. Comparative study on size dependence of melting temperatures of pure metal and alloy nanoparticles. *Appl. Phys. Lett.* **99**, 013108, doi:doi:http://dx.doi.org/10.1063/1.3607957 (2011).

239 Kim, I.-H. Electronic transport properties of the flash-evaporated p-type Bi0.5Sb1.5Te3 thermoelectric thin films. *Mater. Lett.* **44**, 75-79, doi:http://dx.doi.org/10.1016/S0167-577X(00)00005-7 (2000).